Max-Planck-Institut für Intelligente Systeme
(**ehemals Max-Planck-Institut für Metallforschung)**
Stuttgart

Gas Nitriding of Iron-Based Alloys

Benjamin Schwarz

Dissertation
an der
Universität Stuttgart

Bericht Nr. 248
Juli 2014

GAS NITRIDING OF IRON-BASED ALLOYS

Von der Fakultät Chemie der Universität Stuttgart genehmigte Abhandlung zur Erlangung der Würde eines Doktors der Naturwissenschaften (Dr. rer. nat.)

Vorgelegt von

BENJAMIN SCHWARZ

aus Waiblingen

Hauptberichter:	Prof. Dr. Ir. E. J. Mittemeijer
Mitberichter:	Prof. Dr. J. Bill
Prüfungsvorsitzender:	Prof. Dr. T. Schleid
Tag der Einreichung:	23. Mai 2014
Tag der mündlichen Prüfung:	30. Juli 2014

MAX-PLANCK-INSTITUT FÜR INTELLIGENTE SYSTEME

(EHEMALS MAX-PLANCK-INSTITUT FÜR METALLFORSCHUNG)

INSTITUT FÜR MATERIALWISSENSCHAFT DER UNIVERSITÄT STUTTGART

2014

Indes sie forschten, röntgten, filmten, funkten, entstand von selbst die köstlichste Erfindung:

der Umweg als die kürzeste Verbindung zwischen zwei Punkten.

Erich Kästner

Contents

Chapter 1

Introduction

1.1. General introduction

The high-tech sector depends on advanced materials with tailored properties in order to push the technological progress and the innovation further. Despite the huge competition from other relatively new materials such as aluminum-/magnesium-based alloys, plastics or fiber composites, steel is often the material of choice. This is due to the very high strength and very high hardness of steel in combination with its considerable ductility. These outstanding properties cannot only compensate the advantage of lesser weight of other materials, but even outcompete them. Therefore steel was, is and remains a material in high-technology products.

The mechanical properties of steel are controlled by its chemical composition and its microstructure. Many components need not only good overall bulk mechanical properties, but the surface region of components may require even better properties (as the resistances against wear, fatigue and corrosion) as loading is most severe at the surface. Examples of such components are spur gears or engine valves where a very high surface hardness is needed (since in this region the highest mechanical applied stress occurs); at the same time, in the bulk, a high toughness is required in order to avoid cracks and therefore failure.

Such complex and demanding requirements can be met by subjecting the steel component to thermochemical surface treatments, as nitriding or carburizing and variant thereof. Upon these processes either atomic nitrogen and/or atomic carbon is introduced into the component´s surface. Since granting of the first patent for the nitriding process at the beginning of the 20th century, to *A. Machlet,* a variety of nitriding processes have been developed – always with the aim to

introduce nitrogen in a sufficient quantity in the component´s surface region. In order to introduce enough nitrogen in the component´s surface, nitriding is performed at elevated temperatures. The nitrogen-surface concentration must be high (to establish a gradient of the nitrogen activity). These requirements are fulfilled by the following (industrial) procedures:

- *Gas nitriding*. A gas mixture consisting of NH_3 and H_2 is used.
- *Plasma nitriding*. Use of ionized gases such as mixtures of N_2 and H_2
- *Salt-bath nitriding*. Molten salt consisting of cyanides and cyanates.

Despite the relatively early discovery of the nitriding process, the field of applications grows steadily even today. This is because upon nitriding, in contrast to carburizing, there is no phase transformation of iron. Nitriding can be carried out at temperatures between 500 °C to 580 °C (below the Ac_1 temperature of steel), and thus the transformation of austenite → martensite or austenite → ferrite is absent. This has the great advantage that after nitriding there is only a minimal shape distortion of the treated component and thus a costly post-processing is (usually) not necessary. Employed nitriding steels are of low to medium carbon content and alloyed with elements (such as Al, Ti, V, Cr) having a strong affinity for nitrogen to allow the formation of alloying-element nitrides upon nitriding. Depending on the process parameters a compound layer, consisting of the iron nitrides ε-Fe_3N_{1+x} and/or γ'-Fe_4N_{1-y}, can develop on the component´s surface. This compound layer, due to its very high hardness, improves the resistance against wear and at the same time, by its chemical stability, the resistance against corrosion [1, 2]. The underlying diffusion zone improves the resistance against fatigue due to the precipitated alloying-element nitride particles [3].

In view of the widespread application of the nitriding process in industry, it strikes that there is pronounced lack of fundamental knowledge about the atomic processes taking place in the

component upon nitriding, especially considering the crystal structure, the morphology and the precipitation process of the alloying-element nitrides and the interactions of the different alloying elements.

In order to investigate the nitriding process scientifically, in particular gas nitriding is suitable. Only with this method the thermodynamic conditions (especially the chemical potential of nitrogen) of the nitriding process can be controlled precisely over a wide range. The investigation of the nitriding of iron-based alloys is not only suitable to arrive at a better understanding of the nitriding process itself, but also contributes essentially to fundamental scientific knowledge on phase transformations, thermodynamics and kinetics.

1.2. The gas nitriding facility

The precise control of the nitriding conditions, i.e. temperature and activity of nitrogen, is only possible in a dedicated gas nitriding facility. In this research project a tube-furnace facility (Figure 1) was employed for the nitriding experiments. In order to maintain a constant nitrogen activity (cf. Section 1.3.1) during the complete nitriding treatment a flowing (total gas-flow rate was 500 ml/min corresponding to a linear gas velocity of 13.5 mm/s) gas mixture of pure NH_3 (purity 99.998 vol.%) and pure H_2 (purity 99.999 vol.%) was employed. Gas fluxes were controlled with mass-flow controllers (flow variation ±2.5 ml/min). The facility consists of a vertical multi-zone furnace (three independently controlled heating zones) and a quartz tube with an inner diameter of 28 mm. Above sits a ball valve which disconnects the quartz tube from the transfer tube. The specimen for nitriding is suspended with a quartz fiber at the specimen rod and inserted in the furnace over the transfer tube which acts as a sluice to hinder air to contaminate the atmosphere in the furnace. The nitriding process is started by lowering the specimen rod (including the specimen) through the upper ball valve until the specimen rests in the temperature-

homogenous zone (temperature variation ±1 K). In order to interrupt the nitriding process the lower ball valve was opened and a device was pushed which breaks the quarts fiber and the specimen fell down into a flask filled with nitrogen gas saturated distilled water (N_2 gas removes dissolved O_2 in water) at room temperature. Then the lower ball valve was closed and the specimen was taken out of the flask and rinsed with ethanol and dried with compressed air.

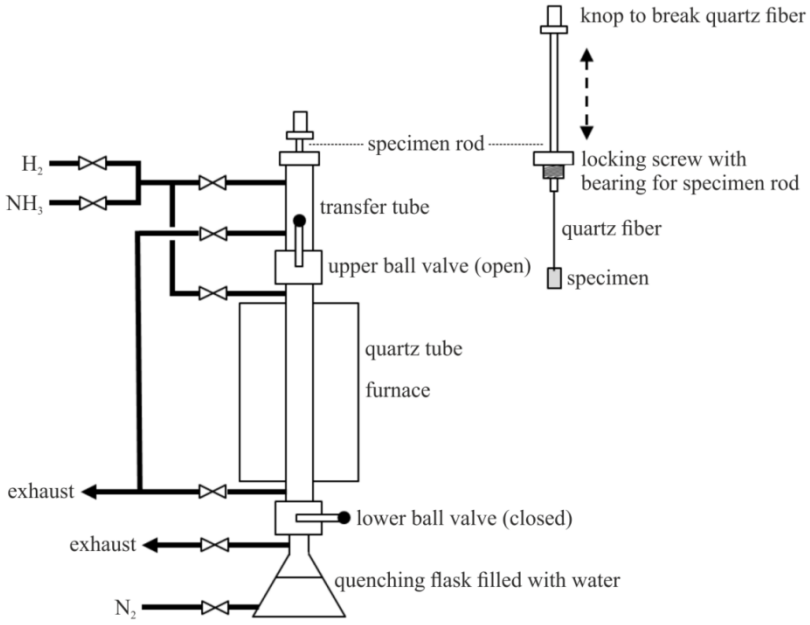

Figure 1: Schematic drawing of the employed gas nitriding facility and the specimen rod with a suspended specimen (according to Ref. [4]).

1.3. Thermodynamics of gas nitriding

The Gibbs energy (and therefore the chemical potential) is a state variable and thus the route which is followed to reach a certain (final) state, i.e. a certain value of the Gibbs energy, is not relevant for (determination of) the Gibbs energy change. As a consequence nitriding of iron in a flowing NH_3/H_2-gas mixture can be conceived as N_2 gas in contact with iron under a certain

pressure. Thus, upon gas nitriding the following hypothetical sub-reactions occur (following derivation is adopted from Refs. [3, 5]:

$$NH_3 \rightleftharpoons \frac{1}{2}N_2 + \frac{3}{2}H_2 \qquad \text{(Eq. 1a)}$$

$$\frac{1}{2}N_2 \rightleftharpoons [N] \qquad \text{(Eq. 1b)}$$

yielding

$$NH_3 \rightleftharpoons [N] + \frac{3}{2}H_2 \qquad \text{(Eq. 2)}$$

where [N] is nitrogen dissolved in the solid iron. The equilibrium reaction of Eq. 2 is only established locally at the surface (local equilibrium). If Eq. (1a) holds, it follows that:

$$\frac{1}{2}\mu_{N_2,g} = \mu_{N,s} \qquad \text{(Eq. 3)}$$

where $\mu_{N_2,g}$ and $\mu_{N,s}$ are the chemical potentials of nitrogen in the gas atmosphere and in the solid, respectively. By adopting a fugacity coefficient which is constant it follows from Eq. (3):

$$\frac{1}{2}\left[\mu^0_{N_2,g} + \ln\left(\frac{p_{N_2}}{p^0}\right)\right] = \mu^0_{N,s} + R\,T\,\ln\left(a_{N,s}\right) \qquad \text{(Eq. 4)}$$

where μ_i^0 is the chemical potential of the component *i* (with *i* = N_2,g or N,s) in the reference state (see below), R is the gas constant, *T* the absolute temperature, p_{N_2} the partial pressure of the hypothetical nitrogen gas, p^0 is the pressure of nitrogen gas in the reference state (pressure of the reference state is equal for all gas components and set to 1 atm pressure) and $a_{N,s}$ is the activity of nitrogen in the solid. By setting $\mu^0_{N,s}$ such that $1/2\,\mu^0_{N_2,g} = \mu^0_{N,s}$ one obtain:

$$a_{N,s} = \sqrt{\frac{p_{N_2}}{p^0}} \qquad \text{(Eq. 5a)}$$

and by applying the equilibrium constants, *K*, of Eqs. 1a and 2

$$K_{1a} = \frac{p_{N_2}^{1/2} \cdot p_{H_2}^{3/2}}{p_{NH_3} \cdot p^0}$$

$$K_2 = \frac{a_{N,s} \cdot p_{H_2}^{3/2}}{p_{NH_3} \cdot \sqrt{p^0}}$$

it yields to:

$$a_{N,s} = K_{1b} \cdot \sqrt{p^0} \cdot r_N = K_2 \cdot \sqrt{p^0} \cdot r_N \qquad \text{(Eq. 5b)}$$

where r_N is defined as the nitriding potential (a value for the "nitriding power"):

$$r_N \equiv \frac{p_{NH_3}}{p_{H_2}^{3/2}} \qquad \text{(Eq. 6)}$$

where p_{NH_3} and p_{H_2} are the partial pressures of the gases NH_3 and H_2, respectively. Now it is obvious that the activity of nitrogen at a certain temperature depends on the nitriding potential and thus in turn on the ratio of the partial pressures of the gases NH_3 and H_2. Further, the partial pressures can be adjusted very precisely with gas-mass flow controllers and the desired microstructure is tunable upon gas nitriding.

1.4. Microstructural evolution upon nitriding

Depending on the temperature and the nitriding potential, nitriding of (initially) pure ferritic iron can lead to the development of different iron-nitrogen phases at the specimen surface. This relationship is represented in the so-called *Lehrer* diagram (Figure 2; *E. Lehrer* presented this type of phase diagram for the first time [6]).

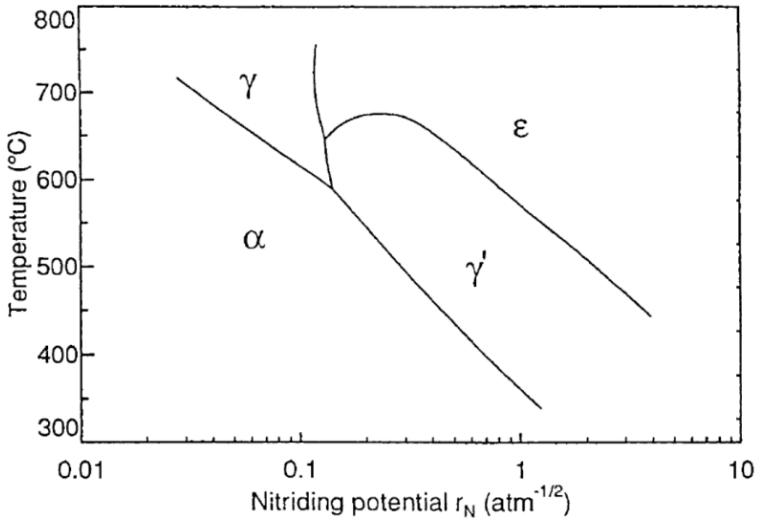

Figure 2: The Lehrer diagram depicts the occurring iron-nitrogen phases as a function of the applied gas nitriding parameters, i.e. temperature and nitriding potential, at a pressure of 1 atm (redrawn according to Ref. [7]).

In contrast to the "normal" phase diagram (Figure 3), in this potential-temperature diagram only one-phase fields occur. The reason is that for a certain temperature the nitrogen activities are the same for the two neighboring iron-nitrogen phases in equilibrium with each other and the for the (gas-) nitriding atmosphere. So the two-phase fields in the "normal" phase diagram reduce to lines in the potential diagram. The iron-nitrogen phases which are shown in the Lehrer diagram exhibit different homogeneity ranges; the metastable iron-nitrogen phase diagram (Figure 3) reveals relatively narrow homogeneity ranges for α-Fe[N] (nitrogen ferrite) and γ´-Fe_4N_{1-y}, a relatively broad homogeneity range for γ-Fe[N] (nitrogen austenite) and a very broad homogeneity range for ε-Fe_3N_{1+x} (structure and lattice parameters for the iron-nitrogen phases are gathered in Table 1).

This "normal" iron-nitrogen phase diagram is not a classical phase diagram, i.e. where the thermodynamically stable phases are presented as a function of temperature and composition at

(usually) 1 atm pressure. The iron-nitrogen phases presented in Figure 3 are unstable at 1 atm pressure and decompose into iron (solid) and nitrogen (gas) upon nitriding if the kinetics allow. Indeed, the decomposition of iron-nitrogen phases takes place at elevated temperatures and for long-time nitriding treatments leading to the formation of porosity in the nitrided region. Pore formation occurs also during the nitriding process because the iron-nitrogen phase underneath the surface, i.e. not in direct contact with the employed nitriding atmosphere, is basically an iron-nitrogen phase at elevated (nitriding) temperature at 1 atm pressure and therefore is thermodynamically unstable. Decomposition and thus porosity is not restricted to iron-nitrogen phases containing higher amounts of nitrogen, it also occurs in nitrogen ferrite but the release of Gibbs energy is smaller compared to the decomposition of nitrogen austenite or ε-Fe_3N_{1+x}, in this order.

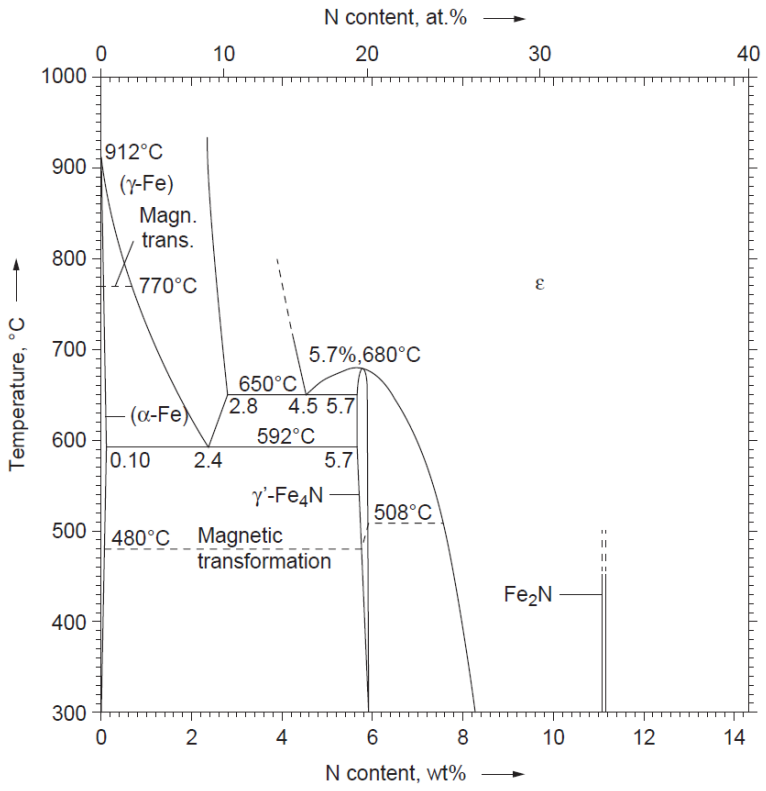

Figure 3: Section of the (metastable) iron-nitrogen phase diagram (adopted from Ref. [3]).

Table 1: Structure and lattice parameters of iron-nitrogen phases. Lattice parameters as a function of nitrogen content for α, α´, γ and ε were adopted from Ref. [8] and for γ´ from Ref. [9]. C_N is the atomic fraction of nitrogen and y_N is the atomic ratio of nitrogen with the relation $y_N = c_N/(1-c_N)$.

			lattice parameters		
Fe-N phase	alias	crystal structure	*a* / (Å)	*b* / (Å)	*c* / (Å)
α-Fe[N]	nitrogen ferrite	bcc (Im3m)	$2.8664 + 0.79 \cdot c_N$	-	-
α´-Fe[N]	nitrogen martensite	bct (Im3m)	$2.8664 - 0.18 \cdot y_N$	-	$a \cdot (2.8664 + 0.91 \cdot y_N)$
α´´-$Fe_{16}N_2$	α´´	bct (I4/mmm)	5.270	-	6.290
γ-Fe[N]	nitrogen austenite	fcc (Fm3m)	$3.572 + 0.78 \cdot c_N$	-	-
γ´-Fe_4N_{1-y}	γ´	fcc ($CaTi0_3$)	3.798	-	-
ε-Fe_3N_{1+x}	ε	hcp ($P6_3/mmc$)	$2.519 + 0.50 \cdot y_N$	-	$a \cdot (1.633 - 0.05 \cdot y_N)$
ζ-Fe_2N	ζ	(Pbcn)	4.843	5.541	4.437

1.4.1. The compound layer

Iron-nitrogen compound layers can only develop if the nitrogen activity and thus in particular the nitriding potential is high enough (cf. Lehrer diagram in Figure 2). At the early stage of the nitriding process, e.g. under conditions which comply with the ε-phase field in the Lehrer diagram, the nitrogen concentration at the surface of an (initially) ferritic component increases. If the nitrogen concentration surpasses the α-Fe[N]/ γ´-iron nitride equilibrium γ´-iron nitride will form after an incubation time at the surface. The incubation time is also affected by the competition of the nitrogen supply as a result of the ammonia dissociation at the surface, by the removal of nitrogen due to its inward diffusion and by removal of nitrogen by recombination and desorption. As a result of faster nitrogen diffusion in α-Fe[N] than in γ´-iron nitride the nuclei is

wedge-shaped whereas the tip points in the direction of the specimen´s core. Depending on the nitriding potential ε-iron nitride nucleates on the top of the γ´-iron nitride particles before the compound layer is closed. An increase in thickness of the compound layer consisting of ε- and or γ´-iron nitride requires diffusion of nitrogen from the surface trough the compound layer (cf. Figure 4). Long-time nitriding treatments, necessary to obtain compound layers with a distinctive thickness, lead to the decomposition of the iron-nitrides underneath the surface (see above) in the oldest (surface adjacent) region. The consequence of the decomposition of iron-nitrogen phases into iron and nitrogen gas is the development of pores at grain boundaries (grain boundaries are essential nucleation sites for nitrogen gas) and within grains.

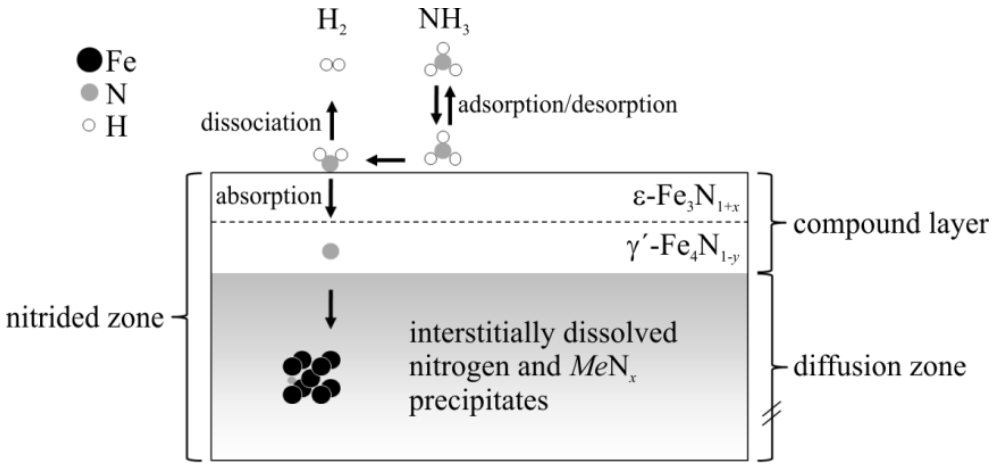

Figure 4: Schematic cross section of an iron-based ferritic specimen nitrided in the ε-phase region of the Lehrer diagram. The nitrided surface consists of the compound layer and the diffusion zone underneath. Further, the compound layer can be subdivided into the surface-adjacent ε-Fe_3N_{1+x} layer followed by the γ´-Fe_4N_{1-y} layer. In the diffusion zone the nitrogen is interstitially dissolved and/or precipitated as MeN_x (with e.g. *Me* = Al, Si, Ti, V, Cr).

Nitriding steels are alloyed with elements, *Me* (with e.g. *Me* = Al, Ti, V, Cr, Mn, Mo), having a chemical affinity for nitrogen and as a result they precipitate as $Me N_x$ upon nitriding. Depending on the strength of the interaction (for details see Section 1.4.2.) between the alloying element and nitrogen the growing compound layer is affected. A weak interaction leads to delayed precipitation of $Me N_x$ and therefore a competition between $Me N_x$ and compound layer formation takes place. At this condition the absorbed nitrogen can diffuse to large depths and thus in turn a high nitrogen supersaturation of the ferrite matrix is attained. The high nitrogen supersaturation at large depths can lead finally to e.g. γ´-plates which penetrate deeply the ferrite matrix. A strong interaction implies the instantaneous precipitation of nanosized and finely-dispersed $Me N_x$ in the nitrogen-diffusion zone and the later developing compound layer overgrows the alloying-element nitrides upon increase of thickness.

1.4.2. The diffusion zone

Nitriding of pure ferrite, i.e. no alloying elements with a chemical affinity for nitrogen are present, leads to an iron-nitrogen solid solution where the nitrogen atoms are dissolved randomly on the octahedral interstitial sites of the bcc-iron lattice. Slow cooling of nitrogen saturated specimens from high nitriding temperatures leads to the precipitation of γ´-iron nitride and upon continued cooling and high nitrogen supersaturation α´´-iron nitride precipitates. Fast cooling, i.e. quenching in water or brine, leads to a highly supersaturated iron-nitrogen solid solution and aging for days at room temperature leads also to the precipitation of α´´-iron nitride.

Steel for nitriding is alloyed with elements having a chemical affinity for nitrogen and thus the nitriding behavior of binary iron-based Fe-*Me* (with *Me* = Al, Si, Ti, V, Cr, Mn, Mo, W) model alloys was investigated extensively. It was shown that the nitriding response depends on the type

of alloying element. Therefore, the alloying elements can be grouped on the basis of the type of interaction with nitrogen [10]:

- *Strong interaction*: In the nitrided surface region (case) all alloying-element atoms precipitate instantaneously as nitrides. Consequently a sharp case/core boundary migrates to larger depths with increasing nitriding time. In this case the nitriding kinetic is rate controlled, at constant temperature, by the diffusion of nitrogen through the nitrided case. A strong interaction is observed for e.g. Ti, V and Cr (for high Cr contents).
- *Weak interaction:* The iron matrix gets saturated with nitrogen throughout the specimen´s thickness and successively the nitride precipitation occurs with the same rate at each depth below the specimen surface. In this case the nitriding rate depends on the rate of nitride-precipitation kinetic that is controlled by a combination of nucleation, growth and impingement mechanisms [11]. A weak interaction is observed for Al[A] and Si.
- *Intermediate interaction:* Moderate nitrogen-concentration gradients with diffuse case/core boundaries will occur. Intermediate interaction is observed for very low alloying element contents of Ti, V and Cr.

[A] Depending on the defect density of the ferrite matrix Al exhibits different types of interaction with nitrogen and AlN precipitates in different crystal structures: A high defect density in the ferrite matrix, i.e. high dislocation density due to cold-rolling, leads to a strong interaction of Al with nitrogen and precipitating AlN has the cubic rock-salt type crystal structure. A small defect density in the ferrite matrix, due to recrystallization (prior to the nitriding treatment), leads to a weak interaction of Al with nitrogen and AlN precipitates in the hexagonal wurtzite-type crystal structure [10].

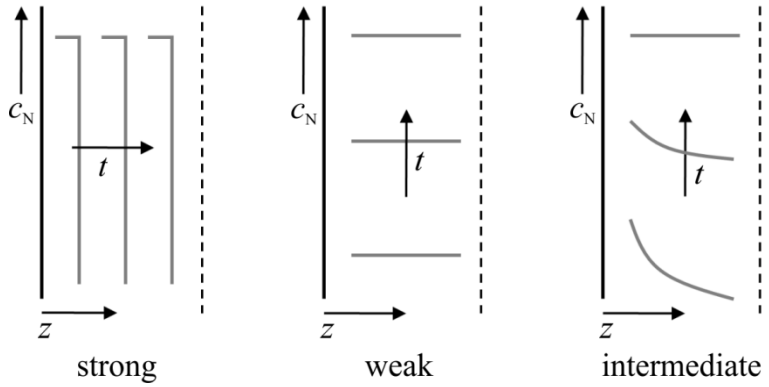

Figure 5: Schematic drawing of the types of *Me*N interactions as revealed by nitrogen concentration-depth profiles for nitrided iron-based Fe-*Me* alloys. C_N, z, and t denote nitrogen concentration, depth and time, respectively. Redrawn according to Ref. [10].

Upon nitriding binary iron-based Fe-*Me* alloys (with *Me* = Ti, Cr and V) *Me*N precipitates in the cubic rock-salt type crystal structure which is based on the fcc translation lattice; *Me* is fcc and nitrogen occupies all of the interstitial octahedral lattice sites (Figure 6a). Further, the lattice parameter of these alloying-element nitrides is very close to

$$a_{MeN} \approx a_{\alpha\text{-Fe}} \cdot \sqrt{2} = 4.05 \text{ Å} \qquad \text{(Eq. 7)}$$

where a_{MeN} and $a_{\alpha\text{-Fe}}$ are the lattice parameters of *Me*N and pure unstrained ferrite [12], respectively. As a consequence, the *Me*N precipitates grow preferentially as platelets along $\{100\}_{\alpha\text{-Fe}}$-habit planes and maintain the Baker-Nutting [13] (also called Bain) orientation relationship (OR)

$$(100)_{\alpha\text{-Fe}} \parallel (100)_{MeN}, [100]_{\alpha\text{-Fe}} \parallel [110]_{MeN} \qquad \text{(Eq. 8)}$$

with the ferrite matrix (Figure 6b) to minimize the misfit-strain energy (the misfit parallel to the $\{100\}_{\alpha\text{-Fe}}$-habit planes is in the order of only a few percent, whereas the misfit perpendicular to the $\{100\}_{\alpha\text{-Fe}}$-habit planes is in the order of 40 % and above; cf. Ref. [14]).

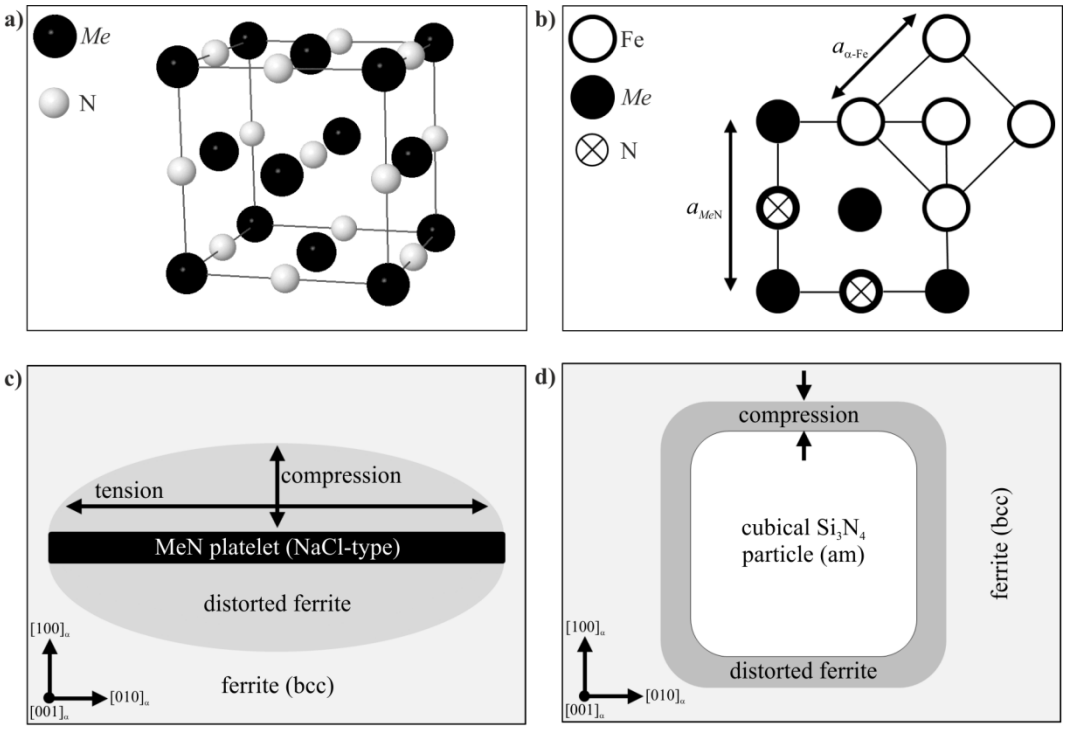

Figure 6: Schematic drawings of **a)** the cubic rock-salt type crystal structure where the *Me* (with *Me* = Ti, Cr and V) atoms are fcc and nitrogen, N, occupies all of the interstitial octahedral lattice sites. **b)** The Baker-Nutting OR (also called Bain OR). The *Me*N exhibits a smaller misfit with the ferrite matrix the closer its lattice parameter, a_{MeN}, is to $a_{\alpha\text{-Fe}} \cdot \sqrt{2}$ with $a_{\alpha\text{-Fe}}$ is the (unstrained) ferrite-lattice parameter. **c)** A (semi-) coherent *Me*N platelet in the ferrite matrix and **d)** a cubical, fully incoherent, amorphous Si_3N_4 particle in the ferrite matrix.

Thus the *Me*N precipitates exhibit a platelet-like morphology and they maintain (initially) a coherent interface parallel to the $\{100\}_{\alpha\text{-Fe}}$-habit planes and an incoherent interface perpendicular to the $\{100\}_{\alpha\text{-Fe}}$-habit planes. As a consequence, the ferrite matrix parallel to the coherent *Me*N/α-Fe interface is under tensile stress and thus in turn the ferrite matrix perpendicular to the coherent *Me*N/α-Fe interface is under compressive stress (Figure 6c). The larger the misfit between *Me*N particle and ferrite matrix, i.e. the larger the difference between lattice parameter of *Me*N and $a_{\alpha\text{-Fe}} \cdot \sqrt{2}$, i.e. the larger is the amount of developing stress. By comparing the lattice parameters of the *Me*N, the misfit and thus the ferrite distortion around *Me*N precipitates is expected to be highest for TiN, followed by CrN and smallest for VN.

In case of large differences in the type of crystal structure between nitride and ferrite matrix *Me*N particles precipitate in morphologies different to that of platelets; for instance, nitriding of iron-based Fe-Si alloys lead to the precipitation of (initially) cubical particles [15-18] which transform at high nitriding temperatures or for very long nitriding time in particles with an octapod-shape (eight-legged particles) [19]. Although the release of chemical Gibbs energy is quite large upon formation of Si_3N_4 the nucleation and especially growth of Si_3N_4 particles in the ferrite matrix is difficult and thus practically weak nitriding kinetics (Figure 5) are observed upon nitriding iron-based Fe-Si alloys. The difficult nucleation and growth is based on a very large volume misfit of more than 100 % between the Si_3N_4 particle and the ferrite matrix. Further, cubical Si_3N_4 particles are of amorphous nature which is very unlikely for precipitates in a crystalline matrix. The amorphous state of the Si_3N_4 particles can be explained as follows: Relatively small particles exhibit a large interface/volume ratio and thus the interfacial energy plays an important role. The amorphous state indicates that the interfacial energy for an amorphous/crystalline interface is smaller than for a crystalline/crystalline interface and therefore

favored [16]. Moreover, the cubical Si_3N_4 particles maintain a specific OR with the ferrite matrix despite their amorphous nature. The cube faces are parallel to $\{100\}_{\alpha\text{-Fe}}$ planes (Figure 6d) indicating that this interface has the smallest (amorphous/crystalline) interfacial energy. As mentioned above, for higher nitriding temperatures and/or very long nitriding time a gradual transformation of the Si_3N_4 particles occur from a cuboidal to an octapod shape [19]. This change in morphology is a consequence of the large volume misfit of Si_3N_4 particles with the ferrite matrix and the elastically anisotropic nature of the ferrite matrix – leading in combination to the preferred growth along $\langle 111 \rangle_{\alpha\text{-Fe}}$ directions. Upon nitriding an iron-based Fe-Si alloy at relatively high temperatures the formation of rod-like crystalline α-Si_3N_4 was also observed [19].

Most research on nitriding of iron-based alloys has been focused on the nitriding of binary iron-based Fe-*Me* alloys. In contrast, commercial nitriding steels contain series of different alloying elements, each exhibiting its own interaction behavior with nitrogen. Due to the difficulty to separate the effects resulting from a single alloying element in multi-alloyed casts, only few projects were carried out to investigate the nitriding behavior of ternary iron-based Fe-Me_a-Me_b alloys (e.g. Fe-Mn-Si [20], Fe-Al-Cr [21-23], Fe-Ti-Cr [24, 25], Fe-Al-Si [26]). All nitrided ternary iron-based alloys developed ternary nitrides, $Me_{a(1-x)}Me_{b(x)}N$ (so-called "mixed nitrides"), instead of separately precipitating binary Me_a and Me_b nitrides. Ternary nitrides develop if the character of the alloying elements and their binary nitrides is alike; e.g. nitriding of ternary Fe-Al-Cr alloys [21-23] or Fe-Ti-Cr [24, 25] alloys lead to the precipitation of metastable mixed $Cr_{1-x}Al_xN$ or $Cr_{1-x}Ti_xN$, respectively. The formation of the mixed ternary $Cr_{1-x}Al_xN$ is explained by differences in the precipitation kinetics of CrN and AlN (precipitation of AlN is slower than that of CrN due to a larger volume misfit with the ferrite matrix) and by the large misfit-strain energy in connection with CrN precipitation which is reduced upon incorporation of Al in CrN. Further, the replacement of Cr by Al is eased due to the fact that AlN can also

precipitate in the cubic rock-salt type crystal structure similar to CrN (see above). A similar explanation can be given for the formation of the mixed ternary $Cr_{1-x}Ti_xN$. In this case the (even higher) misfit-strain energy due to the precipitation of TiN is reduced by the incorporation of Cr in TiN. Despite the considerable release of Gibbs energy upon the formation of mixed nitrides the formation of separate binary equilibrium nitrides is favored. Annealing experiments at temperatures higher than the nitriding temperature after the formation of mixed $Cr_{1-x}Al_xN$ leads to Al depletion in the mixed nitrides and to the subsequent precipitation of hexagonal AlN within ferrite-matrix grains and at grain boundaries [22].

Nitriding of alloys which contain elements forming highly coherent MeN_x (with *Me* = Ti, Cr, V, Mo) showed, that the nitrogen content after homogenously through nitriding exceeds the expected nitrogen content for precipitation of stoichiometric MeN and the equilibrium amount of nitrogen dissolved in the ferrite matrix. This difference between the predicted (theoretical) amount of nitrogen and the amount of determined nitrogen is called "excess nitrogen". Dedicated research revealed the existence of three types of nitrogen depending on the absorption site:

- *Type I*. This type of nitrogen is strongly bonded in the nitride precipitates and is, in comparison with the other types, the most stable one. Upon denitriding in a reducing H_2 atmosphere the strongly bonded nitrogen can (usually) not be removed.
- *Type II*. The nitrogen atoms are absorbed at the coherent interface between the nitride platelet and ferrite matrix. In case of nitrides exhibiting the rock-salt type crystal structure and the Baker-Nutting OR the nitrogen atoms occupy the octahedral interstitial lattice sites in the ferrite matrix opposite to the *Me* atoms in the *Me*N platelet. This type of nitrogen belongs to excess nitrogen and can be relatively easy removed upon denitriding due to the less strong binding.

- *Type III*. Precipitation of (semi-) coherent *Me*N-platelets lead to a misfit-strain field which surrounds the *Me*N platelet and as a consequence the ferrite matrix is tetragonal distorted (Figure 6c). The hydrostatic stress component with a tensile nature enhances the nitrogen solubility and thus larger nitrogen contents are possible in the direct vicinity of *Me*N platelets as the nitrogen equilibrium solubility in ferrite. This type of nitrogen belongs also to excess nitrogen and is easily removed upon denitriding.

1.5. Outlook of the thesis

Nitriding is a thermochemical surface treatment widely employed to improve the mechanical (resistances against wear and fatigue) and chemical (resistance against corrosion) properties of ferritic steel components. However, due to the lack of fundamental knowledge of the nitriding process, its commercial application in industries is still based on empiricism. As compared to other variants of nitriding (e.g. salt-bath or plasma nitriding), the gas nitriding process has the advantage of precise control of thermodynamic equilibrium between the solid component and the gas atmosphere. Thereby gas nitriding is the preferred choice for understanding the nitriding reaction in steel substrates. Understanding the precipitation of internal nitrides in nitrided iron-based alloys also serves as a model to understand the precipitation reactions in solids in general. This thesis is devoted to understand the development of internal nitrides in iron-based alloys.

In literature, many investigations on the precipitation of strong nitride forming alloying elements, i.e. Ti, Cr, V, as cubical rock-salt type crystal structured nitrides exists. The precipitation process of alloying elements as nitrides, of more complex crystal structure (e.g. Si, Mo, W), has been investigated only sparsely. Against this background, an iron-based binary Fe-W alloy was investigated to understand the crystal structure and morphology of tungsten-nitride particles developed upon nitriding (**Chapter 2**).

In the past series of studies were undertaken to gain fundamental knowledge on the iron-nitride compound layer development on pure iron and binary iron-based alloys. Long-time nitriding treatments are known to result in the development of porosity in the iron-nitride compound layers. However, the information about the influence of different alloying elements, present in iron (steel), on the pore formation, especially in the diffusion zone (ferrite/austenite with dissolved nitrogen and/or alloying-element nitride particles) is lacking. Against this background, in this thesis, long-time nitriding experiments were performed on pure iron and several binary iron-based Fe-*Me* alloys (with *Me* = Al, Si, Cr, Co, Ni and Ge) to understand the mechanisms of pore formation in more detail (**Chapter 3**). Two sets of nitriding parameters were applied to the specimens in order to investigate pore formation under ferrite and austenite stabilizing conditions. Porosity development showed a dependence on the ease with which alloying element nitrides develop in the ferrite matrix, matrix (ferrite/austenite) hardening upon internal nitrides development and the availability of nucleation sites for the pores (i.e. grain boundaries).

The fundamental knowledge about solid-state precipitation processes involving significant volume misfits between precipitating particles and matrix is incomplete. The reason is the complexity of interaction of generated misfit strains with the thermodynamics and the kinetics of the reactions. The research presented in the **Chapter 4** and **Chapter 5** were undertaken to reveal the role of magnitudes of coherency strains of the matrix on the nucleation and growth of precipitating particles. To this end, iron-based ternary Fe-*Me*-Si alloys (with *Me* = Ti, Cr, V) were nitrided to investigate the influence of the misfit strains induced into matrix by the fast precipitating misfitting *Me*N on later slowly precipitating misfitting *amorphous* Si_3N_4 particles. In contrast to previously investigated iron-based ternary Fe-Al-Cr and Fe-Ti-Cr alloys, no so-called “mixed” nitrides developed in the nitrided Fe-*Me*-Si alloys. In a first stage all *Me*

precipitates as *Me*N and subsequently, in a second stage, all Si precipitates as Si_3N_4. The *Me*N are precipitating as crystalline, finely dispersed, nanosized platelets which obey the Baker-Nutting orientation relationship with respect to the ferrite matrix. The subsequently developing Si_3N_4 particles precipitate with a cubical morphology and are amorphous. It was shown that the Si_3N_4-precipitation rate depends strongly on the degree of coherency of the first precipitating *Me*N and the different Si_3N_4-precipitation kinetics were ascribed to the different time dependences of the coherent → incoherent transitions of the *Me*N particles in the different Fe-*Me*-Si alloys.

Chapter 2

The Process of Tungsten-Nitride Precipitation upon Nitriding Ferritic Fe-0.5 at.% W Alloy

Benjamin Schwarz, Regina E. Hörth, Ewald Bischoff,

Ralf E. Schacherl and Eric J. Mittemeijer

Abstract

The precipitation of tungsten nitride upon internal nitriding of ferritic Fe- 0.5 at.% W alloy was investigated at 610 °C in a flowing NH_3/H_2 gas mixture. Different tungsten nitrides developed successively; the thermodynamically stable hexagonal δ-WN could not be detected. The state of deformation of the surface plays an important role for the development of tungsten nitride at the surface. The morphologies of the tungsten nitrides developed at the surface and those precipitated at some depth in the specimen are different. The nitride particles at the surface exhibit mostly an equiaxed morphology (with the size of the order 0.5 μm) and have a crystal structure which can be described as a superstructure derived from hexagonal δ-WN. These nitride particles show a strong preferred orientation with respect to the specimen frame of reference but have no relation with the crystal orientation of the surrounding ferrite matrix. In the bulk, nano-sized and finely dispersed platelet-like precipitates grow preferentially along $\{100\}_{\alpha\text{-Fe}}$. It is unclear whether these precipitates consist of binary iron nitride α´´-$Fe_{16}N_2$ or of a ternary Fe-W-N. Additionally to the finely dispersed particles, bigger nitrides at ferrite grain boundaries develop exhibiting platelet-type morphology and possessing a crystal structure which can be also described as a superstructure derived from hexagonal δ-WN. Upon prolonged nitriding assumed

discontinuous precipitation of the initially precipitated finely dispersed nitrides starts from the ferrite-grain boundaries resulting in lamellas consisting of alternate ferrite and hexagonal nitride lamellas, whereas the nitride lamellas having a Pitsch-Schrader orientation relationship with the surrounding ferrite matrix. The nitrides precipitated upon nitriding in the bulk were found to be unstable during H_2 reduction at 470 °C. Remarkably, upon such low temperature dissolution of the nitrides took place but only the nitrogen from the nitride particles could diffuse out of the nitride platelets and the specimen, leaving W-rich regions (W-"clusters") at the location of the original precipitates.

2.1. Introduction

Nitriding as a thermochemical surface treatment is widely employed to improve the surface properties of steel workpieces: The resistance against fatigue, wear and corrosion is increased (very) pronounced [1, 27]. The improvement of the (mechanical) properties by nitriding is a result of precipitating alloying element nitrides in the nitrided zone.

Little is known about the precipitation of tungsten nitride, which can happen upon nitriding of W containing steel (e.g. High Speed Steels [28]). A two stage precipitation process of tungsten nitride in Fe-W alloys has been proposed in Ref. [29]: Continuous precipitation of metastable ternary Fe-W-N, which subsequently transforms to equilibrium hexagonal δ-WN/δ`-W(N,O) through a discontinuous precipitation reaction. However, as the maximum solubility of W in ferrite is about 0.5 at.% at 600 °C [30], and the Fe-W alloys (0.6 at.% to 1.6 at.% W) investigated in Ref. [29] contained more than 0.5 at.% W, it can be suggested that these alloys were not fully ferritic: The thus expected precipitation of the metastable Laves phase Fe_2W can influence the WN precipitation. In the present study the binary Fe- 0.5 at.% W alloy was nitrided to investigate the W-N precipitation in ferrite.

Before nitriding the completely ferritic nature of the Fe- 0.5 at.% W alloy was validated with X-ray diffraction (XRD) and transmission electron microscopy (TEM).

2.2. Experimental procedures

2.2.1. Specimen preparation and nitriding/denitriding

A Fe-0.5 at.% W alloy was prepared from element granules of Fe (purity 99.98 wt.%) and W (purity 99.99 wt.%). The granules were molten in an induction furnace under a protective Ar atmosphere and cast to a rod with the dimensions of (100 × 10) mm. The amount of tungsten and light element impurities in the produced cast are shown in Table 1. The cast rod was cold rolled to obtain a sheet of about 0.2 mm thickness. From the sheet rectangular specimens (lateral dimensions 10 mm × 15 mm) were cut, ground and polished (final stage with 1 µm diamond suspension) from all sides and ultrasonically cleaned in ethanol. Specimens were then encapsulated in a quartz tube under protective Ar atmosphere and recrystallized at 800 °C for 20 min. Before nitriding, the specimens were either ground (SiC P4000 grinding paper) or polished (1 µm diamond suspension) and again ultrasonically cleaned.

Table 2: Concentrations of W and light element impurities in the Fe- 0.5 at.% W alloy.

alloy	W (wt.%)	W (at.%)	O (µg/g)	N (µg/g)	C (µg/g)	S (µg/g)
Fe-0.5 W	1.63 ± 0.02	0.50 ± 0.01	90 ± 10	< 10	23 ± 6	< 20

The gas nitriding facility consists of a vertical multizone quartz-tube furnace (diameter 28 mm; temperature control within ± 1°C) and calibrated gas mass-flow controllers. Each specimen was suspended with a quartz fiber in the defined temperature zone in the furnace. The applied

nitriding temperature was 610 °C and the gas fluxes were adjusted to 45 ml/min for NH_3 (purity 99.998 vol.%) and to 455 ml/min for H_2 (purity 99.999 vol.%)) to establish a nitriding potential [5] of 0.104 $atm^{-1/2}$. For these applied nitriding parameters no iron nitrides can develop (cf. the Lehrer-diagram [6]). The nitriding treatment was either interrupted by quenching the specimen into a flask filled with N_2 purged water or the specimens were slowly cooled to room temperature under a N_2 gas flow in the furnace. The same furnace was used for denitriding the specimens. Denitriding was performed at 470 °C in flowing H_2 gas (400 ml/min) for 72 hours.

2.2.2. Specimen characterization

X-ray diffractograms were recorded with a PANalytical X´Pert MPD (Multi-purpose diffractometer) for phase analysis. To this end the XRD-patterns recorded from the surface of the nitrided specimens were analyzed employing the software X´Pert HighScore and utilizing the data-base of the International Center for Diffraction Data (ICCD) [12]. In order to obtain cross-sections for metallographic analysis, specimens were cut perpendicular to the nitrided surface and embedded in Struers Polyfast using a Struers LaboPress. The cross-sections were ground, polished (final stage employing 1 µm diamond paste) and etched with 2 vol.% Nital for 30 seconds.

Scanning electron microscopy (SEM) investigations were carried out on the etched and nitrided cross-sections with a JEOL JSM-6400 using an acceleration voltage of 15 kV and a working distance from 15 mm – 17 mm.

In order to determine phase- and orientation maps by electron back-scatter diffraction (EBSD) a Zeiss LEO 438 VP SEM (acceleration voltage 20 kV) equipped with a high-speed camera and the analyzing software OIM 5.31 (Ametek EDAX/TSL) was applied.

TEM specimens were prepared in ways similar to those described in [17], either by electropolishing or by ion milling. Bright-field (BF), dark-field (DF) diffraction contrast images and selected area diffraction patterns (SADP) were recorded with a Gatan CCD camera attached to the used Philips CM 200 TEM applying an acceleration voltage of 200 kV.

2.3. Results and discussion

2.3.1. Effect of surface preparation; the development of surface nitrides

XRD-patterns were recorded from recrystallized Fe- 0.5 at.% W alloy specimens nitrided for 24 hours at 610 °C using a nitriding potential of 0.104 $atm^{-1/2}$. The XRD-patterns obtained for a nitrided specimen which was ground before nitriding and for a specimen which was polished before of nitriding are shown in Figure 7. The ground specimen exhibits, in addition to ferrite reflections, strong reflections corresponding to a superstructure which can be derived from hexagonal δ-WN: the observed additional reflections match best with reflections expected for $FeWN_2$ or $W_{2.56}N_4$. These additional reflections could be also associated with δ`-W(N,O). However, the development of δ`-W(N,O) was reported by Stephenson *et al.* [29], as occurring due to the presence of oxygen in the nitriding gas mixture (NH_3/H_2). Such contamination could be avoided in the present work because of the high purity of the gases used. Strikingly, only diffraction peaks pertaining to basal planes of the hexagonal δ-WN type phase are observed (see Figure 7) and this suggest the development of a sharp texture of this phase in the specimen frame of reference. The relatively high intensities of the $\{0002n\}$ peaks of the δ-WN type phase, in comparison to the ferrite peaks, indicate a relatively high volume fraction of this phase at the surface of the specimen. In contrast with the above, for the specimen which was polished before nitriding no peaks other than from ferrite were detected (Figure 7).

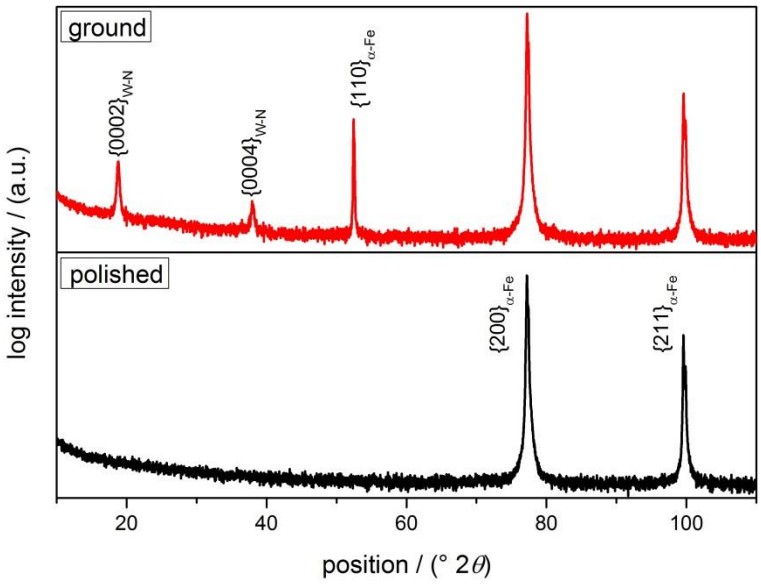

Figure 7: XRD-patterns (Co-K_α radiation) recorded from the surface of Fe- 0.5 at.% W alloy specimens nitrided for 24 hours at 610 °C using a nitriding potential of 0.104 $atm^{-1/2}$. Grinding before nitriding leads to additional reflections from basal planes of a hexagonal nitride phase, whereas the specimen which was polished before nitriding shows only ferrite reflections.

An EBSD analysis of the surface of the specimen which was ground before nitriding for 24 hours is shown in Figure 8. The EBSD phase map (Figure 8a) shows individual hexagonal nitrides (green; δ-WN type) at locations of the surface. Their morphology is mostly equiaxed or sometimes elongated. The corresponding EBSD orientation map (Figure 8b) confirms the strong $\{0001\}$ -texture of the δ-WN type surface nitrides. The ferrite matrix grains do not exhibit a clear preferred orientation.

As no distinct orientation relationship is observed for the δ-WN type particles at the surface and the ferrite matrix, it is suggested that a favorable $\{0001\}_{W\text{-}N}$ -surface energy during the nitriding treatment led to the development of δ-WN type particles with a $\{0001\}$ plane at the

surface. Indeed, close packed surfaces (here $\{0001\}_{W\text{-}N}$) are known to have a relatively low surface energy [31].

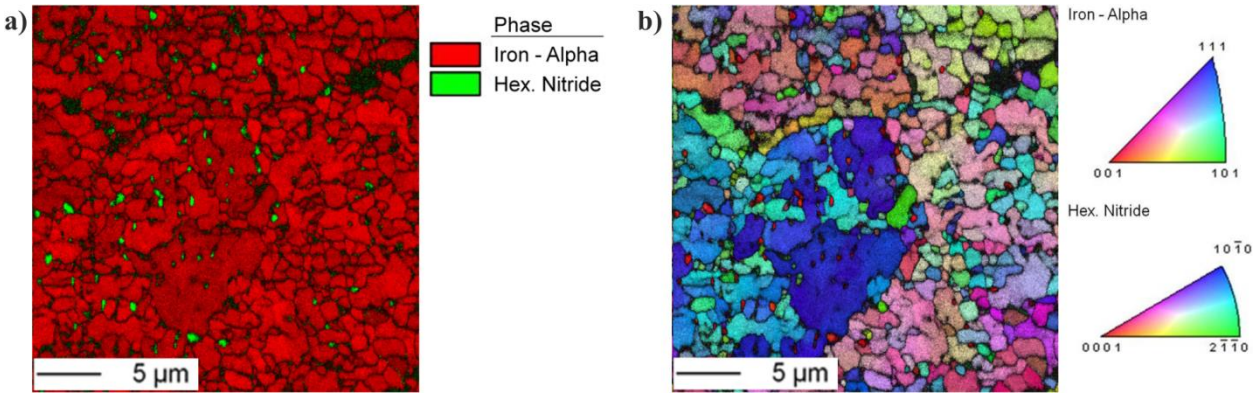

Figure 8: EBSD maps recorded from the surface of a Fe- 0.5 at.% W alloy specimen nitrided for 24 hours at 610 °C using a nitriding potential of 0.104 $atm^{-1/2}$. **a)** Phase map showing hexagonal surface nitrides (green) and ferrite-matrix grains (red). **b)** Orientation map demonstrating strong $\{0001\}$ -texture of the surface nitrides and a more or less random orientation of the ferrite-matrix grains.

2.3.2. Development of nitrides in the bulk

TEM analysis of the specimen nitrided at 610 °C using a nitriding potential of 0.104 $atm^{-1/2}$ showed that after short nitriding times of 2 hours precipitation of finely dispersed and nano-sized precipitates takes place (see Figure 9a). These tiny and finely dispersed precipitates preferentially grow along $\{100\}_{\alpha\text{-}Fe}$ planes.

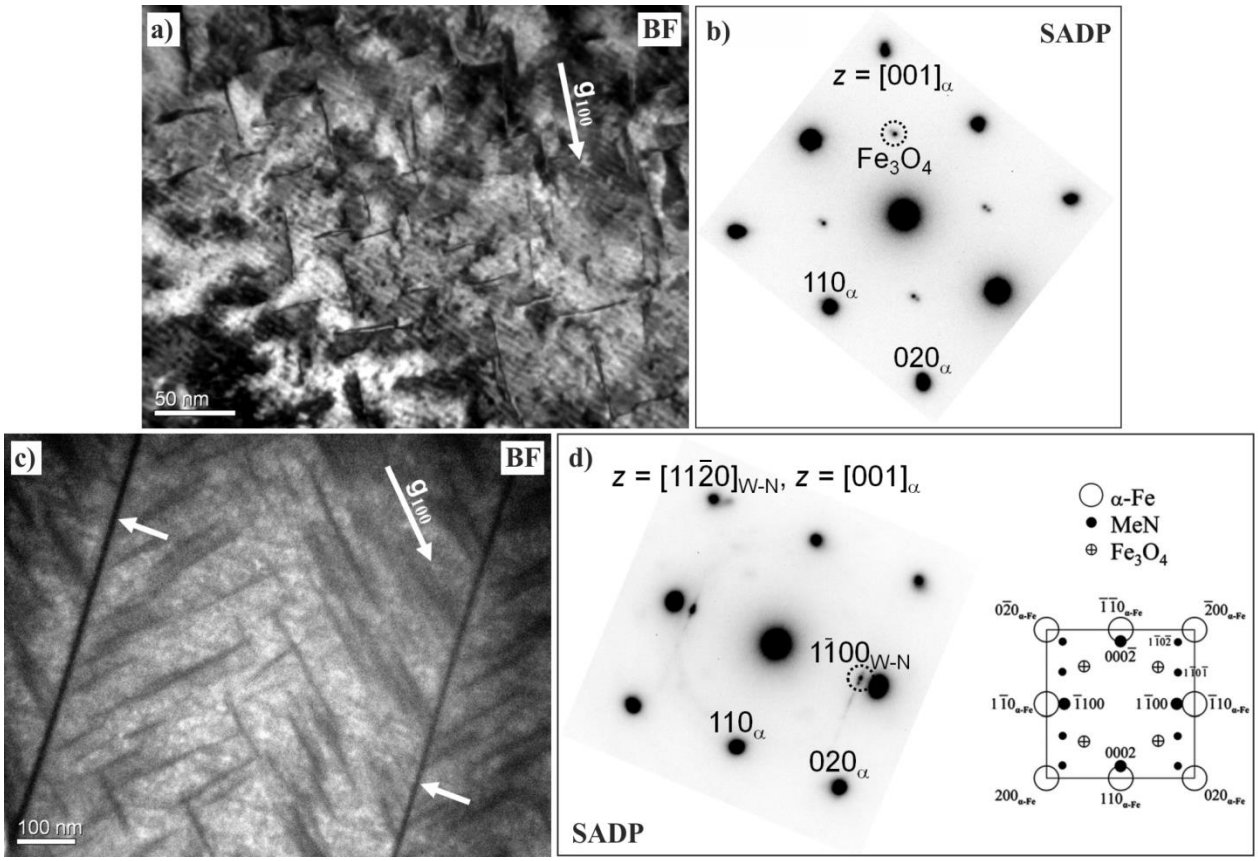

Figure 9: TEM images recorded from Fe- 0.5 at.% W alloy specimens nitrided at 610 °C using a nitriding potential of 0.104 $atm^{-1/2}$. **a)** TEM BF image from a specimen nitrided for 2 hours showing finely dispersed nano-sized precipitates growing preferably along $\{100\}_{\alpha\text{-Fe}}$ planes. Corresponding SADP in **b)**, shows only diffraction spots from ferrite and iron oxide (Fe_3O_4). **c)** TEM BF image from a specimen nitrided for 72 hours showing two very thin nitride lamellas (the dark lines indicated with arrows). The much shorter and smaller platelets in the ferrite matrix are finely dispersed α´´-$Fe_{16}N_2$ platelet-like precipitates. The corresponding SADP in **d)**, show additional diffraction spots which can be indicated as a superstructure of hexagonal δ-WN. The schematic TEM diffraction pattern ($001_{\alpha\text{-Fe}}$ incident electron beam axis) show reflex positions for a Pitsch-Schrader OR between bcc ferrite and hdp nitride [22].

In the corresponding SADP (Figure 9b) only diffraction spots from ferrite and iron-oxide are visible. As described in Ref. [32], it is difficult to obtain diffraction from α´´ due to small transformation strain and slightly different orientation relationships. Therefore it is unclear whether these precipitates consist of the binary iron nitride α´´-$Fe_{16}N_2$ or of a ternary Fe-W-N as described by Stephenson *et al.* [29]. Additionally to the finely dispersed particles, the precipitation of nitrides at ferrite grain boundaries with a platelet-like morphology occurs. These precipitates have a lateral dimension between 100 nm to 1 µm and a thickness of only a few atomic layers. Their crystal structure can be again described as a superstructure derived from hexagonal δ-WN. Continued nitriding (> 8 hours at 610 °C) led to the development of a lamellar microstructure composed of alternate ferrite and hexagonal nitride lamellas (see Figure 9c, nitride lamellas are indicated with arrows). The corresponding SADP (inset in Figure 9d) shows ferrite and additional diffraction spots from a hexagonal nitride lamella. The nitride lamellas exhibit a Pitsch-Schrader orientation relationship $(110)_{\alpha\text{-}Fe} \parallel (0001)_{W\text{-}N}, [001]_{\alpha\text{-}Fe} \parallel [11\bar{2}0]_{W\text{-}N}$ [33] with respect to ferrite matrix (cf. schematic TEM diffraction pattern in Figure 9d). The extra spots can be again indicated as a superstructure of hexagonal δ-WN. It may be suggested that the microstructure is a result of a discontinuous precipitation reaction where the initial finely dispersed Fe-W-N phase with the α´´-$Fe_{16}N_2$ like crystal structure is replaced. Surprisingly, after the coarsening there are still finely dispersed α´´-$Fe_{16}N_2$ like precipitates in the direct vicinity of the hexagonal nitrides (see Figure 9c). In addition to the metastable Fe-W-N phase, precipitation of α´´-$Fe_{16}N_2$ is expected due to room temperature aging of the nitrided specimens [34].

A specimen nitrided for 48 hours at 610 °C using a nitriding potential of 0.104 $atm^{-1/2}$ was subjected to denitriding for 72 hours at 470 °C under pure H_2 gas flow. The nitrogen content after nitriding was 0.45 at.% and after denitriding 0.03 at.%. Therefore, nearly all nitrogen diffused out of the specimen during the denitriding treatment which indicates the instability of developed

nitrides at 470 °C in reducing H_2 atmosphere. However, SEM investigation of the cross-section of the denitrided specimen showed similar to the nitrided specimens still plate-like structures along grain boundaries and lamellar structures emanating from the grain boundaries (see Figure 10).

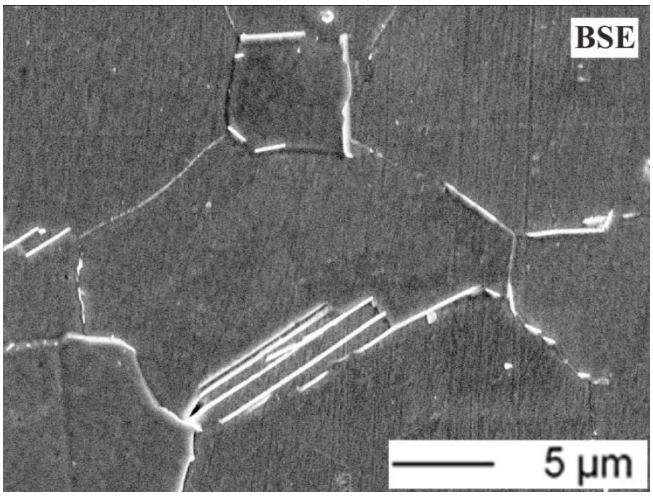

Figure 10: SEM BSE image recorded from the etched cross-section of Fe- 0.5 at.% W alloy specimen nitrided for 48 hours at 610 °C using a nitriding potential of 0.104 $atm^{-1/2}$. After nitriding the specimen was denitrided for 72 h at 470 °C under pure H_2 gas flow. During the denitriding process the specimen lost nearly all nitrogen, hence leaving W-rich regions ("W-clusters") at the location of the former nitride precipitates (bright contrast) along ferrite-grain boundaries and as lamellar colonies within the ferrite grains.

At the denitriding temperature interstitially dissolved nitrogen and the nitrogen coming from the dissolving W-N can easily diffuse out of the specimen, whereas the mobility of W as a substitutional-alloying element is not high enough to diffuse away. Hence, it can be suggested that upon denitriding W remains at the location of the original nitride platelets leading to W

enrichments ("W-clusters") at the location of original precipitates. This can be clearly distinguished by SEM using back-scatter electron (BSE) contrast.

2.4. Conclusions

- Tungsten-nitride precipitation occurred both in the bulk and, depending on surface preparation, at the surface of the nitrided specimens. The crystal structure of the developed tungsten nitrides is a superstructure of hexagonal δ-WN.
- The surface-nitride development is due to a certain degree of deformation of the surface.
- Nitrides which developed in the bulk have a platelet morphology. Their crystal structure can (also) be conceived as a superstructure of hexagonal δ-WN. Prolonged nitriding leads to lamellar structures (colonies) of these nitrides composed of nitride and ferrite lamellae due to a discontinuous precipitation reaction. The nitrides with platelet morphology exhibit a Pitsch-Schrader orientation relationship with the surrounding ferrite matrix.
- The nitrides in the bulk are unstable with respect to hydrogen reduction at 470 °C, which results in their dissolution leaving W-rich regions ("W-clusters") at the locations of the original nitride precipitates, due to the very low diffusivity of W in ferrite at 470 °C.

Acknowledgements

We thank Mr. P. Kress and W. Engelhardt for the nitriding experiments, Mrs. S. Kühnemann for SEM investigation, W.-D. Lang for TEM sample preparation and Dr. Meka for discussion (they are all with the Max Planck for Intelligent Systems).

Chapter 3

Pore Formation upon Nitriding Iron and Iron-based Alloys; The Role Alloying Elements and Grain Boundaries

Benjamin Schwarz, Holger Göhring, Sai R. Meka,

Ralf E. Schacherl and Eric J. Mittemeijer

Abstract

Pure iron and a series of iron-based Fe-*Me* alloys (with *Me* = Al, Si, Cr, Co, Ni and Ge) were nitrided in a NH_3/H_2 gas mixture at 650 °C (923 K). Different nitriding potentials were applied to investigate the development of pores under ferrite and austenite stabilizing conditions. In all cases pores developed in the nitrided microstructure, i.e. also and strikingly pure ferritic iron exhibited pore development. The pore development is shown to be caused by the decomposition of (homogeneous) nitrogen-rich Fe(-*Me*)-N phase into nitrogen-depleted Fe(-*Me*)-N phase and molecular N_2 gas. The latter, gas phase can be associated with such high pressure that the surrounding iron-based matrix can yield. Thermodynamic assessments indicate that continued decomposition, i.e. beyond the state where yielding is initiated, is possible. Precipitating alloying-element nitrides, i.e. AlN, CrN or Si_3N_4, in the diffusion zone below the surface, hinder the formation of pores due to the competition of alloying-element nitride (Me_xN_y) precipitation and pore (N_2) development; alloying elements reducing the solubility of nitrogen enhance pore formation. No pore formation was observed upon nitriding a single crystalline pure iron specimen, nitrided under ferrite stabilizing conditions, thereby exhibiting the essential function of grain boundaries for nucleation of pores.

3.1. Introduction

Nitriding is a thermochemical surface treatment applied to improve the mechanical and chemical properties of ferritic steel components [1-3]. The nitrided zone can be subdivided into an outer iron-nitride compound layer, consisting of ε-Fe_3N_{1+x} and/or γ′-Fe_4N_{1-y}, on top of a diffusion zone of nitrogen in the ferrite matrix. The nitrogen in the diffusion zone is dissolved interstitially (at the nitriding temperature) and/or precipitated as nano-sized alloying-element nitride particles in case the matrix has been alloyed with nitride forming elements, *Me*, such as Al, V, Cr, etc..

Formation of pores in the *iron-nitride compound layer* is a well-known phenomenon [35-39]. The pores can occur within the grains and along the grain boundaries of the iron-nitride layer. The coalescence of individual pores at the grain boundaries results in opened grain boundaries/micro-cracks. Pores, in the form of "open" grain boundaries in contact with the outer surface, can be beneficial due to their function as reservoirs for lubricants to provide better tribological performance [40], but in general pores are detrimental due to the associated mechanical weakening of the material.

Different, contradictory mechanisms have been presented in the literature for pore formation in the iron-nitride compound layer upon nitriding; see the overview presented in Ref. [38]. The most widely accepted theory is based on the thermodynamic instability of the iron-nitride phases [7, 35, 36]: iron-nitride phases which are not in direct contact with the nitriding atmosphere (NH_3/H_2 gas mixture or nitrogen plasma or salt bath) are, at the usual applied temperatures and pressures, thermodynamically unstable and tend to decompose into molecular N_2 gas and iron.

Development of pores upon nitriding is not restricted to the iron-nitride compound layer. Pores can occur as well in the *diffusion zone*, underneath the iron-nitride compound layer, although this has been noticed rarely in the literature: Nitriding of pure iron, employing nitriding parameters

(temperature and nitriding potential) corresponding with the austenite-phase region of the Lehrer diagram [6], resulted in the growth of nitrogen-austenite from the surface accompanied by the development of pores along the austenite-grain boundaries below the surface [41]. Upon prolonged nitriding of iron-based Fe-*Me* alloys, employing nitriding parameters corresponding with the ferrite-phase region of the Lehrer diagram, pores can develop below the surface along grain boundaries in the ferritic matrix [42-44].

Until now the attention was largely devoted to pore development in the iron-nitride compound layer, whereas little attention was paid on pore development in nitrogen ferrite and nitrogen austenite. Yet, as shown in this work, such pore formation in the nitrogen-diffusion zone is a generally occurring phenomenon, leading to pore fractions of possibly 10 vol.% and more, and thus may have a pronouncedly negative effect on the mechanical properties. As commercial nitriding steels are usually alloyed with a series of alloying elements, it is essential to understand the influence of the dissolved alloying elements and/or the developing alloying-element nitride particles on the pore formation in nitrogen-diffusion zones of nitrided steels.

Against the above background, the current project aims at understanding of (i) the development of porosity in pure nitrogen ferrite and in pure nitrogen austenite and (ii) the effects of alloying elements (*Me* = Al, Si, Cr, Co, Ni and Ge) on pore formation in ferrite and austenite. In order to reveal the role of grain boundaries on pore formation, experiments have also been performed on single crystal iron specimens.

3.2. Thermodynamics of gas nitriding and pore formation

At a given temperature, a specific chemical potential of nitrogen in a solid iron-nitrogen phase Fe[N] (as α-Fe[N] (nitrogen ferrite), γ-Fe[N] (nitrogen austenite) and the iron nitrides γ'-Fe_4N_{1-y} and ε-Fe_3N_{1+x}) and thus a certain nitrogen concentration (activity) in the phase concerned, can in

principle be realized (actually, at the surface of the solid substrate; see what follows) by imposing an outer gas atmosphere of pure N_2 gas at very high pressure. The corresponding equilibrium can be described as:

$$\frac{1}{2}N_2 \rightleftharpoons [N] \qquad \text{(Eq. 9)}$$

where [N] denotes nitrogen dissolved in the solid substrate. The (hypothetical) N_2 gas pressures which are needed to establish certain chemical potentials and thus concentrations of dissolved nitrogen in α-Fe[N] or γ-Fe[N] at a temperature of 650 °C (923 K) have been plotted in Figure 11. These pressures are (with reasonable effort) technically *un*feasible. Therefore, gas nitriding is usually performed with a gas mixture of NH_3 and H_2 at *atmospheric* pressure. Upon operating this process, NH_3 dissociates at the surface into H_2 gas and nitrogen dissolved in the solid substrate. The corresponding equilibrium can be described as:

$$NH_3 \rightleftharpoons [N] + \frac{3}{2}H_2 . \qquad \text{(Eq. 10)}$$

It is important to realize that establishment of this equilibrium requires that thermal dissociation of NH_3 can be ignored and that the recombination of nitrogen atoms adsorbed at the surface is negligible (if the latter would not hold, a stationary state, instead of an equilibrium situation, would occur at the surface of the substrate; for full discussion see Refs. [3, 45]).

The equilibrium concentration of dissolved nitrogen in the iron-based Fe[N] phase and the nature of this Fe[N] phase, (i.e. α-Fe[N], γ-Fe[N], γ´-Fe_4N_{1-y} or ε-Fe_3N_{1+x}) is determined by the temperature and the chemical potential of nitrogen which is directly proportional to the nitriding potential [5]

$$r_N = \frac{p(NH_3)}{p(H_2)^{3/2}} \qquad \text{(Eq. 11)}$$

where p is the partial pressure. Thus, the equilibrium nitrogen concentration in the specimen can be easily tuned by adjusting the composition of the nitriding gas atmosphere (see abscissa at the top of Figure 11 a, b).

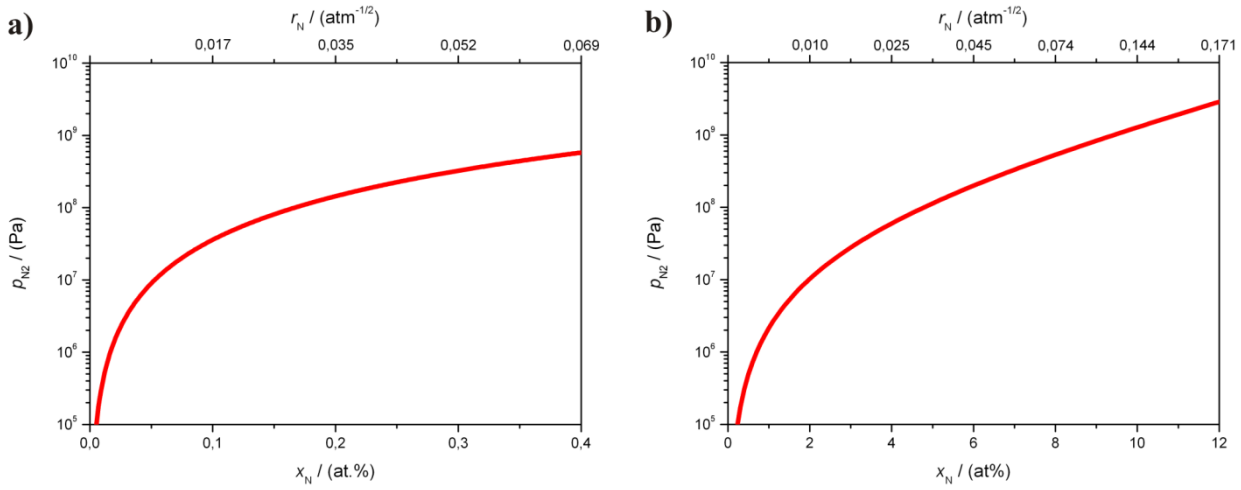

Figure 11: The pressure of nitrogen gas (p_{N2}) in equilibrium with the iron-nitrogen solid solution as a function of the nitrogen content, x_N, at 650 °C (923 K) for **a)** nitrogen ferrite (α-Fe[N]; $Fe + N_2 \rightleftharpoons \alpha$-Fe[N]) and **b)** nitrogen austenite (γ-Fe[N]; $Fe + N_2 \rightleftharpoons \gamma$-Fe[N]). Note the different nitrogen-concentration scales in the diagrams. The nitriding potentials (cf. Eq. (11)), corresponding to x_N, for nitriding in a NH_3/H_2 gas mixture at the same temperature and at 1 atm pressure ($NH_3 + Fe \rightleftharpoons \alpha$-Fe[N]$+ 3/2 H_2$; $NH_3 + Fe \rightleftharpoons \gamma$-Fe[N]$+ 3/2 H_2$), have been indicated on the abscissa at the top of both figures. The values for p_{N2} as a function of x_N were calculated using the Thermo-Calc software [46] adopting the thermodynamic model for nitrogen in iron presented in Ref. [47].

The Fe[N] phase which is not in *direct* contact with the nitriding gas atmosphere, i.e. the part of the substrate underneath the surface, is unstable with respect to its decomposition into nitrogen depleted $Fe[N]^*$ and N_2 gas. Thus, in the bulk of nitrogen ferrite and nitrogen austenite the following reactions (Eq. (12) and Eqs. (13 a, b), respectively) can occur under release of Gibbs energy

$$\alpha\text{-}Fe[N] \rightarrow \alpha\text{-}Fe[N]^* + N_2 \qquad \text{(Eq. 12)}$$

$$\gamma\text{-}Fe[N] \rightarrow \gamma\text{-}Fe[N]^* + N_2 \qquad \text{(Eq. 13a)}$$

$$\gamma\text{-}Fe[N] \rightarrow \alpha\text{-}Fe[N]^* + N_2 . \qquad \text{(Eq. 13b)}$$

The formation of N_2 gas can lead to pore development, provided diffusion to an outer surface, not exposed to the nitriding atmosphere, where escape of dissolved nitrogen as N_2 gas might occur, can be neglected. Upon this decomposition, the rise of the nitrogen gas pressure in the pores leads to plastic deformation of the surrounding matrix, as follows from the following consideration.

Adopting a spherical shape for a pore (= hollow sphere) yielding of the surrounding pore wall, taken of infinite thickness, occurs if

$$p_i \geq 2/3\sigma_y \qquad \text{(Eq. 14)}$$

where p_i is the gas pressure in the pore and σ_y represents the (uniaxial) tensile yield strength of the matrix. This limiting condition for yielding complies with both the *von Mises* criterion and the *Tresca* criterion [48].

Two sets of nitriding parameters were applied in the current work (see Table 3). The first set (650 °C, r_N=0.050 $atm^{-1/2}$) stabilizes nitrogen-ferrite, α-Fe[N], containing 0.35 at.% nitrogen [45] at the surface of the specimen, corresponding to an (hypothetical) equilibrium N_2 gas pressure of 440 MPa (see Figure 11a, calculated using Thermo-Calc [46] on the basis of a thermodynamic model for nitrogen in iron presented in Ref. [47]). This equilibrium pressure exceeds 2/3 of the

ferrite uniaxial tensile yield strength which equals about 50 MPa at 650 °C [49]. Hence, in view of the inequality (14), the ferrite matrix already yields well before the equilibrium N_2 gas pressure in a pore is reached.

The second set of nitriding parameters (650 °C, r_N=0.104 $atm^{-1/2}$) stabilizes nitrogen austenite, γ-Fe[N], containing 9.5 at.% nitrogen [47, 50][B] at the surface of the specimen, corresponding to an (hypothetical) equilibrium N_2 gas pressure of 1 GPa (see Figure 11b). Also in this case, the equilibrium N_2 gas pressure exceeds 2/3 of the austenite (uniaxial) tensile yield strength which equals about 570 MPa[C] [51, 52]. Hence, as for ferrite upon nitriding, in view of the inequality (14), the austenite matrix already yields well before the equilibrium N_2 gas pressure in a pore is reached.

[B] Instead of the nitriding potential, r_N, Thermo-Calc can only handle activities in order to define an equilibrium. To obtain the "activity" of nitrogen, a_N, in the gas phase, equal to the activity of nitrogen in the solid, the equilibrium constant of reaction (10) is needed (see Eq. (15) in Ref. [5]). This equilibrium constant was calculated using data taken from Ref. [47]. Knowledge of a_N, p and T then suffices to calculate the corresponding equilibrium concentrations of nitrogen in nitrogen austenite using Thermo-Calc adopting the thermodynamic description in Ref. [47] (the reference state of nitrogen for both phases is taken identical).

[C] The (uniaxial) tensile yield strength of austenite containing 9.5 at.% nitrogen was calculated applying the formula presented in Ref. [51] which is valid at a temperature of 295 K. For higher temperatures the tensile yield strength becomes significantly smaller and is above 450 °C nearly constant [52]. The relative decrease of the yield strength from RT to 450 °C is almost independent of the nitrogen content in austenitic steels [52]. Therefore, the calculated value for the tensile yield strength at 295 K was multiplied with this factor to estimate the tensile yield strength of austenite containing 9.5 at.% nitrogen at 923 K (650 °C).

Table 3: Nitriding parameters employed to stabilize either nitrogen ferrite, α-Fe[N], or nitrogen austenite, γ-Fe[N], at the surface of the specimen.

	temperature / (°C)	flow rate / (ml/min)		r_N / ($atm^{-1/2}$)	time / (h)
phase at specimen surface		NH_3	H_2		
α-Fe[N]	650	23.25	476.75	0.050	72
γ-Fe[N]	650	45.00	455.00	0.104	72

Starting with, respectively, nitrogen ferrite containing 0.35 at.% nitrogen and nitrogen austenite containing 9.5 at.% nitrogen (see above), the Gibbs energy differences for the decomposition reactions (12), (13a) and (13b) and the nitrogen concentrations left in the depleted matrix (Fe[N]*) were calculated, using approaches presented in Ref. [47], for the inner pore, nitrogen gas pressures at which the iron matrix starts to yield. The results have been gathered in Table 4.

In the cases of the decomposition of α-Fe[N] according to Eq. (12) and the decomposition of γ-Fe[N] according to Eq. (13a) further decomposition (i.e. after the onset of yielding) is thermodynamically favored as the corresponding Gibbs energy differences at the onset of yielding are negative (cf. Table 4).

The decomposition of γ-Fe[N] into α-Fe[N]* (Eq. (13b)) and N_2 gas in *closed* pores is only thermodynamically possible below nitrogen gas pressures (in the pores) of 330 MPa (then the Gibbs reaction energy is negative). Therefore, the decomposition of γ-Fe[N] into α-Fe[N]* can in principle occur but the release of Gibbs free energy for the decomposition of γ-Fe[N] into γ-Fe[N]* (Eq. (13a)) is larger at the considered conditions and thus is thermodynamically favored.

Table 4: The Gibbs reaction energies ΔG (if $\Delta G < 0$, energy is released), of reactions (12), (13a) and (13b) at 650 °C (923 K) are given for two nitriding potentials (r_N; the nitriding potential tunes at a given temperature the equilibrium nitrogen concentration in iron (c_N)), as applied in this work, and the pressure, p_i, where yielding of the matrix surrounding the pore is initiated ($p_i = 2/3\,\sigma_y$ [48], where p_i is the nitrogen-gas pressure in the pore and σ_y is the (uniaxial) tensile yield strength of ferrite [49] or nitrogen austenite [51, 52]). The nitrogen concentration, c^*_N, in the nitrogen-depleted iron of reactions (12), (13a) and (13b) is shown as well.

r_N / ($atm^{-1/2}$)	0.050	0.104	
p_i / (MPa)	33	380	
c_N (Fe[N]) / (at.%)	0.35	9.50	
c^*_N (Fe[N]*) / (at.%)	0.10	7.28	0.32
reaction	(12)	(13a)	(13b)
ΔG / (J/mol)	-17	-47	47

3.3. Experimental procedures

3.3.1. Specimen preparation

Several iron-based alloys were prepared from elemental granules of Fe (purity 99.98 wt%), Al (purity 99.999 wt%), Si (purity 99.999 wt%), Cr (purity 99.98 wt%), Co (purity 99.98 wt%), Ni (purity 99.98 wt%) and Ge (purity 99.999 wt%). The granules were melted in an induction furnace under a protective Ar atmosphere and cast to rods with a length of 100 mm and a diameter of 10 mm. The cast rods were ground to remove surface oxides and cleaned in ethanol in an ultrasonic bath and thereafter cold-rolled to sheets of approximately 1 mm thickness. Rectangular specimens (15 × 10 × 1) mm were cut from such cold rolled sheets. These specimens

were ground and polished (final stage with 1 µm diamond paste) from both sides and ultrasonically cleaned in ethanol. The specimens were then encapsulated in a quartz tube under protective Ar atmosphere and recrystallized at 800 °C for 20 min. After the recrystallization treatment, the specimens were polished (again) with 1 µm diamond paste to remove surface oxides, which might have formed during the recrystallization treatment, and ultrasonically cleaned in ethanol.

In order to determine the amounts of alloying elements in samples taken from the produced casts, inductively coupled plasma optical emission spectroscopy (ICP-OES) was applied, whereas carrier gas hot extraction was used to determine the amount of light element impurities such as O and N. The amounts of C and S were determined by means of the combustion method. Results of the chemical analysis for Fe and the iron-based alloy casts are shown in Table 5.

Table 5: Alloying element and light element impurity contents in the pure iron and the binary iron-based Fe-*Me* alloy casts used in the present work.

alloy	alloying element (wt.%)	alloying element (at.%)	O (µg/g)	N (µg/g)	C (µg/g)	S (µg/g)
Fe	-	-	70	< 10	< 10	< 10
Fe-Al	0.95 ± 0.01	1.95 ± 0.02	20	< 5	< 10	< 10
Fe-Si	1.01 ± 0.01	1.99 ± 0.02	30	< 20	< 10	< 20
Fe-Cr	1.90 ± 0.02	2.08 ± 0.02	24	< 10	< 20	< 20
Fe-Co	2.13 ± 0.02	2.02 ± 0.02	20	< 10	< 20	< 20
Fe-Ni	2.12 ± 0.02	2.02 ± 0.02	35	< 10	< 20	< 20
Fe-Ge	2.17 ± 0.02	1.76 ± 0.02	50	< 10	< 35	< 20

3.3.2. Nitriding

The gas nitriding facility consists of a vertical multizone quartz-tube furnace (diameter 28 mm) and is equipped with temperature controllers (temperature variation ± 1°C) and gas mass-flow controllers. For the nitriding treatments, the sheet specimens (see above) were suspended with a quartz fiber and positioned in the uniform temperature zone of the furnace. The sum of the gas fluxes of NH_3 (purity 99.998 vol%) and H_2 (purity 99.999 vol%) were kept constant at 500 ml/min and the NH_3 and H_2 gas fluxes were maintained such to set the required nitriding potential [5]. Nitriding experiments were carried out such that either nitrogen ferrite or nitrogen austenite was stabilized at the specimen`s surface. The corresponding two sets of nitriding conditions employed in the present work are shown in Table 3. The nitriding treatment was interrupted by quenching the specimens into water which was purged with N_2 gas to minimize the amount of dissolved oxygen.

3.3.3. Weight measurement

Specimens were weighed before nitriding and after homogenous (through) nitriding and the weight uptake was used to calculate the nitrogen uptake of the specimens. Five weight measurements were carried out and from the mean, the average nitrogen content and its standard deviation were calculated. For weighing, a comparator balance (Mettler XP56) with 1 µg (0.001 mg) sensitivity was used.

3.3.4. X-ray diffraction

A PANalytic X´Pert MPD (multi-purpose diffractometer) was used to characterize the phases developed after nitriding. Co-K_α radiation and Bragg-Brentano geometry with a graphite

monochromator in the diffracted beam and a PANalytical X´Celerator detector were employed. The specimens were rotated around their surface normal during the measurements to enhance crystal statistics. The recorded XRD-patterns were analyzed by using the software X´Pert HighScore and the different phases were identified using the data-base from the International Center for Diffraction Data (ICDD) [12].

3.3.5. Light microscopy

Specimens for light microscopical analysis were cut perpendicular to the nitrided surface and embedded in Struers Polyfast to obtain cross-sections. The embedded cross-sections were ground, polished (final stage 1 µm diamond paste) and etched with 2 vol.% Nital for 30 s. A Zeiss Axiophot microscope, equipped with an Olympus Color View IIIu digital camera, was used to record the microstructures. In order to determine the void fraction in the nitrided region, 10 images were recorded from different, randomly selected regions of the nitrided volume (each image covers a rectangular area of (440 × 100) µm) and the area fraction of the pores was determined by using the software analySIS 5.0 from Soft Imaging System. The area fraction of the pores is equal to the volume fraction of the pores if the pores do not exhibit a morphological texture [53].

3.3.6. Scanning electron microscopy (SEM) and electron backscatter diffraction (EBSD)

A Leo 1530 VP (acceleration voltage 3 kV, working distance 6 mm) equipped with an in-lens detector (30 mm aperture) was applied to record SEM micrographs. EBSD investigation was carried out to determine the distribution, shape, and crystal orientation of the phases present in a specimen´s cross-section. To this end, a Zeiss LEO 438 VP scanning electron microscope

(acceleration voltage 20 kV) equipped with a high-speed camera from EDAX and the analyzing software OIM 5.31 from TSL was employed.

3.3.7. Electron probe microanalysis (EPMA)

In order to determine local chemical compositions, point scans were performed using the SX100 microanalyzer from Cameca. Cross-sections for analysis were prepared in a similar way as for light microscopy except that the final etching step was omitted. A focused electron beam of acceleration voltage of 15 kV and current of 100 nA was employed. The intensities of generated characteristic N-K_α, and Fe-K_β X-ray emission peaks were used to obtain the element concentrations of N and Fe, respectively: The measured N-K_α, and Fe-K_β intensities were divided by the intensities recorded from γ'-Fe_4N (N-K_α) and Fe (Fe-K_β) standard specimens, respectively, and the concentration values were calculated from these intensity ratios applying the $\phi(\rho z)$-approach according to Ref. [54].

3.4. Results

3.4.1. Pore formation in nitrogen ferrite and the role of alloying elements

Microstructures of the nitrided regions as developed in pure iron and the binary iron-based Fe-*Me* alloys nitrided for 72 h under conditions which, at least for pure iron (see what follows), stabilize the ferrite phase at the surface of the specimen (650 °C, r_N = 0.050 $atm^{-1/2}$; cf. Ref. [6]) are shown in Figure 12. The amount of nitrogen taken up by the specimens upon nitriding (cf. Section 3.3.3) and the resulting pore fractions (cf. Section 3.3.5) have been gathered in Table 6.

Table 6: Pore fraction and nitrogen content resulting by nitriding under nitrogen-ferrite stabilizing condition (650 °C using r_N = 0.050 atm$^{-1/2}$) for pure iron and several iron-based Fe-*Me* alloys, all (through) nitrided for 72 h. Additionally, the stoichiometry of the possibly precipitating alloying-element nitrides, their standard Gibbs energy of formation, ΔG_f^0 (at 298 K, for the reaction of one mole of N_2), and their volume misfit with the ferrite matrix have been indicated.

alloy	Fe	Fe-Al	Fe-Cr	Fe-Co	Fe-Ge	Fe-Si	Fe-Ni
pore fraction / (%)	0.55	< 0.1	0.51	0.52	2.13	< 0.1	4.20
N content / (at.%)	0.31	2.39	2.18	0.26	0.23	0.24	0.99
Me_xN_y	-	AlN	CrN	Co_3N	β-Ge_3N_4	β-Si_3N_4	Ni_3N
ΔG_f^0 (Me_xN_y) / (kJ/mol)	-	-574	-185	~ 0	-153	-358	~ 0
volume misfit[D] / (%)	-	77	52	13	143	105	13

The micrographs reveal the development of porosity along grain boundaries of the ferrite matrix. The amount of porosity in the alloys shows a strong dependence on the presence and the type of alloying element: Fe-Ni and Fe-Ge alloys show the highest porosity; pure iron and Fe-Cr and Fe-Co alloys take an intermediate position and the lowest porosity can be detected in Fe-Al and Fe-Si alloys (see Table 6 and Figure 12).

D

$$\frac{\left(\frac{M_{Me_xN_y}}{x\cdot\rho_{Me_xN_y}}-\frac{at.wt_{Fe}}{\rho_{Fe}}\right)}{\frac{at.wt_{Fe}}{\rho_{Fe}}}\cdot 100$$

where M, ρ and *at.wt* are molecular mass, density and atomic mass, respectively.

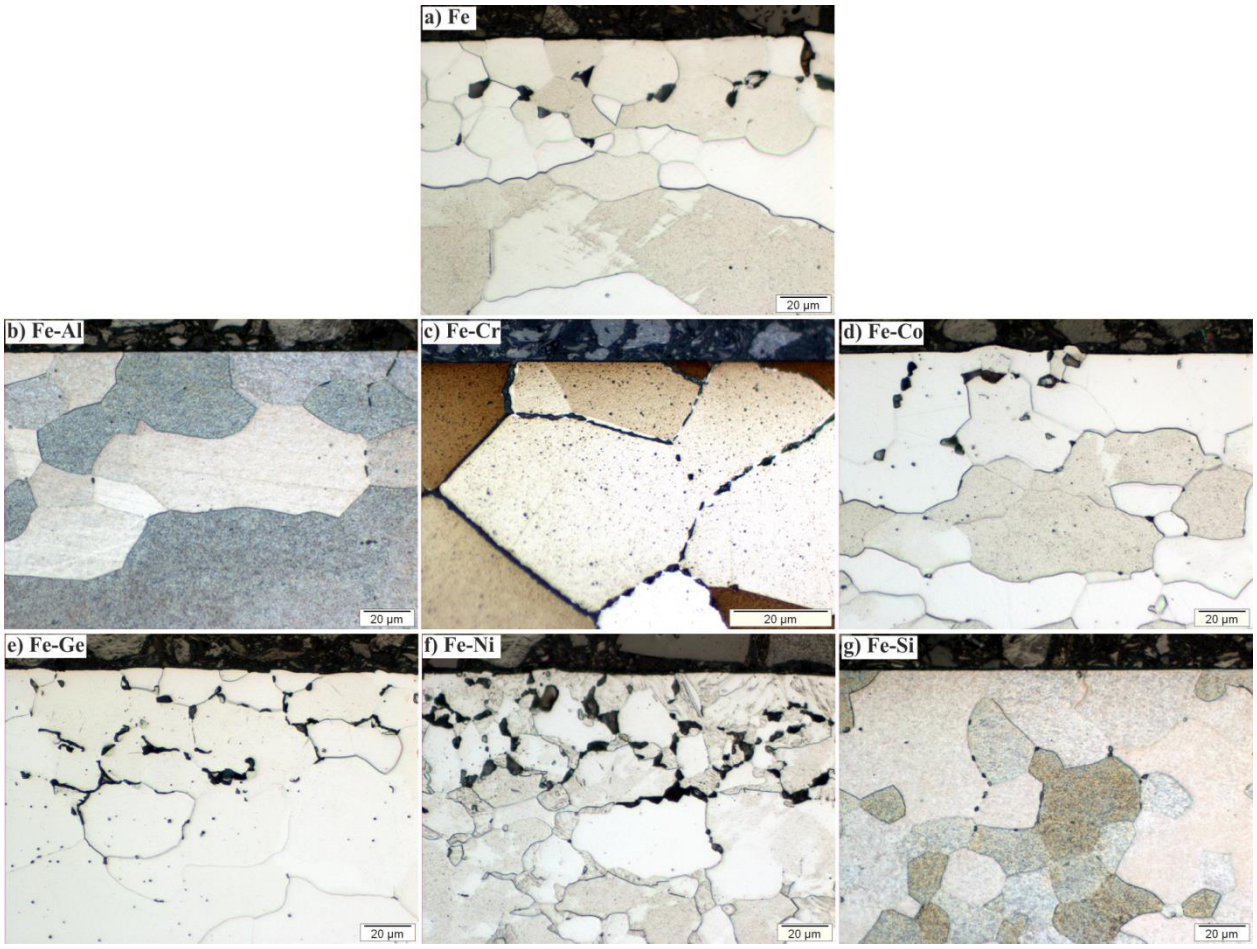

Figure 12: Microstructures for nitrogen-ferrite stabilizing conditions. Light optical micrographs (LOM) recorded from cross-sections (polished and etched) of iron and iron-based Fe-Me alloy specimens after nitriding for 72 h at 650 °C and with r_N = 0.050 atm$^{-1/2}$. The amount of pores is small in the Fe-Al and Fe-Si alloys, moderate in pure Fe and the Fe-Cr and Fe-Co alloys, and large in the Fe-Ni and Fe-Ge alloys. Note that the Fe-Ni alloy became austenitic in the surface region upon nitriding (see text).

The X-ray diffractograms recorded from the surface of the iron and iron-based Fe-*Me* alloy specimens after the nitriding treatment are shown in Figure 13. Except for the Fe-Ni alloy, the diffractograms of the nitrided specimens show only ferrite reflections. In case of the Fe-Ni alloy,

in addition to ferrite reflections, reflections belonging to nitrogen austenite and nitrogen martensite were detected.

The microstructures as developed close to the surface of polycrystalline pure iron and polycrystalline binary Fe-Co and Fe-Ge alloy specimens are shown in Figure 14. It is observed that the development of pores (along ferrite-grain boundaries) in the polycrystalline iron and polycrystalline Fe-*Me* alloys is associated with bulging out of the ferrite matrix on top of the pores.

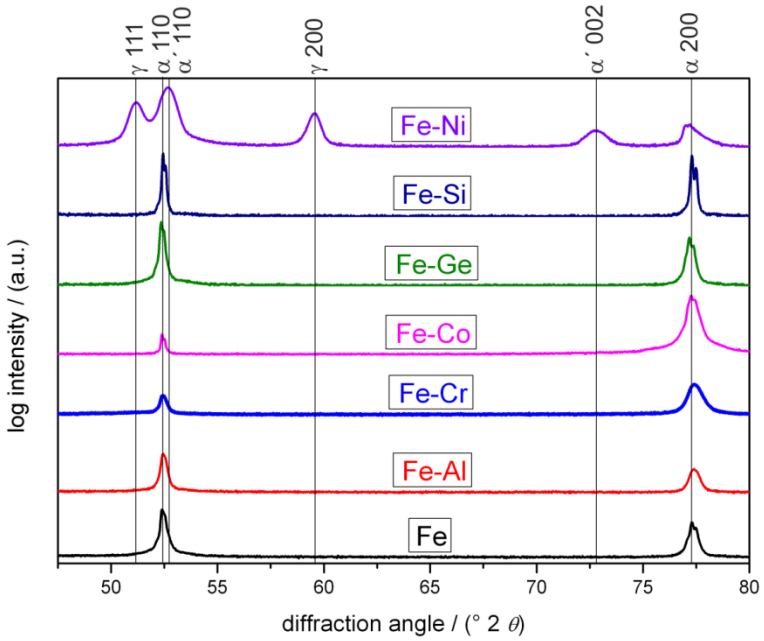

Figure 13: X-ray diffractograms (Co-K_α) recorded from the surface of pure iron and iron-based Fe-*Me* alloy specimens after nitriding for 72 h at 650 °C and with r_N = 0.050 $atm^{-1/2}$. Except in case of the Fe-Ni alloy, only reflections from ferrite are observed. The diffractogram of the nitrided Fe-Ni alloy shows, in addition to ferrite (α) reflections, reflections belonging to nitrogen austenite (γ) and nitrogen martensite (α´).

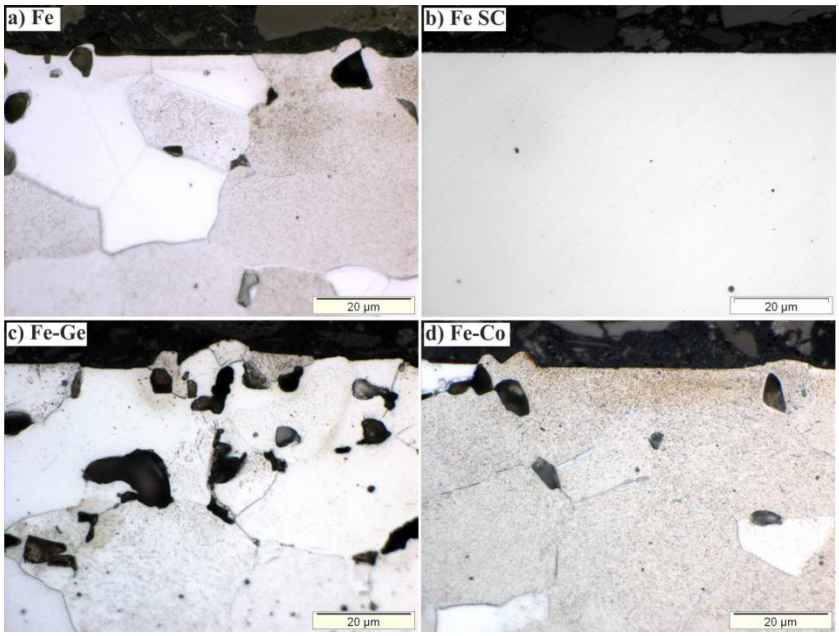

Figure 14: Light optical micrographs recorded from cross-sections of iron and iron-based, ferritic specimens after nitriding for 72 h at 650 °C with r_N = 0.050 atm$^{-1/2}$. **a)** Polycrystalline iron **b)** Single crystal of iron nitrided for 168 h (72 h + 96 h) applying the conditions as above, which shows no pore formation (cross-section was only polished). **c)** Fe-Ge alloy and **d)** Fe-Co alloy. Pores which developed close to the surface in polycrystalline iron and Fe-Ge and Fe-Co alloys caused bulging out of material at locations of the surface close to these pores.

In contrast with the polycrystalline specimens, a single crystalline iron specimen shows no porosity at all – even, as revealed by additional experiments, after a nitriding time much longer than that for the polycrystalline specimens (Figure 14b).

3.4.2 Pore formation in nitrogen austenite and the role of alloying elements

Microstructures of the nitrided regions developed in the, initially ferritic, pure iron and binary iron-based Fe-*Me* alloy specimens, nitrided for 72 h under conditions which stabilize the nitrogen

austenite phase at the surface of the specimens (650 °C, r_N = 0.104 $atm^{-1/2}$; cf. Ref. [6]), are shown in Figure 15 and Figure 16. The amount of nitrogen taken up by the specimens upon nitriding (cf. Section 3.3.3) and the resulting pore fractions (cf. Section 3.3.5) have been gathered in Table 7.

The nitrided polycrystalline iron specimen shows isolated pores as well as channels of coalesced pores along grain boundaries which are more or less perpendicular to the surface (Figure 15a). Some of these channels are in direct contact with the outer surface. The microstructure in the surface adjacent region, as exposed by the EBSD-phase map (Figure 15b and 15c), consists of a relatively thin surface adjacent zone dominantly composed of nitrogen austenite (γ-Fe[N]; indicated by green color). A zone of dominantly nitrogen martensite (α´; indicated by dark red color) occurs at larger depth, followed by a core of nitrogen ferrite (α-Fe[N]; indicated by bright red color). The presence of nitrogen austenite at the very surface is confirmed by XRD-phase analysis (see the diffractogram at the bottom of Figure 17).

Pores which have developed in this region are surrounded by nitrogen austenite and nitrogen martensite as indicated by EBSD (see Figure 15c). Local nitrogen concentrations, as determined by EPMA (point) measurements (see concentration indications in Figure 15c), confirm the presence of nitrogen austenite/martensite adjacent to the pores: the nitrogen concentrations are much too high for nitrogen ferrite. Beneath the region exhibiting channels, a needle-like microstructure (see Figure 15a) consisting nearly exclusively of nitrogen martensite (see Figure 15b) has formed from nitrogen austenite upon water quenching, applied after completion of the nitriding time (see Section 3.3.2).

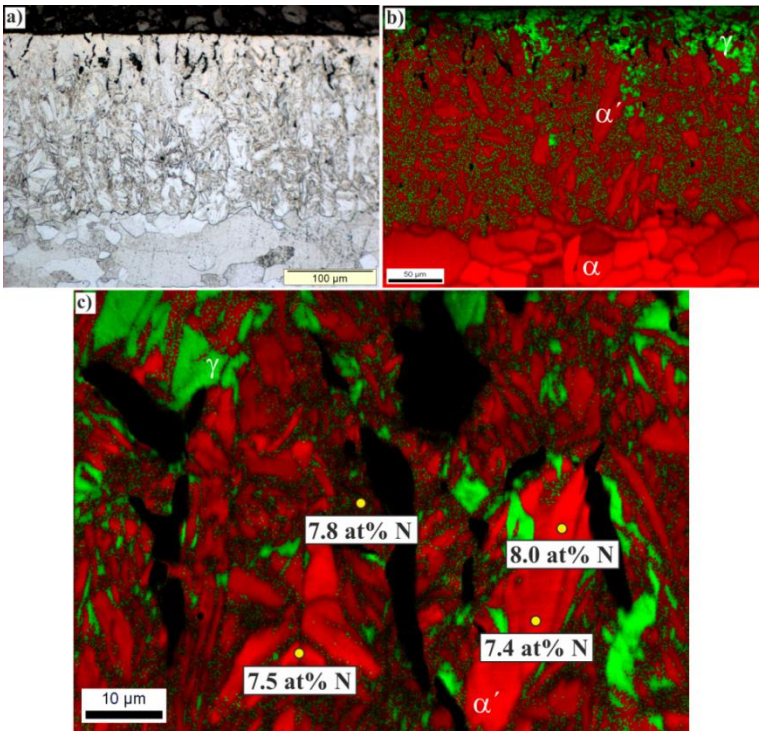

Figure 15: **a)** Light optical micrographs recorded from the cross-section (polished and etched) of a polycrystalline iron specimen nitrided at 650 °C for 72 h with r_N = 0.104 atm$^{-1/2}$. Channels of coalesced pores, oriented more or less perpendicular to the surface, can be observed. **b)** EBSD-phase map (overlay of image-quality (IQ) map and phase map; high IQ: bright red and bright green; low IQ: dark red and dark green. In this way one can distinguish between nitrogen ferrite (α; bright red in (b)) and (strained) nitrogen martensite (α´; dark red in (b)). The surface region consists predominantly of fcc nitrogen austenite (γ, green) succeeded at increasing depth below the surface by b.c.t. nitrogen martensite (α´, dark red) and at still larger depths, by bcc. ferrite (α, bright red). **c)** EBSD-phase map (overlay of IQ map and phase map) at higher magnification than in b) recorded from the surface adjacent region. The local nitrogen concentrations in the matrix surrounding the pores, as determined by EPMA, have been indicated in the figure. It follows that both fcc nitrogen austenite and b.c.t. nitrogen martensite surround the pores (black regions).

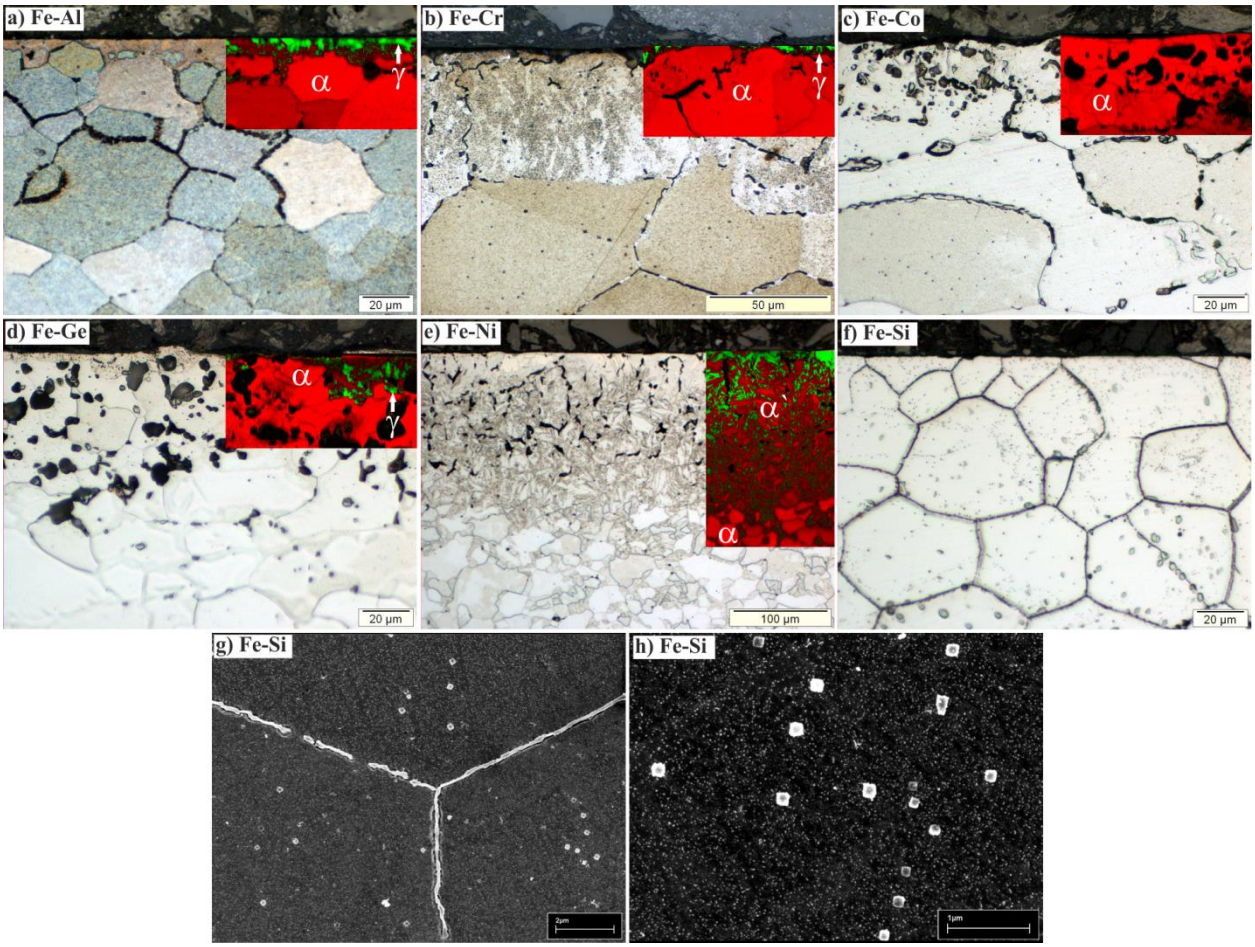

Figure 16: Microstructures for nitrogen austenite stabilizing conditions. Micrographs are recorded from cross-sections (polished and etched) of iron-based Fe-*Me* alloy specimens after nitriding for 72 h at 650 °C and with r_N = 0.104 $atm^{-1/2}$. **a–f)** Light optical micrographs with inserted EBSD-phase maps (overlay of IQ map and phase map; cf. caption of **Figure** 15) where α (bright red), α´ (dark red) and γ (green) denotes nitrogen ferrite, nitrogen martensite and nitrogen austenite, respectively. **g, h)** SEM micrographs recorded from the nitrided Fe-Si alloy, which remained ferritic upon nitriding. The amount of pores is small in the Fe-Al and Fe-Cr alloys, moderate in the Fe-Ni alloy, and large in the Fe-Co and Fe-Ge alloys. No pore formation is observable in case of the Fe-Si alloy; Si_3N_4 bands occur along ferrite grain boundaries and cubical Si_3N_4 precipitates are present within ferrite grains (see text).

Table 7: Pore fraction and nitrogen content resulting by nitriding under nitrogen-austenite stabilizing condition (650 °C using r_N = 0.104 $atm^{-1/2}$) for pure iron and several iron-based Fe-*Me* alloys, all nitrided for 72 h. Additionally, the stoichiometry of the possibly precipitating alloying-element nitrides and their standard Gibbs energy of formation, ΔG_f° (at 298 K for the reaction of one mole of N_2), and their volume misfit with the austenite matrix have been indicated.

alloy	Fe	Fe-Al	Fe-Cr	Fe-Co	Fe-Ge	Fe-Si	Fe-Ni
pore fraction / (%)	4.79	0.97	2.30	13.90	17.03	-	8.68
N content / (at%)	3.67	2.62	3.33	0.35	0.57	0.83	2.74
Me_xN_y	-	AlN	CrN	Co_3N	β-Ge_3N_4	β-Si_3N_4	Ni_3N
ΔG_f^0 (Me_xN_y) / (kJ/mol)	-	-574	-185	~ 0	-153	-358	~ 0
volume misfit / (%)	-	-8	-21	-42	26	6	-42

Except the Fe-Si alloy, all nitrided (initially ferritic) Fe-*Me* alloys showed distinct porosity development (Figure 16) and a layer consisting of nitrogen austenite and nitrogen martensite (cf. insets in Figure 16 and diffractograms in Figure 17). The largest amount of porosity has been generated in the nitrided Fe-Ge alloy (see also Table 7). In this alloy pores have developed which often exhibit a more globular shape and have diameters of several micrometers (cf. Figure 16d). The nitrided Fe-Si alloy does not show pore development and, also in contrast with the other nitrided Fe-*Me* alloys and nitrided iron under these conditions, its surface adjacent region consists of nitrogen ferrite and not of nitrogen austenite (cf. X-ray diffractograms in Figure 17), instead the Fe-Si alloy showed development of bands (of Si_3N_4; see Section 3.5.2) along ferrite grain boundaries and cubical (Si_3N_4; see section 3.5.2) particles within ferrite grains (Figure 16 g, h)

The thickness of the nitrogen austenite/martensite surface layer after nitriding is different in the various Fe-*Me* alloys. The thickness of the nitrogen austenite/martensite-surface layer is very

thin in case of Fe-Al, Fe-Cr, Fe-Co, and Fe-Ge alloys, whereas a thick austenite/martensite-surface layer occurs in case of the Fe-Ni alloy and pure iron.

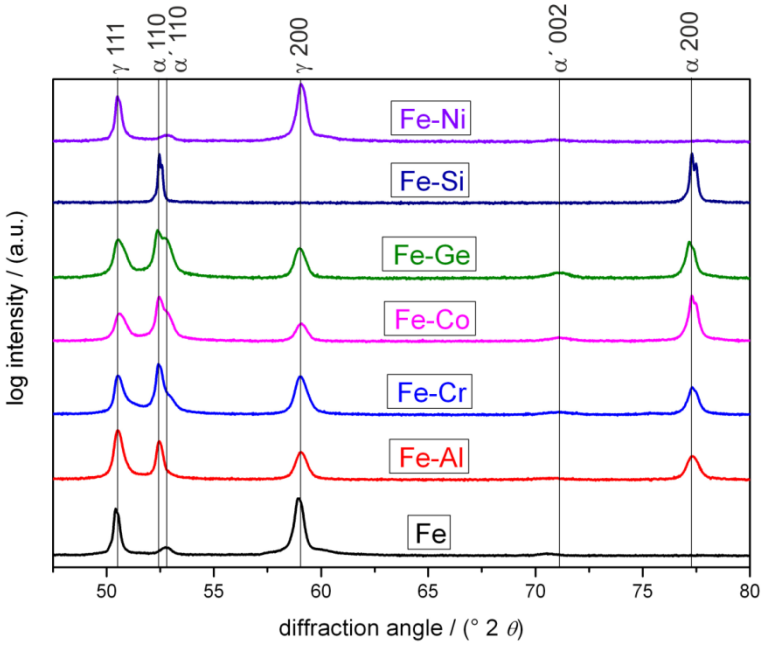

Figure 17: X-ray diffractograms (Co-K_α) recorded from the surface polycrystalline pure Fe specimen and iron-based Fe-*Me* alloys after nitriding for 72 h at 650 °C and with r_N = 0.104 $atm^{-1/2}$. The diffractograms of all nitrided Fe-*Me* alloys show reflections from nitrogen austenite (γ) and nitrogen martensite (α´), with the exception of the diffractogram of the Fe-Si alloy, which shows only ferrite reflections.

3.5. Discussion

3.5.1. Pore formation in nitrogen ferrite and the role of alloying elements

The applied nitriding time of 72 h at 650°C with r_N = 0.050 $atm^{-1/2}$ is sufficient to homogeneously (through) nitride the ferritic matrix of the 1.0 mm thick specimens (cf. data for the diffusion coefficient of nitrogen in ferrite as given in Ref. [7]); the homogeneity of the

nitrided ferrite matrix was confirmed by the observed constant hardness level over the complete thickness of the 1.0 mm thick specimens as measured on cross-sections.

The ferrite matrix of the nitrided pure α-Fe and nitrided Fe-*Me* alloys, with interstitially dissolved nitrogen, is thermodynamically unstable underneath the surface with respect to decomposition into nitrogen-depleted ferrite and molecular N_2 gas (cf. reaction (12) in Section 3.2 and Figure 18). Evidently, pores filled with N_2 gas start to develop at grain boundaries (Figure 12). Upon prolonged nitriding these pores coalesce, leading to the appearance of channels i.e. open grain boundaries (e.g. see Figure 12c and 12e). From a comparison of nitrided single crystalline and polycrystalline iron specimens (cf. Figure 14) it follows that the grain boundaries are essential agents for the nucleation and growth of pores in nitrided ferrite; no pore formation within ferrite grains occurs. Indeed, the driving force for the decomposition of α-Fe[N] is relatively small (see Figure 18), so that homogenous nucleation of N_2 gas filled pores within the grains may be obstructed. This contrasts with the development of pores in ε-iron nitride.

The nitrogen uptake recorded for the nitrided, polycrystalline pure iron specimen amounts to 0.31 at.% (cf. Table 6) and thus is slightly smaller than the equilibrium value of the nitrogen solubility of iron as predicted for the employed nitriding conditions (0.35 at.% according to Ref. [45]). This difference can be explained by the formation of pores (possibly coalesced to channels) in contact with the outer atmosphere (cf. Figure 12a and 14a) and the thus occurring nitrogen depletion of the ferrite matrix surrounding these pores/channels (cf. Eq. (12)). Nitrogen uptakes well above the maximum nitrogen solubility of ferritic pure iron occur in case of the Fe-Cr and Fe-Al alloys, which can be attributed to the development of AlN and CrN precipitates, respectively, in the ferrite matrix.

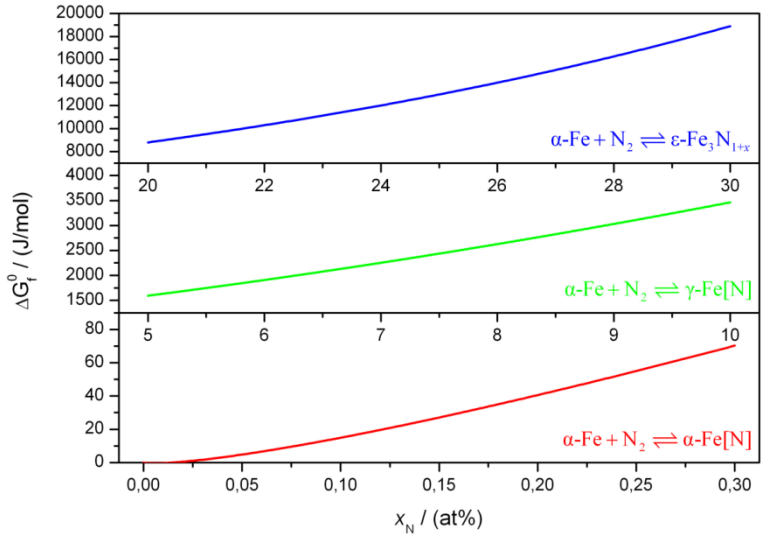

Figure 18: The Gibbs energies of formation, ΔG_f^0 (at 298 K and 1 atm), from one mole ferrite, $\alpha\text{-Fe}$, and the corresponding amount of nitrogen gas, as a function of the nitrogen content, x_N, in the nitrogen ferrite (α-Fe), nitrogen austenite (γ-Fe) and the ε-Fe_3N_{1+x}. Clearly ΔG_f^0 is positive for all three reactions and increases significantly with the nitrogen content in the product phases concerned. Evidently, the three phases considered are all unstable with respect to decomposition. The driving force for this decomposition increases in the order α-Fe → γ-Fe → ε-Fe_3N_{1+x}, irrespective of the nitrogen content in the range of possible nitrogen content for each phase. For all phases the driving force for decomposition increases with increasing nitrogen content. Values for ΔG_f^0 were calculated using the Thermo-Calc software [46] adopting the thermodynamic model for nitrogen in iron presented in Ref. [47].

Pore formation in nitrided Fe-Al and Fe-Cr alloys can be discussed as follows: (i) The (metastable) equilibrium amount of dissolved nitrogen in the ferrite matrix of nitrided iron-based Fe-Al and Fe-Cr alloys can in principle be larger than that for nitrided pure iron, due to (a) a higher nitrogen solubility in iron-based Fe-Al [55] and Fe-Cr alloys [56] as compared to pure iron

and (b) the presence of so-called excess nitrogen taken up in the strain fields surrounding the *Me*N-precipitates [14, 57, 58]. (ii) Moreover, the development of AlN[E] and CrN precipitates in Fe-Al and Fe-Cr alloys upon nitriding competes with the development of N_2 gas containing pores. Hence, it is concluded from (i) and (ii) that the pore fractions in nitrided Fe-Al and Fe-Cr alloys can be smaller than in nitrided pure iron, as observed (cf. Table 6). Note that the presence of dissolved excess nitrogen in nitrided Fe-Al and Fe-Cr alloys after the nitriding only seemingly suggests a higher driving force for pore development than in pure iron: this excess nitrogen is thermodynamically stabilized by the misfit-strain fields surrounding the *Me*-nitride precipitates [14]. However, if upon continued nitriding, a coherent → incoherent transition sets in for the initially precipitated *Me*-nitrides in the surface adjacent region, then the nitride/matrix misfit is no longer (fully) accommodated elastically and the capacity for dissolving excess nitrogen gets lost. The originally dissolved excess nitrogen then tends to precipitate and N_2 gas filled pores can develop at grain boundaries. This effect has been observed in Ref. [59].

Pore formation in nitrided Fe-Co and Fe-Ge alloys can be discussed as follows. The Fe-Co and Fe-Ge alloys show a nitrogen uptake much smaller than that of the Fe-Al and Fe-Cr alloys (cf. Table 6) and even smaller than that of pure iron. (i) Co [60] and Ge[F] dissolved in α-Fe lower

[E] Nitriding of iron-based Fe-Al alloy at a lower temperature (550 °C) than that in the current study (650 °C) leads, prior to the precipitation of hexagonal AlN, to the formation of pores along ferrite-grain boundaries due to the large nitrogen supersaturation of the ferrite matrix and the difficult and thus slow precipitation of hexagonal AlN. In a later stage the coalesced pores ("microcracks") are closed due to the planar state of high compressive stresses, parallel to the surface, induced by precipitated AlN [44]. The pores which are present in the current Fe-Al alloy have developed after AlN precipitation

[F] In the absence of literature data, the relatively low nitrogen solubility of ferritic Fe-Ge alloy was demonstrated by the following additional experiments performed in this project: Foils from pure iron and Fe-Ge alloy were prepared with a thickness of 0.2 mm and the lateral dimensions of (15 x 10) mm. Specimens, cut from these foils, were

the nitrogen solubility of the ferrite. Extremely high nitriding potentials are necessary to form Co and Ge nitrides: see Ref. [61] for a Lehrer-type diagram for the Co-N system and note the extremely large volume misfit of Ge_3N_4 with the ferrite matrix, as given in Table 6. (ii) In nitrided Fe-Co and Fe-Ge alloys the formation of N_2 gas filled pores can occur in the absence of competition with *Me*-nitride precipitation. Hence, it is concluded from (i) and (ii) that pore fractions in nitrided Fe-Co and Fe-Ge alloys can be (much) higher than in nitrided pure iron, as observed

(cf. Table 6).

Si as an alloying element in iron lowers, similar as Co and Ge, the equilibrium nitrogen solubility in ferrite [62]. Although, as compared with the Fe-Ge system (where no *Me*-nitride development was observed at all upon nitriding), for the Fe-Si system the chemical driving force for *Me*-nitride precipitation is larger and the nitride/matrix misfit is smaller (but still very large; see Table 7), yet, but only after very long nitriding times, (*amorphous* instead of crystalline) silicon-nitride precipitates develop in the ferrite-matrix grains (see Refs.[16-18] and Figure 16g). On this basis, and with reference to the above discussion on nitrided Fe-Co and Fe-Ge alloys, one might expect a pore fraction of value as observed for Fe-Co and Fe-Ge alloys. Instead, a pore fraction is observed that is even distinctively smaller than that for pure iron. Recognizing that in ferritic pure iron and ferritic Fe-*Me* alloys the grain boundaries act as the only nucleation agents for the N_2 gas filled pores (see Figure 12, section 3.4.1 and above), this peculiar phenomenon is

recrystallized at 800 °C for 20 min and subjected to nitriding at 580 °C with r_N = 0.104 $atm^{-1/2}$ for 15 h. This lower nitriding temperature (as compared to 650 °C) was chosen to retard pore formation and the chosen time was found to be sufficient to homogenously (through) nitride these 0.2 mm thick foils and to avoid pore formation. The nitrogen equilibrium concentration after nitriding was determined for the pure iron to be 0.30 at.% and for the Fe-Ge alloy to be only 0.19 at.%.

interpreted as follows. Si_3N_4 precipitates as amorphous bands along the ferrite-matrix grain boundaries, prior to precipitation of (cubical) Si_3N_4 particles within the ferrite-matrix grains [17]. It is suggested that these amorphous bands hinder the nucleation of pores at grain boundaries, which are the agents for nucleation of N_2 gas filled pores in ferritic material, as discussed above, (also) because by formation of these bands the nitrogen otherwise available for pore formation is consumed.

The relatively high amount of nitrogen taken up by the Fe-Ni alloy specimen (0.99 at.%) is due to the development of nitrogen austenite (so the specimen did not remain ferritic as the other alloys nitrided subject to the same conditions; cf. Figure 13); it cannot be ascribed to the development of nickel nitride: extremely high nitriding potentials, which are not applied in this work, are required to stabilize nickel nitrides [63]. Upon water quenching to room temperature, nitrogen austenite transforms to nitrogen martensite provided its nitrogen content is not too high (martensite start temperature, M_s, of pure Fe[N] is above RT for a nitrogen content larger than 8.4 at.% [64]). The austenite stabilization observed upon nitriding for the originally ferritic Fe-Ni alloy in the surface adjacent region is the result of the combined austenite stabilization effects of both dissolved nitrogen and dissolved Ni (evidently, only the 2 at.% Ni in the considered Fe-Ni alloy cannot stabilize the austenite phase at the nitriding temperature of 650 °C, according to the data presented in Ref. [65]).

The high N_2 gas pressures which would develop in the closed pores cannot be sustained by surrounding matrix (cf. Section 3.2). Thus, pore formation is associated with plastic yielding of the surrounding ferrite matrix: the diameters of the pores at the grain boundaries in the polycrystalline specimens are several microns and it appears that, under the action of the N_2 gas pressure in closed pores in the subsurface region, the specimen surface can (even) bulge out (Figure 14a, c, d) by plastic yielding of the ferrite matrix surrounding the pores.

Precipitation of alloying-element nitrides significantly strengthens the ferrite matrix which, in view of the discussion in the above paragraph, can then retard pore growth. Hence, not only pore nucleation is less abundant in the case of alloying elements which easily precipitate as nitrides (due to a smaller chemical driving force for pore formation in the beginning of nitriding; see above discussion), but also the subsequent pore growth is retarded.

3.5.2. Pore formation in nitrogen austenite and the role of alloying elements

The microstructure developing upon nitriding an (initially ferritic) pure iron specimen, employing conditions which stabilize nitrogen austenite, γ-Fe[N], at the specimen surface (650 °C, r_N = 0.104 $atm^{-1/2}$), can be understood as follows (see Figure 15). Nucleation of nitrogen austenite can occur at the moment that the nitrogen concentration in ferrite at the surface exceeds that of the ferrite/austenite-phase boundary in the Fe-N phase diagram. Continued nitriding leads to a thickness increase of this formed nitrogen-austenite layer by migration of the α/γ-transformation front in the direction of the specimen´s core. The here applied nitriding time of 72 h at 650 °C is not sufficient for the complete transformation of the 1.0 mm thick specimen into nitrogen austenite and thus the specimens were not homogenously (through) nitrided (the core region of the specimens remained ferritic; the core region is saturated with nitrogen; a hardness measurements in the core region revealed a hardness (200 $HV_{0.1}$) which is twice that of unnitrided pure ferrite), in contrast with the nitrided ferritic specimens discussed in Section 3.5.1.

Similar as discussed for nitrogen ferrite (Section 3.5.1), the nitrogen austenite underneath the surface is thermodynamically unstable with respect to decomposition into nitrogen depleted austenite and molecular N_2 gas (cf. reaction (13a) in Section 3.2 and Figure 18). As a consequence, porosity develops along the grain boundaries of austenite in the subsurface regions. Prolonged nitriding leads to the coalescence of pores to channels which can be in direct contact

with the nitriding outer atmosphere (NH_3/H_2-gas mixture). (Subsequent) Decrease of the nitrogen concentration in nitrogen austenite adjacent to the pores can eventually lead to the reemergence of ferrite, as reported in an earlier investigation [41].

In the current work, pores which have developed upon nitriding at austenite-grain boundaries are, according to the EBSD- and EPMA measurements (see Figure 15c), surrounded by nitrogen austenite (and/or nitrogen martensite after quenching). The nitrogen concentrations in the vicinity of pores (see Figure 15c) are too high for the presence (by reemergence as discussed above or by direct decomposition according to reaction (13b)) of a possible ferrite phase (the maximum solubility of nitrogen in ferrite at 650 °C amounts to approx. 0.27 at.% [47]). As shown in Section 3.2, the value of the Gibbs reaction energy of the decomposition reaction (13a) of nitrogen austenite into nitrogen-depleted nitrogen austenite and N_2 gas is negative, whereas the decomposition reaction (13b) of nitrogen austenite into nitrogen-depleted ferrite and N_2 gas is only thermodynamically possible until an inner pore N_2 gas pressure of 330 MPa has been attained. Therefore, the occurrence of nitrogen ferrite, as a direct decomposition product of nitrogen austenite, is at the N_2 gas pressures in the pores where yielding of the surrounding matrix occurs (380 MPa; cf. Section 3.2) inhibited.

The EBSD-phase map (Figure 15b) shows nitrogen austenite concentrated close to the surface of the nitrided and quenched iron specimen. The martensite-start temperature (M_s) depends on the nitrogen concentration (the higher the nitrogen concentration the lower is M_s [64]). Nitrogen-austenite regions at the very surface contain the highest nitrogen content and thus the lowest M_s. For the employed nitriding conditions the expected surface nitrogen concentration is 9.5 at.% [47, 50] which corresponds to a M_s temperature of approx. -50 °C [64]. Consequently, the nitrogen-austenite phase close to the surface, i.e. the nitrogen austenite with the highest nitrogen content in the specimen, is preserved upon quenching to room temperature.

Similar to pore formation in nitrogen-ferrite specimens, the pore-formation tendency is lower for the Fe-*Me* alloys with alloying elements which more or less easily precipitate as nitrides (i.e. *Me* = Al, Cr and Si) and the pore-formation tendency is higher for alloying elements which cannot precipitate, in the practice of the current experiments, as alloying element nitrides (i.e. *Me* = Co, Ge and Ni).

The non-occurrence of nitrogen austenite (at the surface) in the case of the nitrided Fe-Si alloy (Figure 16 and Figure 17) can be ascribed to Si being the strongest ferrite stabilizing alloying element, as compared to Co, Ni and Ge.

Nitrided Fe-Ni alloy shows a microstructure which is comparable to the microstructure of nitrided pure iron (cf. Figure 15a and Figure 16e). A pronounced layer of nitrogen martensite with a thickness of approximately 200 μm (see what follows) is visible in the light optical micrograph and the EBSD-phase-map inset (see Figure 16e).

The thickness of the nitrogen austenite/martensite layers is much smaller in the Fe-*Me* alloys which are alloyed with ferrite stabilizing alloying elements such as Al, Cr and Ge (Ni is an austenite stabilizing element). Also, the occurrence of pronounced pore development, as in case of the Fe-Co alloy, obstructs growth of the nitrogen-austenite layer, because the nitrogen that could be used for nitrogen-austenite-layer growth gets lost by pore development.

3.6. Conclusions

- The thermodynamic instability of pure nitrogen ferrite can in principle induce its decomposition in nitrogen depleted ferrite and nitrogen gas. This nitrogen gas development leads to the formation of pores at grain boundaries, as shown in this project for the nitrided ferrite matrix of pure iron. Strikingly, a single crystal of nitrided, pure ferritic iron did not show porosity development.

- The nitrogen gas pressure in closed pores exceeds the critical value for yielding according to both the von Mises criterion and the Tresca criterion and the matrix surrounding the pores visibly yields as for example exhibited by bulging out of the specimen surface.
- The thermodynamic instability of pure nitrogen austenite induces its decomposition in nitrogen depleted austenite and nitrogen gas leading to pore development similar as in nitrogen ferrite. The driving force for this process is much larger than for the decomposition of nitrogen ferrite. The decomposition of nitrogen austenite into *nitrogen ferrite* and N_2 gas is thermodynamically possible but the release of Gibbs energy is small in comparison with the decomposition of nitrogen austenite into *nitrogen depleted austenite* and N_2 gas. The ferrite phase can reemerge if the nitrogen depletion of the austenite, surrounding channels (at grain boundaries) in contact with the outer surface, continues.
- Alloying elements that enhance the nitrogen equilibrium solubility in iron, i.e. Al and Cr, and that precipitate easily as nitrides, such as AlN and CrN, exhibit less pronounced pore formation than pure iron.
- Alloying elements that reduce the nitrogen equilibrium solubility in iron, i.e. Co and Ge, and that do not precipitate easily as nitrides, promote the formation of pores as compared to pure iron.
- Si dissolved in iron lowers the nitrogen equilibrium solubility in iron and precipitates (very slowly) as (amorphous) Si_3N_4. The pore formation at ferrite-grain boundaries is retarded due to the development of amorphous Si_3N_4 bands along the grain boundaries which inhibits nucleation of N_2 gas filled pores at the grain boundaries.

Acknowledgements

The authors thank Mr. Dipl.-Ing. (FH) P. Kress and Mr. W. Engelhardt for assistance with the nitriding experiments, Dr. E. Bischoff for EBSD investigation and discussion, Dipl.-Ing. P. J. Rossi for SEM investigation and Mrs. S. Haug for EPMA analysis (all with the Max Planck Institute for Intelligent Systems, Stuttgart).

Chapter 4

Nitriding of Iron-based Ternary Fe-V-Si Alloy;

The Precipitation Process of Separate Nitrides

Benjamin Schwarz, Sai R. Meka, Ralf E. Schacherl,

Ewald Bischoff and Eric J. Mittemeijer

Abstract

Iron-based ternary Fe-V-Si and binary Fe-Si alloy specimens were nitrided in a NH_3/H_2 gas mixture at 580 °C (853 K) with a nitriding potential of $r_N = 0.1$ atm$^{-1/2}$ until nitrogen saturation in the specimens was achieved. In contrast to previously investigated iron-based ternary Fe-Al-Cr and Fe-Ti-Cr alloys, no so-called "mixed" nitrides developed in the Fe-V-Si alloy. Instead, in a first stage all vanadium precipitated as *crystalline* VN and subsequently all silicon precipitated as *amorphous* Si_3N_4. Moreover, the precipitation rate of Si_3N_4 in the nitrided ternary Fe-V-Si alloy was much lower than in the binary Fe-Si alloy nitrided under identical conditions. This much lower Si_3N_4-precipitation rate is attributed to the presence of first precipitated VN: coherency strains caused by the (semi-) coherent VN precipitates interact with the strain fields surrounding the Si_3N_4 precipitates and are obstacles for movement of dislocations necessarily introduced in the ferrite matrix by growing Si_3N_4 precipitates. This interpretation is supported by additional experiments where the first precipitated VN platelets were coarsened by annealing, before subsequent nitriding led to, now much faster, Si_3N_4 precipitation.

4.1. Introduction

Nitriding is a widely used thermochemical surface treatment for components made of ferritic iron-based alloys. Nitriding can greatly improve the mechanical properties, as the wear and the fatigue resistances, as well as the chemical properties, as the corrosion resistance [1-3]. Different nitriding methods exist: gas nitriding, plasma nitriding and salt-bath nitriding. In contrast to the other nitriding methods, gas nitriding offers the advantage to be able to precisely adjust the chemical potential of nitrogen in the nitriding medium. Thereby it is in principle possible to control the developing phases and microstructures upon gas nitriding [7].

Gas nitriding is performed with a flowing NH_3/H_2 gas mixture. During nitriding, NH_3 molecules dissociate catalytically on the iron surface leading to atomic nitrogen adsorbed at the surface [66, 67]. The adsorbed nitrogen atoms can be dissolved in the solid of the surface and subsequently diffuse to larger depths in the substrate. By choosing appropriate nitriding parameters (temperature and nitriding potential; for details see Ref. [7]) the formation of iron nitrides can be avoided, so that only a nitrogen-diffusion zone develops.

If the iron is alloyed with elements, *Me*, having an affinity for nitrogen (e.g. *Me* = Al, Ti, V, Cr, or Si), alloying-element nitrides can develop in the diffusion zone upon nitriding. These precipitated (semi-) coherent nitrides can induce pronounced improvement of the fatigue resistance of nitrided work-pieces [11].

Most studies on nitriding response dealt with ferritic iron-based *binary* Fe-*Me* alloys [10, 57, 68-70]. In contrast, commercial nitriding steels contain multiple alloying elements, each of specific interaction with nitrogen. Until now few studies were devoted to the nitriding behavior of *ternary* iron-based Fe-Me_a-Me_b alloys (Fe-Mn-Si [20], Fe-Cr-Al [21-23], Fe-Cr-Ti [24, 25], Fe-Al-Si [26]). In case of nitrided Fe-Cr-Al [21-23] and Fe-Cr-Ti [24, 25] alloys, it was recently found that metastable, mixed ternary nitrides, $Me_{a(1-x)}Me_{b(x)}N$, develop, instead of the stable,

binary nitrides, Me_aN and Me_bN. Strikingly, these mixed ternary nitrides develop in systems for which the separate binary nitrides are of the same stoichiometry (i.e. same *Me*/N atomic ratio) and of the same crystal structure (cubic rock-salt type crystal structure).

With respect to the above discussion the question arises what happens upon nitriding if in one (iron-based) alloy, two alloying elements, both having a strong chemical affinity for nitrogen (as in the above cases), are dissolved, but which show upon nitriding of the corresponding binary alloys rather different nitriding behaviors, as for example exhibited by different *Me*-N stoichiometries for the binary nitrides. Upon nitriding binary Fe-V alloys, V precipitates rapidly as stoichiometric VN of rock-salt type crystal structure [71]. Upon nitriding binary Fe-Si alloys, Si precipitates relatively slowly as stoichiometric Si_3N_4 which is of amorphous nature [16-18]. The investigation of the nitriding responses of V and Si jointly present in a ternary Fe-V-Si alloy is the subject of the present research project.

It will be shown that, albeit no mixed ternary nitride precipitates, but separate binary nitrides develop, the kinetics of nitride precipitation in the ternary alloy differs remarkably from what is observed for the corresponding binary alloys. A corresponding explanation is offered on the basis of additional, dedicated experiments.

4.2. Experimental procedures

4.2.1. Specimen preparation

The iron-based binary Fe-Si alloy and the iron-based ternary Fe-V-Si alloy casts were produced by melting elemental granules of Fe (purity 99.98 wt.%), V (purity 99.9 wt.%) and Si (purity 99.999 wt.%) in an induction furnace under a protective Ar atmosphere. The melts were cast to rods with a length of 100 mm and a diameter of 10 mm. These casts were ground to

remove surface oxides and cold-rolled to sheets with a thickness of approximately 1 mm. Rectangular prism-shaped specimens with the dimension (15 × 10 × 1) mm were cut from these sheets. The specimens were ground, polished (last step was 1 µm diamond paste) and finally ultrasonically cleaned in ethanol. Next, the specimens were encapsulated in quartz tubes under a protective Ar atmosphere and recrystallized at 800 °C for 20 min. Subsequently the specimens were again polished (1 µm diamond paste) and cleaned ultrasonically in ethanol.

Inductively coupled plasma optical emission spectroscopy (ICP-OES) was used to determine the actual amounts of V and Si in the casts, carrier gas hot extraction was used to determine the amounts of oxygen and nitrogen, and the combustion method was applied to determine the amounts of carbon and sulfur. The results of the chemical analysis of the different alloys have been gathered in Table 1.

Table 8: Alloying element and light element impurity contents in the pure iron, the binary iron-based Fe-Si alloy and the ternary Fe-V-Si alloy casts prepared and employed in the present work.

alloy	V [at.%]	Si [at.%]	O [µg/g]	N [µg/g]	C [µg/g]	S [µg/g]
Fe	-	-	70	< 10	< 10	< 10
Fe-2.0Si	-	1.99 ± 0.02	30	< 20	< 10	< 20
Fe-0.3V-2.0Si	0.29 ± 0.01	1.97 ± 0.01	60	< 20	< 10	< 20

4.2.2. Nitriding

Gas nitriding treatments were performed in a vertical multi-zone quartz-tube furnace (inner diameter 28 mm) which was equipped with gas mass-flow (flow variation ±2.5 ml/min) and

temperature (temperature variation ±1 K) controllers (see Ref. [4] for a detailed description of the nitriding facility). Nitriding was performed at a temperature of 580 °C using a nitriding potential of r_N = 0.1 $atm^{-1/2}$ (45 ml/min NH_3 and 455 ml/min H_2; nitriding potential is defined as $r_N = p(NH_3)/p(H_2)^{3/2}$, where p denotes partial pressure [3]). For the nitriding treatment high purity NH_3 (purity 99.998 vol.%) and H_2 (purity 99.999 vol.%) gases were used. Note that upon applying this nitriding condition, no iron nitrides (ε-Fe_3N_{1+x} or γ′-Fe_4N_{1-y}) can develop upon nitriding pure iron [6] and did not develop in case of nitriding the iron-based alloys investigated in this study. The nitriding treatments were interrupted at certain times by quenching the specimens in water which was purged with N_2 gas to minimize the amount of oxygen dissolved in the water. The first set of specimens was nitrided for 1 h, 4 h, 8 h, 24 h. The second set of specimens was nitrided in steps of 72 h to a total time of 1656 h.

4.2.3. Weighing

The specimens were weighed with a comparator balance (Mettler XP56) before and after each nitriding treatment. For each weighing, five measurements were carried out and the mean, taken as the nitrogen uptake, and its standard deviation were calculated.

4.2.4. X-ray diffraction

An X´Pert MPD (multi-purpose diffractometer) from PANalytic employing Co-K_α radiation and Bragg-Brentano geometry was used to record X-ray diffraction (XRD) patterns. The MPD, operating in Bragg-Brentano geometry, was equipped with a graphite monochromator in the diffracted beam and an X´Celerator detector from PANalytic. The diffraction-peak positions were

determined using the X´Pert Highscore software and from these data the present phases were identified using the data-base from the International Center for Diffraction Data (ICDD) [12].

4.2.5. Microhardness measurement

For cross-sectional analysis a part of the specimens was removed by a cut perpendicular to the nitrided surface. Such parts were embedded in Struers Polyfast. The cross-sections were ground and polished. Hardness-depth profiles were determined employing a Vickers microhardness tester VMHT MOT from Leica, applying a load of 100 g for 10 s. Each hardness value presented for the nitrided ternary Fe-V-Si alloy specimens is the average of three corresponding indentations made in the cross-section at the same depth beneath the surface of the specimen. Hardness values of the unnitrided Fe-V-Si alloy specimen and of the nitrided pure iron specimen were determined as the average of 10 hardness indentations at different lateral positions on cross-sections of the specimens.

4.2.6. Transmission electron microscopy

In order to obtain electron transparent specimens, discs with a diameter of 3 mm were cut out from nitrided specimens. The thickness of the discs was reduced by removing material from both sides by polishing and dimpling. The final thinning method was either electropolishing or ion milling. In case of electropolishing a Struers TenuPol-5 apparatus was used (electrolyte: 85 vol.% acetic acid and 15 vol.% perchloric acid), whereas ion milling was performed using the Model 1010 from Fischione. Bright field (BF), dark field (DF) images and selected area diffraction patterns (SADP) were recorded with a Gatan CCD camera attached to a Philips CM 200 transmission electron microscope (TEM) operated at an acceleration voltage of 200 kV. This TEM is equipped with an energy-dispersive X-ray detection system (EDX); (semi-) quantitative

element analysis was performed using the software Gemini from EDAX. Calibration of the camera constant was realized by using ferrite-matrix diffraction spots where the lattice spacings, *d*, are known. For indexing diffraction spots in the SADPs the corresponding *d* values were calculated by measuring the distances *R* of these spots from the center in the SADPs using the software Digital Micrograph Diffpack from Gatan and comparing these *d* values with the lattice-parameter data provided by the ICDD data base [12].

4.3. Results and evaluation

4.3.1. Nitrogen uptake and precipitate development

Specimens of iron-based ternary Fe-V-Si alloy (see Table 8 for exact composition) were nitrided until no further nitrogen uptake was detectable. It should be noted that through nitriding of the 1 mm thick specimens has been achieved after about 24 h of nitriding (see below). The resulting curve of nitrogen uptake as a function of nitriding time can be subdivided into stages I and II (see Figure 19):

Stage I: The period of nitriding time shorter than 30 h is characterized by an initially fast increase of the nitrogen content until, practically, a plateau is reached. This plateau level corresponds with a nitrogen content slightly smaller than the nitrogen content of 0.58 at.% that would occur if (i) all V has precipitated as stoichiometric VN ($[N]_{VN}^{chem}$ = 0.29 at.%, cf. Table 8) and (ii) the remaining ferrite (α-Fe) matrix would be saturated with nitrogen at the given temperature and nitriding potential as for pure iron ($[N]_{\alpha}^{0}$ = 0.29 at.% according to Ref. [45]).

Hardness-depth profiles were obtained from cross-sections after nitriding (see Figure 20). Nitriding of 1 mm thick ternary Fe-V-Si alloy specimen for 1 h leads to a significant hardness increase (more than 250 %) at the specimen´s surface. Upon continued nitriding up to 24 h, the

hardness gradient reduces until no gradient in hardness occurs throughout the complete specimen´s thickness.

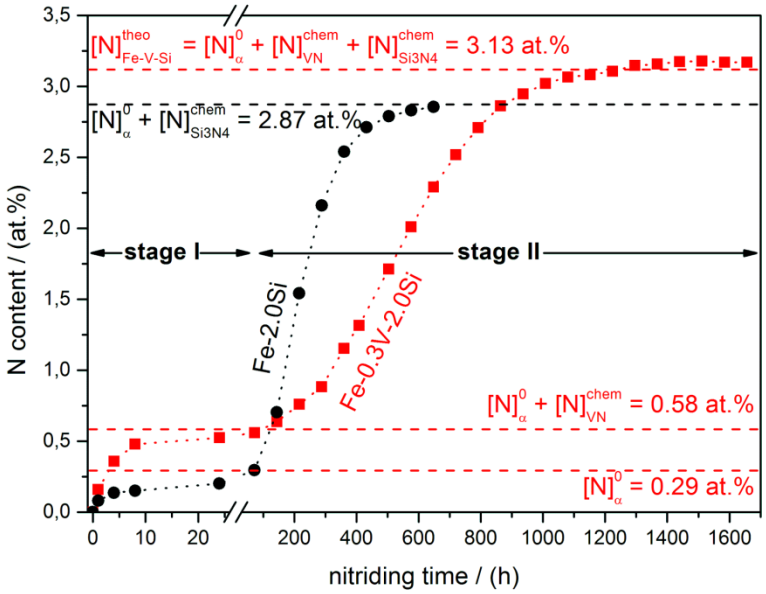

Figure 19: Nitrogen content as a function of nitriding time for ternary Fe-V-Si and binary Fe-Si alloy specimens nitrided at 580 °C applying a nitriding potential of 0.1 $atm^{-1/2}$. Nitrogen-uptake curves can be subdivided in stages I and II: Stages I and II have been indicated for the nitriding of the ternary Fe-V-Si alloy (see text for discussion).

In order to characterize the nitrides precipitated in this stage I, TEM analysis was performed. A TEM BF image recorded after nitriding for 24 h (end of stage I in Figure 19) and the corresponding SADP are presented in Figure 21. A “tweed-like” contrast can be seen in this image due to finely-dispersed and nano-sized precipitates. The shape of the precipitates is platelet-like with a length of approximately 5 nm. The precipitates developed along $\{100\}_\alpha$-habit planes and are surrounded by a coffee-bean like contrast ([72]; see magnified region next to the BF image). The corresponding SADP recorded in $[001]_\alpha$-zone axis reveals streaks of intensities

along $[100]_\alpha$ and $[010]_\alpha$ directions with intensity maxima at positions corresponding very well to those of VN of rock-salt crystal structure type oriented in Bain orientation ($(100)_\alpha \parallel (100)_{VN}, [010]_\alpha \parallel [011]_{VN}$) with respect to the ferritic (α-Fe) matrix. These streaks of intensities are a consequence of strain broadening due to the development of (semi-) coherent nitride platelets on $\{100\}_\alpha$-habit planes (the maximal misfit strain occurs in $\langle 100 \rangle_\alpha$ directions perpendicular to the nitride platelets) and the very thin nature of the nitride platelets.

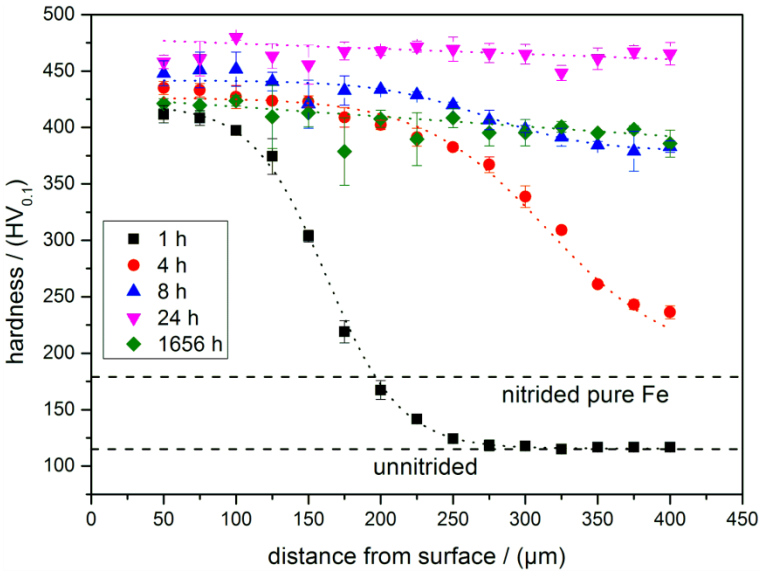

Figure 20: Hardness-depth profiles of ternary Fe-V-Si alloy specimens nitrided for different times at 580 °C applying a nitriding potential of 0.1 $atm^{-1/2}$. Nitriding leads to a significant hardness increase due to precipitation of VN and Si_3N_4. The thickness of the nitrided case is increasing with nitriding time until a constant hardness through the complete thickness of the specimen is achieved after 24 h (end of stage I in Figure 19). Prolonged nitriding for 1656 h (end of stage II in Figure 19) leads to a hardness drop associated with coarsening of the initially (in stage I) precipitated VN particles.

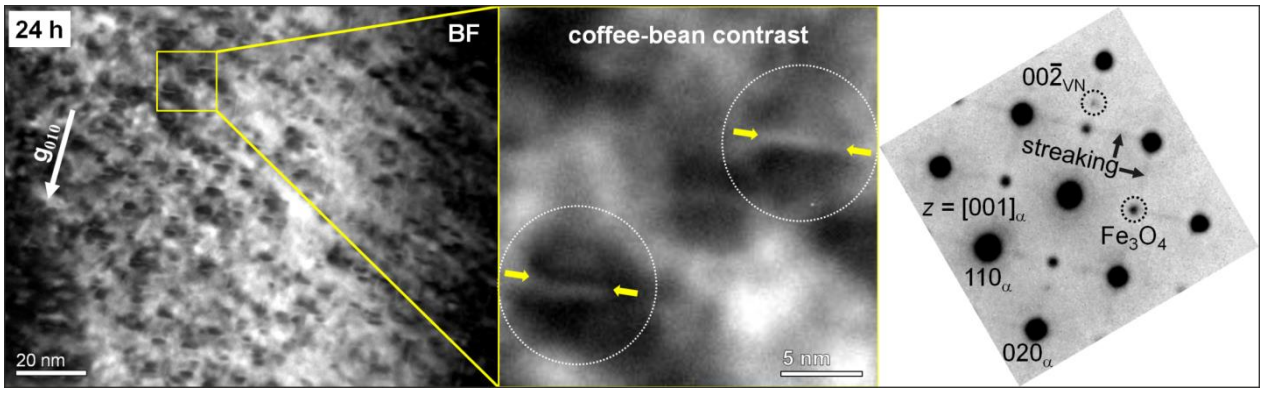

Figure 21: A TEM BF image recorded from a ternary Fe-V-Si alloy specimen after nitriding at 580 °C applying a nitriding potential of 0.1 $atm^{-1/2}$ for 24 h (end of stage I in Figure 19). Nano-sized, platelet-like precipitates developed along $\{100\}_\alpha$-habit planes causing a coffee-bean like contrast (see magnified region; arrows indicate the platelet length). The corresponding SADP (with $[001]_\alpha$.-zone axis) reveals diffraction spots of the ferrite matrix (α) (and iron oxide, Fe_3O_4; due to surface oxides on the TEM foil) and streaks of intensity along $[100]_\alpha$ and $[010]_\alpha$ directions with intensity maxima at the positions corresponding to diffraction maxima of VN of rock-salt crystal structure type oriented in Bain orientation with respect to the ferritic matrix.

XRD-patterns recorded from the surface of an unnitrided specimen and after nitriding for 24 h (end of stage I in Figure 19) are shown in Figure 22a. After nitriding for 24 h, (still) only ferrite peaks can be observed. However, the 200_α peak reveals pronounced diffraction-line broadening as compared to that of an unnitrided specimen; the broadening is asymmetrical: a distinct shoulder/tail towards higher diffraction angles can be observed (see Figure 22b). The mass-increase, the TEM and the XRD results indicate at this stage (only, all) V has precipitated as VN and that the VN particles diffract coherently with the ferritic matrix (see Ref. [71]). Evidently, in stage I no sign of participation of Si in the precipitation process occurring in the ferritic grains is apparent.

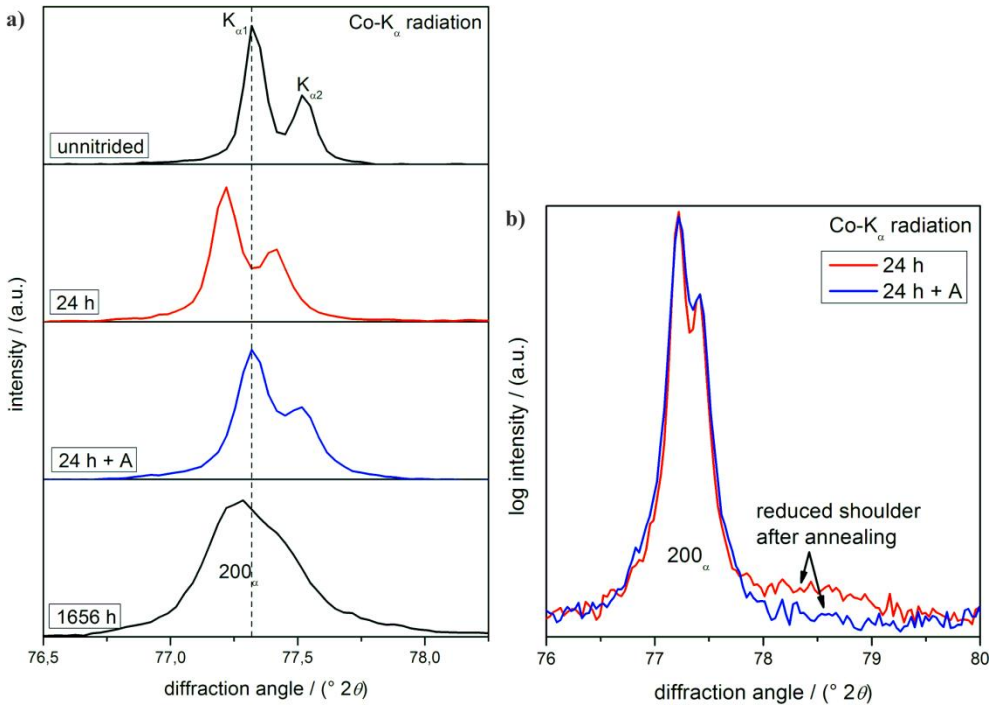

Figure 22: X-ray diffractograms (normalized with respect to integrated intensity) as recorded from the surface of ternary Fe-V-Si alloy specimens before nitriding, after nitriding and after nitriding + annealing (A). Nitriding treatments were performed at 580 °C applying a nitriding potential of 0.1 $atm^{-1/2}$ for 24 h and 1656 h. The annealing treatment (subsequent to nitriding for 24 h) was performed at 750 °C for 24 h. Beside ferrite peaks, no additional peaks can be observed after nitriding. **a)** Comparison of the 200_α peaks before and after nitriding (24 h and 1656 h) reveals a ferrite-peak shift to smaller diffraction angles and ferrite-peak broadening. Annealing (after nitriding; 24 h + A) leads to a reversal of the ferrite-peak shift and, as shown in **b)**, a distinct reduction of the ferrite-peak shoulder at higher diffraction angles. Note that, in order to clearly show the decrease of the ferrite-peak shoulder upon annealing, in b) the 200_α peak for the 24 h + A specimen has been shifted on the 2θ scale such that the maxima positions of the peaks recorded for the 24 h and 24 h + A specimens coincide.

Stage II: Continued nitriding (t > 30 h) leads at first only to a moderate increase of the nitrogen content (see Figure 19), followed, after a nitriding time of approximately 100 h, by a pronounced nitrogen-uptake rate which in turn starts to decelerate after about 500 h of nitriding, to attain, after about 1500 h of nitriding, a saturation level of nitrogen content is achieved: A sigmoidal shaped nitrogen-uptake curve occurs suggesting a heterogeneous nitride precipitation proceeding by nucleation and growth [11]. The final saturation level of nitrogen is in good agreement with the amount of nitrogen expected if, all Si has precipitated as stoichiometric Si_3N_4, all V has precipitated as stoichiometric VN, and the remaining ferrite matrix is saturated with nitrogen ($[N]^{chem}_{VN}$ = 0.29 at.%, $[N]^{chem}_{Si_3N_4}$ = 2,63 at.%, $[N]^{0}_{\alpha}$ = 0.29 at.%; $[N]^{theo}_{Fe\text{-}V\text{-}Si} \equiv [N]^{chem}_{VN} + [N]^{chem}_{Si_3N_4} + [N]^{0}_{\alpha}$ = 3.13 at.%).

TEM images recorded from a specimen nitrided for 216 h (beginning of stage II in Figure 19) are shown in Figure 23a. The BF image (Figure 23a1) reveals, in addition to the finely-dispersed, tiny VN platelets (see discussion for stage I), much bigger cubical Si_3N_4 precipitates. The (semi-) quantitative EDX analysis (cf. Section 4.2.6) performed in the TEM on a Si_3N_4 particle (which upon electropolishing remained at the edge of the TEM foil by selective dissolution of ferrite matrix) revealed that the particle is composed of Si and nitrogen with more nitrogen than Si atoms. The edge length of these cubical Si_3N_4 precipitates is approximately 100 nm and the cube faces are parallel to the $\{100\}_{\alpha}$ planes (as observed for nitrided binary Fe-Si alloys in Refs. [17, 18]).

The thickness of the TEM foil is smaller than the size of the Si_3N_4 particles, which thus extend from top to bottom in the foil shown in Figure 23a. Hence, it follows that VN platelets are also present *within* these cubical Si_3N_4 precipitates: see the DF image produced using the $00\bar{2}_{VN}$-diffraction spot (Figure 23a2) which reveals the presence of tiny VN platelets by a distinctive

bright contrast with their surroundings. In the same DF image the larger cubical Si_3N_4 precipitates exhibit a relatively bright contrast within the ferrite matrix as well. Recognizing that no diffraction spot of any crystalline Si_3N_4 is detectable, it is suggested that the cubical Si_3N_4 precipitates are amorphous (because the corresponding diffuse scattered intensity is able to pass the objective lens aperture). The occurrence of amorphous Si_3N_4 precipitates was observed for nitriding binary Fe-Si alloys [16-19]. The highly unusual precipitation of an amorphous precipitate in a crystalline matrix has been attributed to the thermodynamic stabilization of small amorphous Si_3N_4 particles due to a lower energy of the amorphous/crystalline interface as compared to that of the crystalline/crystalline interface [16].

TEM micrographs recorded from a specimen nitrided for 1656 h (saturation level of nitrogen; see Figure 19) are shown in Figure 23b. The finely dispersed VN precipitates shown in this micrograph now have a length between 15 nm to more than 50 nm, but they are still very thin. Size and morphology of the amorphous Si_3N_4 precipitates have changed remarkably as compared with the beginning of stage II (cf. Figure 23a1 and 23b1). Preferential growth at the corners of the cubes resulted in a (presumably) octapod-shape of the precipitates (see recent work on nitriding binary Fe-Si alloy [19]). The morphological change of amorphous Si_3N_4 precipitates from cubical to presumably octapod-shape is attributed to the anisotropic growth of the misfitting Si_3N_4 precipitate due to anisotropic misfit-stain field in the precipitate surrounding elastically anisotropic matrix [19].

The SADP pertaining to the BF image shown in Figure 23b1 shows, besides diffraction spots from the ferrite matrix, now clear diffraction spots from VN. Further, (still) no diffraction spots from Si_3N_4 are observed; instead, a more intense diffuse intensity (“halo”) is observed around the primary electron beam caused by electron scattering by the amorphous Si_3N_4 precipitates. The DF image recorded using the 002_{VN}-diffraction spot is shown in Figure 23b2.

It (again; see above) follows that the VN platelets occur both in the ferrite matrix and within the (now) octapod-shaped Si_3N_4 precipitate.

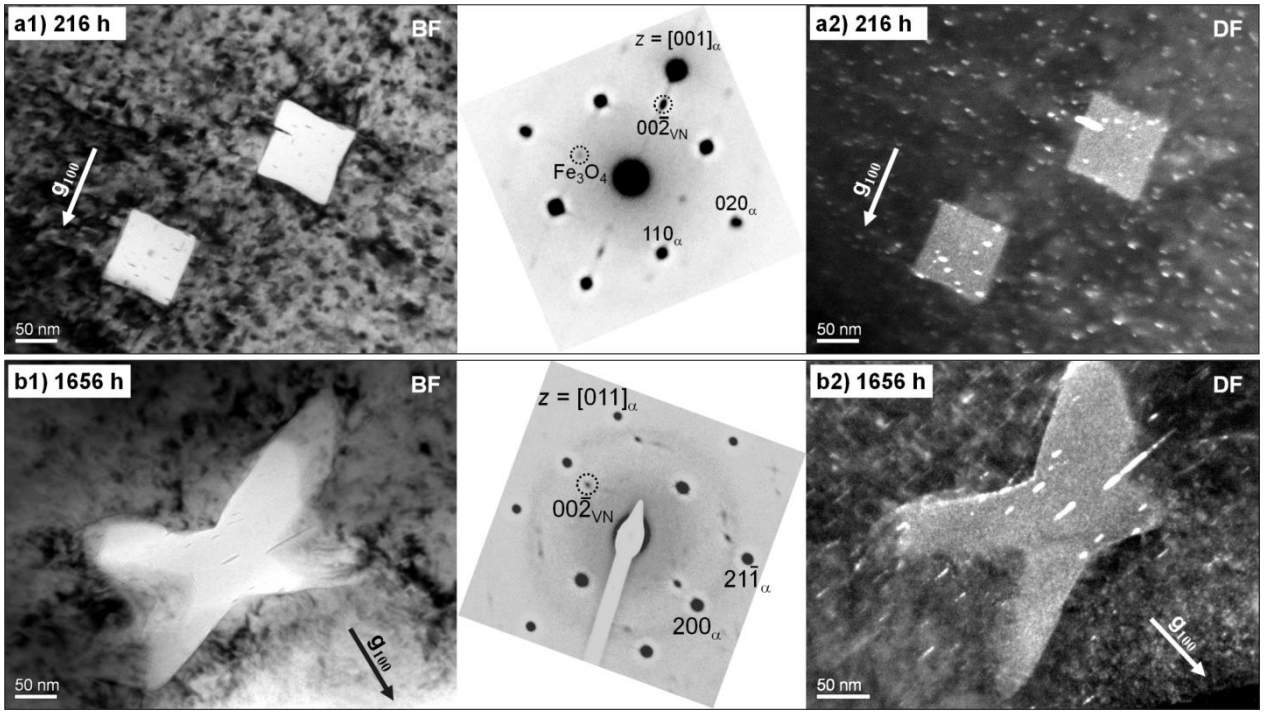

Figure 23: TEM images recorded from ternary Fe-V-Si alloy specimens after nitriding (580 °C, 0.1 $atm^{-1/2}$) for different (long) nitriding times (stage II in Figure 19). **a)** Specimen nitrided for 216 h shows large cubical Si_3N_4 precipitates which have overgrown tiny VN precipitates. The SADP shows diffraction spots from ferrite (iron oxide (Fe_3O_4); see caption of Figure 21) and VN. The $00\bar{2}_{VN}$-diffraction spot was used to record the DF image shown in Figure 23a2. This DF image exhibits crystalline VN particles in the ferrite matrix and within the cubical Si_3N_4 particles and the Si_3N_4 particles appear also bright due to the diffuse intensity resulting from electron scattering by the amorphous Si_3N_4 precipitates. **b)** Specimen nitrided for 1656 h): BF image shows a cut through an octapod-shaped Si_3N_4 precipitate with VN platelets within. The SADP shows diffraction spots belonging to ferrite and VN and a diffuse intensity ("halo") around the primary electron beam due to electron scattering by the amorphous Si_3N_4 precipitates.

4.3.2. Role of the initially precipitated VN on the kinetics of the later precipitating Si_3N_4

The nitrogen uptake of a binary Fe-Si alloy, nitrided in this work under the same conditions as applied to the ternary Fe-V-Si alloy (both of similar Si content, see Table 8), is shown in Figure 19 as well. It follows that the precipitation process of Si_3N_4 is much slower in the ternary Fe-V-Si alloy (stage II in Figure 19) than that in the binary Fe-Si alloy, also considering for the ternary alloy only the time after all VN has precipitated (i.e. after stage I). Thus the question emerges if and how this retardation of Si_3N_4 precipitation is related to the preceding precipitation of VN in the ternary Fe-V-Si alloy.

In order to assess the role of the nano-sized nature of the VN precipitates and their associated coherency-strain fields on the subsequent Si_3N_4 precipitation, a ternary Fe-V-Si alloy specimen was nitrided for 24 h to precipitate first all V as VN (note that after 24 h of nitriding Si_3N_4 precipitation in the ferritic grains has not started yet). Subsequently this specimen was encapsulated in a quartz tube under protective Ar atmosphere and annealed at 750 °C for 24 h to coarsen the VN precipitates. A TEM investigation was performed after this nitriding + annealing treatment to investigate the effect of annealing on the VN precipitates: the TEM BF image in Figure 23a shows coarsened VN platelets along $\{100\}_\alpha$ planes of the ferrite matrix with a length varying from 90 nm to 140 nm (length before the annealing treatment was only about 5 nm; cf. Figure 21). Further, the VN precipitates have become incoherent with the surrounding ferrite matrix, as evidenced from the disappearance of coherency-strain contrast around the platelets in the BF image and the VN intensity maxima becoming more prominent in the in the corresponding SADP. The reduction of stresses in the ferrite matrix surrounding the VN is also indicated by a reversal of the ferrite-peak shift and by the disappearance of the shoulder at the high angle side of the 200_α reflection after annealing (see Figure 22b). The ferrite-lattice

parameter after nitriding + annealing amounts to (2.866 ± 0.001) Å and is therefore comparable with the ferrite-lattice parameter of strain-free ferrite (2.865 ± 0.001) Å.

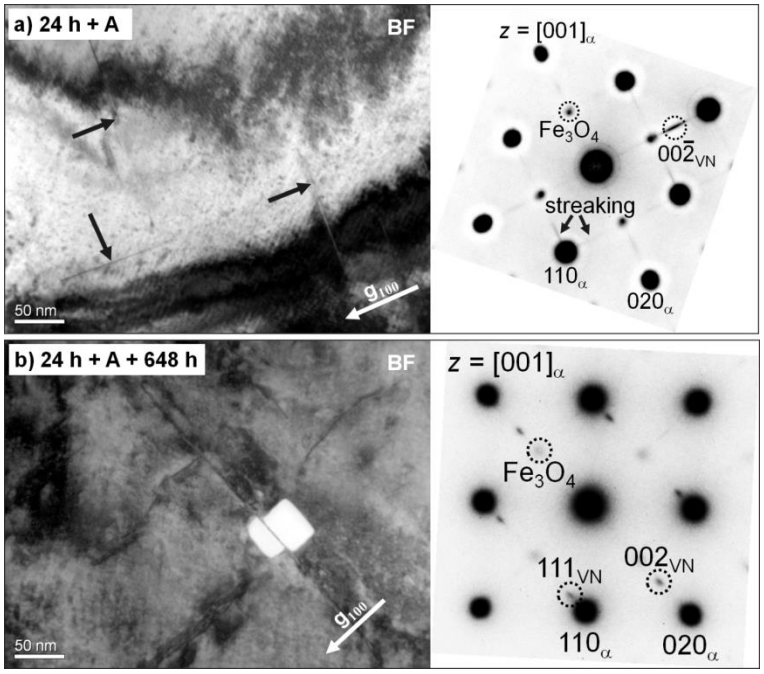

Figure 24: TEM BF image recorded from a ternary Fe-0.3V-2.0Si alloy specimen after nitriding (580 °C, 0.1 $atm^{-1/2}$, 24 h) and subsequent annealing (under protective Ar atmosphere at 750 °C for 24 h). The VN precipitates (arrows) have coarsened after annealing; the precipitates have become relatively long but are still very thin (1 – 2 nm); distinct contrast due to coherency stresses surrounding these precipitates cannot be observed anymore. The corresponding SADP (with $[001]_\alpha$.-zone axis) shows diffraction spots from ferrite (iron oxide (Fe_3O_4); see caption of Figure 21), reduced streaking along $[100]_\alpha$ and $[010]_\alpha$ directions and now clearer intensity maxima at the positions corresponding to diffraction maxima of VN of rock-salt crystal structure type oriented in Bain orientation with respect to the ferritic matrix. **b)** TEM BF image recorded from the same specimen after a subsequent nitriding treatment of 648 h leading to nitrogen saturation (see Figure 25). Si_3N_4 has precipitated on the faces of a coarsened VN precipitate.

After this first nitriding + annealing step the nitriding treatment was continued until saturation, i.e. until no further nitrogen uptake was detectable. The thus obtained nitrogen-content curve as a function of nitriding time is shown in Figure 25. Additionally, the nitrogen uptake vs. time curves of the ternary Fe-V-Si alloy specimen and the binary Fe-Si alloy specimen which were "conventionally" nitrided (i.e. no annealing step in between) are presented in Figure 25, too.

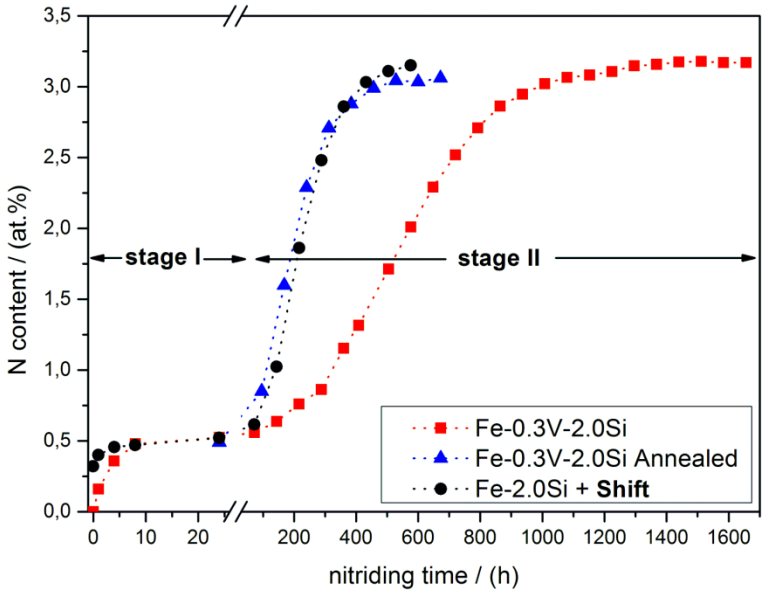

Figure 25: Nitrogen content as a function of nitriding time for ternary Fe-V-Si alloy and binary Fe-Si alloy specimens nitrided at 580 °C applying a nitriding potential of 0.1 $atm^{-1/2}$. The curve of the nitrided binary Fe-Si alloy has been shifted to higher values (for better comparison) to compensate for the nitrogen which is chemically bonded as stoichiometric VN in the nitrided ternary Fe-V-Si alloy. The curve consisting of black circles represents the ternary Fe-V-Si alloy specimen which was (i) nitrided for 24 h to precipitate all vanadium as VN, followed by (ii) annealing at 750 °C for 24 h and thereafter subjected to (iii) nitriding until a constant nitrogen level was achieved after 648 h.

Note that the nitrogen-content values of the nitrided binary Fe-Si alloy in Figure 25 have been shifted to higher values (+ 0.29 at.% N) to compensate for the additional nitrogen uptake by the ternary Fe-V-Si alloy due to the (already) precipitated stoichiometric VN. Evidently, the nitriding of the nitrided + annealed Fe-V-Si alloy specimen leads to a much faster Si_3N_4-precipitation: in fact, the nitrogen-uptake rate of the first nitrided + annealed ternary alloy is equal to that of the binary Fe-Si alloy. (Note that the nitriding time needed for full VN precipitation can be neglected as compared to both the nitriding time of the binary Fe-Si alloy and the subsequent nitriding time of the first nitrided + annealed Fe-V-Si alloy).

4.4. General discussion

4.4.1. Separate and successive precipitation of VN and Si_3N_4

The experimental evidence presented in this investigation (Section 4.3) demonstrates that upon nitriding the ternary Fe-V-Si alloy, first all V precipitates as VN and thereafter all Si precipitates as Si_3N_4. This behavior is strikingly different from what is observed for nitrided Fe-Cr-Al and Fe-Cr-Ti alloys where "mixed" $Me_{a(1-x)}Me_{b(x)}N$ nitrides develop. These observations can be rationalized considering an *Me*-N interaction parameter as originally defined in Ref. [14]:

$$I = -\frac{\Delta G_{MeN_n}}{W_{strain}} \qquad \text{(Eq. 15)}$$

where ΔG_{MeN_n} is the change of the chemical Gibbs energy upon precipitation of MeN_n from the Fe-*Me*-N solid solution and W_{strain} is the associated misfit-strain energy according to Ref. [73]. Interaction-parameter values calculated for certain iron-based binary Fe-*Me* alloys (with *Me* = Ti, V, Al, Cr and Si) have been gathered in Table 9. The development of "mixed" $Me_{a(1-x)}Me_{b(x)}N$ nitrides upon nitriding Fe-Cr-Al and Fe-Ti-Cr alloys is suggested by *Me*-N interaction parameters

of distinctively positive value for both Me_a and Me_b. The interaction parameter for V-N (I = 1.7) and the interaction parameter for Si-N (I = 0.4) are not only largely different, but in particular for *Me* = Si the interaction parameter is, albeit positive, very small; thereby precipitation of a "mixed" nitride is less likely.

Table 9: Interaction parameter, I, defined as the ratio of the change of the chemical Gibbs energy upon precipitation of *Me* and N, both dissolved in α-Fe (ferrite), as MeN_n, at 773 K. $\Delta G_{MeN_n}^{773K} = \Delta G_{MeN_n}^{0} - n\Delta G_{N}^{\alpha\text{-Fe(N)}}$, where $\Delta G_{MeN_n}^{0}$ is the Gibbs energy of formation for one mole MeN_n and $\Delta G_{N}^{\alpha\text{-Fe(N)}}$ is the Gibbs energy of dissolution of 1 mole N in ferrite (Fe-*Me* interaction is ignored). $W_{strain} = 6G_{\alpha}C\varepsilon^{2}V_{MeN_n}$ is the misfit-strain energy developing upon precipitation of one mole MeN_n in ferrite, where G_{α} is the shear modulus of ferrite, C is given by $3K_{MeNn}/(3K_{MeNn}+4G_{\alpha})$, with K_{MeNn} as the bulk modulus of MeN_n, ε is the linear misfit parameter and V_{MeNn} is the molar volume of the nitride. The misfit-strain energy was calculated according to Ref. [14, 73] for the case of full elastic accommodation of the misfit.

Fe-*Me*	$\Delta G_{MeN_n}^{773K}$ / (kJ/mol)	W_{strain} / (kJ/mol)	$I = -\frac{\Delta G_{MeN_n}}{W_{strain}}$
Fe-Ti	-300	173	1.7
Fe-V	-186	112	1.7
Fe-Al	-275	272	1.0
Fe-Cr	-91	116	0.8
Fe-Mo	-31	128	0.2
Fe-Si	-210	523	0.4

Moreover, the development of "mixed" (V, Si)-nitride upon nitriding Fe-V-Si alloy appears less likely recognizing that the V-N bonding has a significantly less covalent character than the Si-N bonding [74]. Further VN has a cubic rock-salt type crystal structure [71] whereas (crystalline) β-Si_3N_4 has a hexagonal type crystal structure [75].

Nitriding of 1 h leads to an increase of the surface hardness of more than 250 % and this value exceeds by far the contribution which is induced by only interstitially dissolved nitrogen in pure ferrite (hardness of a nitrided pure ferrite specimen is only (179 ± 4) $HV_{0.1}$, as determined in this project for identical nitriding conditions); see Figure 20. Therefore, this significant hardness increase is a strong indication for the, at this stage, precipitating VN particles. The transition between the nitrided surface and the unnitrided core of the nitrided ternary alloy is smoother than in case of nitrided binary Fe-2.23 at.% V alloy [76]. This is a consequence of the relatively low V content in the present ternary Fe-V-Si alloy (0.29 at.% V; cf. Table 8): With decreasing alloying element content, the nitriding response as defined in Ref. [10] changes from "strong" to "weak", implying, at the same nitriding conditions, deeper penetration of nitrogen into the specimen and promoting homogeneous nitriding of a sufficiently thin specimen at a shorter time. In the present case, 24 h of nitriding was sufficient to establish a homogenously nitrided, though not saturated (!) specimen. Upon continued nitriding the nitrogen level in the specimen increases at all depths with the same amount until saturation is achieved.

The nitrogen content in the specimens close to the end of stage I (t = 24 h), recognizing that all V has precipitated as VN, suggests a smaller level of nitrogen saturation of the ferrite matrix than compatible with that of pure ferrite (cf. Section 4.3.1). This small deviation can be ascribed to the presence (at this stage) of the (still) substitutionally dissolved Si which is known to lower the equilibrium nitrogen solubility in ferrite [62]. The decrease of the nitrogen solubility in ferrite due to dissolved Si in the ferrite matrix overcompensates the increase of the nitrogen solubility

associated with the (small) amount of so-called "excess" nitrogen induced by the presence of the coherency-strain field of the precipitated (semi-) coherent VN [14, 77].

Nitriding of ternary Fe-V-Si alloy specimens for longer than 30 h gives rise to a nitrogen-uptake curve of sigmoidal shape (see Figure 19; stage II). Such a shape is characteristic for the "ideal-weak interaction" behavior as exhibited by nitrogen and Si in ferrite [17, 78] (see also the above discussion). Despite a relatively high (negative value for the) Gibbs energy of formation of Si_3N_4 in ferrite (cf. value for $\Delta G^{773K}_{Si_3N_4}$ in Table 2), the precipitation process of Si_3N_4 in ferrite is extremely slow due to a high volume misfit of the Si_3N_4 particle with the surrounding ferrite matrix (> 100 %, cf. the value for W_{strain} in Table 9). This large misfit is responsible for difficult nucleation and growth of the Si_3N_4 precipitates. In view of the large volume misfit it is no surprise that growing Si_3N_4 precipitates are associated with plastic deformation in the surrounding ferrite matrix (see the dislocation ring which surrounds a Si_3N_4 particle developed upon nitriding the iron-based binary Fe-Si alloy in Ref. [19]). Such misfit-induced dislocations can serve as new nucleation sites for Si_3N_4 (autocatalysis), thereby enhancing the precipitation rate. At the end of stage II, the precipitation rate of Si_3N_4 slows down, obviously due to the depletion of dissolved Si in the ferrite matrix (in the end volume diffusion of Si governs the nitriding rate).

VN particles are present in both, the ferrite matrix and inside the Si_3N_4 particles (see Figure 23). As the orientation of the VN particles in the ferrite matrix and in the cubical Si_3N_4 particles in the same ferrite grain is the same, it is thereby strongly suggested that the primarily (in stage I) precipitated VN is overgrown by later (in stage II) precipitating Si_3N_4 particles.

The very long nitriding time of 1656 h has led, in comparison to the nitriding treatment of 24 h, to a slight drop in hardness of about 100 $HV_{0.1}$, throughout the complete thickness of specimen (cf. Figure 20). This result can be discussed as follows: (i) Precipitation of Si_3N_4

particles in the ferritic matrix leads to a (moderate) hardness increase of about 140 $HV_{0.05}$ [17]. (ii) The 200_α peak has shifted to higher diffraction angles (smaller ferrite-lattice parameter) and the shoulder/tail at higher diffraction angles has become less pronounced (see Figure 22), which can be interpreted as a consequence of coarsening/loss of coherency of the initially extremely fine and nano-sized VN precipitates. It follows from (i) and (ii) that the decrease in hardness due to VN-precipitate coarsening overcompensates the increase in hardness due to Si_3N_4 precipitation.

4.4.2. Kinetics of Si_3N_4 precipitation

The VN particles precipitate in stage I as (semi-) coherent platelets along $\{100\}_\alpha$-habit planes in the ferritic matrix. The misfit parallel to a $\{100\}_\alpha$-habit plane is much smaller (2 %) than that perpendicular to it (44 %), as calculated using lattice parameters of α-Fe (ferrite) and VN [12]. The small misfit parallel to the broad faces of the platelet can be initially accommodated elastically and thus the surrounding ferrite matrix gets elongated along directions parallel to the platelet and gets compressed along the direction perpendicular to the platelet: a tetragonally distorted ferrite matrix surrounds the VN platelets.

Upon nitriding binary Fe-Si alloy and also the current ternary Fe-V-Si alloy, the amorphous Si_3N_4 precipitates develop as “cubes” with the cube faces parallel to $\{100\}_\alpha$ planes (cf. Section 4.3.1), presumably due to a favorable interface energy along these ferritic-matrix planes [16]. In view of the huge volume misfit (> 100 %) between the Si_3N_4 and the ferritic matrix, a severe compression of the ferrite matrix in directions perpendicular to the cube faces of the Si_3N_4 particles, i.e. in directions perpendicular to $\{100\}_\alpha$ planes, is expected. The VN platelets, precipitated in stage I, are associated with a considerable compressive component of stress in the

surrounding ferrite matrix perpendicular to $\{100\}_\alpha$ planes (see above), as well. Thus, it is suggested that the development of cubical Si_3N_4 precipitates, in stage II, is as compared to the already difficult precipitation of Si_3N_4 in unstressed ferrite as holds for binary Fe-Si alloy upon nitriding, is additionally obstructed by the *extra* enhancement of elastic strain energy upon precipitation of Si_3N_4 in the ferrite matrix already strained by the VN precipitates. Further, addressing the plastic accommodation of the misfit between Si_3N_4 precipitates and the ferrite matrix (see above), the finely-dispersed, tiny, (semi-) coherent VN precipitates (result of stage I), form efficacious obstacles for movement of dislocations, to be introduced for plastic accommodation of the Si_3N_4/α-Fe misfit (see above), and thus hinder Si_3N_4 development upon growth (in stage II). As a consequence of both discussed effects, the considerable retardation of the rate of precipitation upon nitriding the ternary Fe-V-Si alloy, as compared to nitriding of the binary Fe-Si alloy, can be understood.

Deliberate coarsening of VN precipitates, in the Fe-V-Si alloy after stage I, by the intermediate high temperature annealing treatment (relief of coherency-strain fields; see Section 4.3.2), then establishes for subsequent precipitation of Si_3N_4 a situation as occurs more or less upon nitriding the binary Fe-Si alloy. Further, the particle density of VN obviously reduces significantly upon coarsening. Thus pinning of dislocations introduced in the ferrite matrix upon precipitation of Si_3N_4 becomes much less pronounced. As a result the precipitation of Si_3N_4 in the ternary Fe-V-Si alloy with coarsened/incoherent VN particles, proceeds with the same rate as observed for the corresponding binary Fe-Si alloy (see Figure 25).

In case of the coarsened VN particles, Si_3N_4 can precipitate at the interface of the now coarsened/incoherent VN particles with the ferrite matrix and *grow* in the now relaxed matrix (see Figure 24b).

4.5. Conclusions

- In strong contrast to the precipitation of "mixed" nitrides, $Me_{a(1-x)}Me_{b(x)}N$, in Fe-Al-Cr and Fe-Cr-Ti alloys upon nitriding, in iron-based ternary Fe-V-Si alloy specimens, V and Si precipitate upon nitriding *separately and successively* as nitrides.
- First all V precipitates as finely-dispersed, nano-sized, crystalline VN platelets. The VN platelets have the rock-salt type crystal structure and obey a Bain orientation relation with the surrounding ferrite matrix. Subsequently all Si precipitates as much larger, amorphous, stoichiometric Si_3N_4 cubes with the cube faces parallel to $\{100\}_\alpha$ planes.
- Separate formation of VN and Si_3N_4 can be ascribed to a large difference in the *Me*-N interaction, in particular a very small Si-N interaction occurs, where the *Me*-N interaction comprises the effects of chemical affinity and misfit strain.
- The Si_3N_4 precipitation rate for nitriding ternary Fe-V-Si alloy specimens is much lower than that of a binary Fe-Si alloy specimen of similar Si content and nitrided at the same conditions. This is due to the extra enhancement of elastic strain energy upon precipitation of Si_3N_4 in a matrix already severely strained by the (semi-) coherent VN platelets and the action of the (semi-) coherent VN platelets as obstacles for movement of dislocations produced for plastic accommodation of the Si_3N_4 particle/ferrite-matrix volume misfit.
- Coarsening of first precipitated VN platelets, by an intermediate high temperature annealing treatment, results in incoherent VN particles and much lower VN-particle density and thus the ferrite matrix is relieved from coherency strain. As a result, continued nitriding leads to Si_3N_4 precipitation with a (much higher) rate similar to that for the corresponding binary Fe-Si alloy.

Acknowledgements

The authors thank Mr. Dipl.-Ing. (FH) P. Kress and Mr. W. Engelhardt for assistance with the nitriding experiments and Prof. Dr. van Aken to provide access to the TEM (all are with the Max Planck Institute for Intelligent Systems, Stuttgart).

Chapter 5

Coherency Strain and Precipitation Kinetics; Crystalline and Amorphous Nitride Formation in Ternary Fe-Ti/Cr/V-Si Alloys

Benjamin Schwarz, Paul J. Rossi, L. Straßberger, F. Jörg, Sai R. Meka, Ewald Bischoff, Ralf E. Schacherl and Eric J. Mittemeijer

Abstract

Specimens of iron-based binary Fe-Si alloy and ternary Fe-*Me*-Si alloys (with *Me* = Ti, Cr and V) were nitrided at 580 °C in a NH_3/H_2-gas mixture applying a nitriding potential of 0.1 $atm^{-1/2}$ until nitrogen saturation in the specimens was attained. In contrast with recent observations in other Fe-Me_1-Me_2 alloys no "mixed" (Me_1, Me_2) nitrides develop in Fe-*Me*-Si alloys upon nitriding: First all *Me* precipitates as *Me*N; thereafter all Si precipitates as Si_3N_4. The *Me*N precipitates as crystalline, finely dispersed, nanosized platelets, obeying a Baker-Nutting orientation relationship (OR) with respect to the ferrite matrix. The Si_3N_4 precipitates as cubically, amorphous particles; the incoherent (part of the) *Me*N/α-Fe interface acts as heterogeneous nucleation site for Si_3N_4. The Si_3N_4-precipitation rate was found to be strongly dependent on the degree of coherency of the first precipitating *Me*N. The different, even opposite, kinetic effects observed for the various Fe-*Me*-Si alloys could be ascribed to the different time dependences of the coherent → incoherent transitions of the *Me*N particles in the different Fe-*Me*-Si alloys.

5.1. Introduction

Gas nitriding is applied to ferritic iron-based alloys to improve their mechanical and chemical properties [1-3]. The dissociation of gaseous NH_3 on the surface of the component releases free nitrogen atoms which can be absorbed and diffuse inwardly via the octahedral interstitial-lattice sites of the ferrite matrix. Nitriding steels are usually alloyed with elements (e.g. Al, Ti, V and Cr [79-98]) having a strong affinity to nitrogen leading upon nitriding to the precipitation of nanosized alloying-element nitride particles in the ferrite matrix.

A parameter which characterizes the strength of the interaction of nitrogen and alloying element can be defined as the ratio of the energy gained upon nitride formation (i.e. chemical Gibbs energy) and the energy spent to form nitride precipitates in the ferrite matrix (i.e. interfacial and misfit-strain energies) [14, 99]. The larger the interaction parameter for a certain alloying element, the larger is the tendency for precipitation of the corresponding alloying-element nitride. On this basis two extremes of nitride-precipitation behavior can be distinguished [10]:

(i) *Strong interaction*: In the nitrided surface region (case) all alloying-element atoms precipitate more or less instantaneously as nitrides. Consequently a sharp case/core boundary migrates to larger depths with increasing nitriding time. In this case the nitriding kinetic is rate controlled, at constant temperature, by the diffusion of nitrogen through the nitrided case.

(ii) *Weak interaction*: Prior to the nitride precipitation, the iron matrix gets saturated with nitrogen throughout the specimen. Then, the nitride precipitation occurs at the same rate at each depth below the specimen surface. In this case the nitriding rate depends on the rate of precipitation kinetics that can be controlled by (a combination of) nucleation, growth and impingement mechanisms [11].

Experimental results obtained for the kinetics of precipitation, in *binary* iron-based alloys upon nitriding, of TiN [68, 100, 101] and VN [102-104] have shown that Ti and V exhibit a strong interaction with (inwardly diffusing) nitrogen. Cr shows a strong (for high Cr contents) to an intermediate (for relatively small Cr contents) interaction behavior [59, 105-107]. Weak interaction behavior is observed in the cases of Si [16, 17, 78] and Al [10, 108, 109], for nitride precipitation in a defect (dislocation) free/poor ferrite matrix.

Recently the nitriding behavior of ternary iron-based Fe-V-Si alloy was investigated for the first time [110]. It was shown that VN and Si_3N_4 precipitate not only separately but moreover successively: First all V precipitates as VN and thereafter Si_3N_4 precipitation takes place. Further, as compared to the precipitation rate of Si_3N_4 in binary Fe-Si alloy, the precipitation rate of Si_3N_4 in the ternary Fe-V-Si alloy was found to be much lower.

TiN, CrN and VN have the same cubic, rock-salt type crystal structure and precipitate in ferrite on the same habit plane ($\{001\}_{\alpha\text{-Fe}}$) and with the same orientation relationship (Baker-Nutting: $(100)_{\alpha\text{-Fe}} \parallel (100)_{MeN}, [010]_{\alpha\text{-Fe}} \parallel [011]_{MeN}$). However, as indicated by their lattice parameters, their (coherency-) strain fields induced by the misfitting nitride platelets in the ferrite matrix are of distinctively different magnitude: The coherency strains are highest for TiN, lower for CrN, and lowest for VN.

The present project is focused on investigation of the effect of the magnitude of the coherency strains, caused by prior precipitation of *Me*N (with *Me* = Ti, Cr and V) on the subsequently developing Si_3N_4 particles. Thereby, insight into mechanisms of precipitation in a matrix exhibiting locally fluctuating (coherency) strains is obtained.

5.2. Experimental procedures

5.2.1. Specimen preparation

The iron-based ternary Fe-*Me*-Si alloys and the binary Fe-Si alloy were produced by melting granules of Fe (purity 99.98 wt.%), Si (purity 99.999 wt.%), Ti (purity 99.999 wt.%), V (purity 99.9 wt.%) and Cr (purity 99.999 wt.%) under protective Ar atmosphere and cast to rods. The cast rods, with a length of 100 mm and a diameter of 10 mm, were ground to remove a possible surface-oxide layer. Afterwards the cast-rods were subjected to cold-rolling to prepare sheets with a thickness of approximately 1 mm. Specimens, with a rectangular shape and dimensions (15 × 10 × 1) mm, were cut from these sheets and subsequently ground, polished (final step with 1 µm diamond paste) and ultrasonically cleaned in ethanol. Next, the specimens were annealed, after having put them into a quartz tube filled with protective Ar gas, at 800 °C for 20 min to recrystallize the deformed microstructure. The recrystallized specimens were polished (1 µm diamond paste) again, to remove a possible surface-oxide layer formed during the recrystallization treatment and ultrasonically cleaned in ethanol.

The chemical composition of the Fe-Si and Fe-*Me*-Si specimens was determined by inductively coupled plasma optical emission spectroscopy (for the alloying-metal contents: Si, Ti, Cr and V), carrier gas hot extraction (for O and N) and combustion methods (for C and S). Results of the chemical analysis are shown in Table 10.

5.2.2. Nitriding

The Fe-2.0Si and Fe-*Me*-2.0Si alloy specimens were gas nitrided by suspending them, with a quartz fiber, in a vertical multizone quartz-tube furnace equipped with gas mass-flow (flow variation ±2.5 ml/min) and temperature (temperature variation ±1 °C) controllers (see Ref. [4] for detailed description of the nitriding facility). Nitriding experiments were performed at 580 °C

with a gas flux of NH_3 (purity 99.998 vol.%) adjusted to 45 ml/min and a gas flux of H_2 (purity 99.999 vol.%) adjusted to 455 ml/min. This set of gas fluxes corresponds to a nitriding potential of $r_N = 0.104\ \mathrm{atm}^{-1/2}$ (the nitriding potential is defined as $r_N = p(NH_3)/p(H_2)^{3/2}$, where p denotes partial pressure [3, 5]). Using this set of nitriding parameters, a 1 mm thick pure iron specimen is through nitrided after 20 hours [3]. For the employed nitriding potential at 580 °C iron nitrides (ε-Fe_3N_{1+x} or γ'-Fe_4N_{1-y}) cannot form upon nitriding pure iron [6], and no iron nitrides were found upon nitriding the Fe-2.0Si and Fe-*Me*-2.0Si alloys. The nitriding treatments were terminated by quenching the specimens into distilled water purged with N_2 gas (purging water with N_2 gas minimizes the O content dissolved in water).

Table 10: Alloying element contents and light element impurity contents in the binary iron-based Fe-Si alloy and the ternary Fe-*Me*-Si alloys prepared and employed in the present work.

alloy Fe-*Me*-2.0Si	*Me* (at.%)	Si (at.%)	O (µg/g)	N (µg/g)	C (µg/g)	S (µg/g)
Fe-2.0Si	-	1.99 ± 0.02	30	< 20	< 10	< 20
Fe-0.5Ti-2.0Si	0.47 ± 0.01	2.03 ± 0.02	50	< 10	< 20	< 20
Fe-0.2Ti-2.0Si	0.19 ± 0.01	2.01 ± 0.02	20	< 10	< 40	< 20
Fe-0.3V-2.0Si	0.29 ± 0.01	1.97 ± 0.01	60	< 20	< 10	< 20
Fe-2.0Cr-2.0Si	2.03 ± 0.02	1.94 ± 0.01	20	< 10	< 10	< 30

5.2.3. Weighing

Every specimen was weighed before and after nitriding with a comparator balance (Mettler XP56). For weight determination five such weighing measurements were carried out. From the

mean values and their standard deviations, before and after nitriding, the nitrogen uptake and its standard deviation were calculated. The latter standard deviation is smaller than the size of the data points in Figure 26.

5.2.4. X-ray diffraction

A PANalytic X´Pert multi-purpose diffractometer (MPD) employing Co-K_α radiation (λ = 1.7902 Å) and Bragg-Brentano geometry was used to record X-ray diffraction (XRD) patterns. This MPD is equipped with a graphite monochromator in the diffracted beam and an X´Celerator detector from PANalytic. The recorded diffractograms were analyzed by the software X´Pert Highscore and the occurring phases were identified from peak positions in the diffractograms using the data base from the International Center for Diffraction Data (ICDD) [12]. Recognizing that the specimens are homogeneously (through) nitrided after 20 h at 580 °C and $r_N = 0.104\ \mathrm{atm}^{-1/2}$ (see Section 5.2.2) no residual stress-depth profile occurs in the specimen. However, the misfit-strain fields surrounding the precipitated particles invoke a macroscopic, hydrostatic component of strain/stress (independent of depth) [111], leading to diffraction-peak shifts as a consequence of a change of the ferrite-lattice parameter. To trace the change of the ferrite-lattice parameter, the $200_{\alpha\text{-Fe}}$ peaks were fitted with an asymmetric (split) pseudo-Voigt function for both the $K_{\alpha 1}$ component and the $K_{\alpha 2}$ component [112], in the diffraction-angle range (70°– 85°) 2θ using the software Topas 3.0 from Bruker AXS. The instrumental offset for the utilized diffractometer was determined by making measurements on a pure iron specimen, prepared according to the procedure described in Section 5.2.1 (adopting the lattice parameter of pure iron of 2.8664 Å from Ref. [12]). From the thus obtained fit functions the peak position (and thereby the ferrite-lattice parameter) and the full width at half maximum (FWHM) of the $K_{\alpha 1}$

component were determined adopting 1/5 of the step size (0.033° 2θ) as the error in peak position. Thus the error in the ferrite-lattice parameter values in Table 11 is ± 0.0002 Å and the error for the lattice-parameter difference values in Table 11 is ± 0.0004 Å. The error in the FWHM values in Table 12 is taken as two times 1/5 of the step size (see above) and thus is ± 0.013° 2θ.

5.2.5. Transmission electron microscopy

Electron transparent foils were prepared from nitrided specimens at a depth below the surface of 100 µm (only in one case the depth was 500 µm as explicitly mentioned in the corresponding figure caption). To this end, discs with a diameter of 3 mm were cut out of the nitrided specimens. The thickness of the discs was reduced by grinding in such a way that the desired depth was in the middle of the remaining specimen; the final thinning involved either electropolishing or ion milling. In case of electropolishing the discs were (mechanically) polished and then electropolished (electrolyte: 85 vol.% acetic acid and 15 vol.% perchloric acid) with a Struers Tenupol-5 apparatus. In case of ion milling the discs were dimpled and then ion-milled using the apparatus Model 1010 from Fischione. A Philips CM 200 transmission electron microscope was used. The instrument is equipped with a Gatan CCD camera to record the bright-field (BF), dark-field (DF) images and selected area diffraction patterns (SADP). Ferrite-matrix diffraction spots, corresponding with known lattice spacings, d, were used for calibration of the camera constant of the microscope. In order to index diffraction spots in the SADPs, the software Digital Micrograph Diffpack from Gatan was used to determine the distances, R, of diffraction spots from the center in the SADPs and to calculate the corresponding d values. These d values were then compared with the lattice-parameter data provided by the ICDD data base [12].

5.3. Results and evaluation

5.3.1. Nitride-precipitation kinetics

Specimens of the ternary Fe-*Me*-2.0Si alloys (with *Me* = Ti, Cr and V) and the binary Fe-2.0Si alloy (see Table 10 for composition of the alloys) were nitrided for different times at 580 °C with $r_N = 0.104\ \text{atm}^{-1/2}$. The nitrogen uptakes as a function of nitriding time for these nitrided alloys are shown in Figure 26. The levels of nitrogen content expected, for precipitation of all *Me* as *Me*N, plus precipitation of all Si as Si_3N_4 and plus the establishment of the equilibrium-nitrogen solubility of an unstrained ferrite matrix, $[N]_\alpha^0$ (here 0.29 at.% N for the employed nitriding conditions [45]), for all the nitrided alloys have been indicated in Figure 26a with dashed lines. These levels of nitrogen content are called the "theoretical" nitrogen contents ($[N]^{theo} = [N]_{MeN} + [N]_{Si_3N_4} + [N]_\alpha^0$).

All alloy specimens were nitrided for sufficiently long time to reach the theoretical nitrogen content (at least; see what follows for uptake of "excess nitrogen"). Establishment of the theoretical nitrogen content for the different nitrided alloys is compatible with the development of separate *Me*N and Si_3N_4 precipitates, which is in agreement with the evidence from transmission electron microscopy investigation (cf. Section 5.3.2). The nitrogen taken up beyond the theoretical nitrogen level, as observed for especially the Fe-0.5/0.2Ti-2.0Si alloys, is called "excess nitrogen[G]".

The rate of increase of the nitrogen content in case of the ternary Fe-0.3V-2.0Si alloy is significantly smaller as that of the binary Fe-2.0Si alloy, the ternary Fe-2.0Cr-2.0Si and

[G] Excess nitrogen denotes the part of the nitrogen uptake (after saturation) above the expected for only precipitation of *Me*N and realization of the nitrogen equilibrium solubility of unstrained ferrite. This extra nitrogen can be (i) adsorbed at the *Me*N/α-Fe interface, (ii) dissolved in the ferrite matrix due to the strain field surrounding (semi-) coherent *Me*N precipitates and (iii) trapped at dislocations[14, 57].

Fe-0.2/0.5Ti-2.0Si alloys: For example, the nitriding times needed to attain a constant, saturation level of nitrogen are 650 h for the binary Fe-2.0Si alloy, 200 h/520 h for the ternary Fe-0.5/0.2Ti-2.0Si alloys, 500 h for the ternary Fe-2.0Cr-2.0Si alloy and 1500 h for the ternary Fe-0.3V-2.0Si alloy (see Figure 26a).

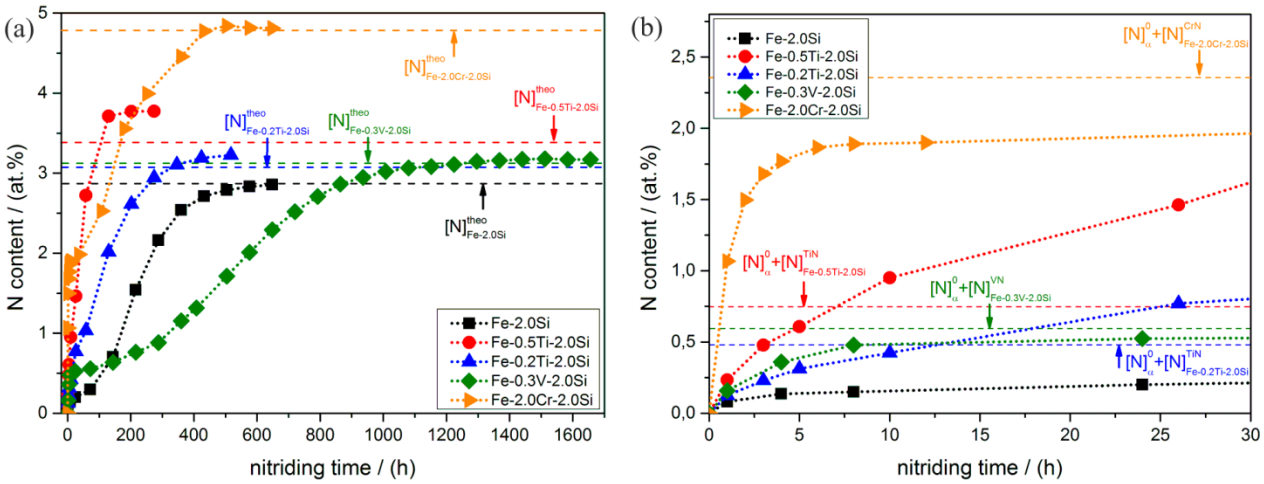

Figure 26: **a)** Nitrogen content as a function of nitriding time for the binary Fe-2.0Si alloy and the ternary Fe-*Me*-2.0Si alloy (with *Me* = Ti, Cr and V) specimens nitrided at 580 °C with $r_N = 0.104\ \mathrm{atm}^{-1/2}$. The "theoretical nitrogen contents" as indicated with dashed lines, pertain to (pure) ferrite saturation with nitrogen and all alloying-element atoms precipitated as stoichiometric *Me*N and Si_3N_4. **b)** For nitriding times shorter than 30 h the nitrogen-content curves attain, except of the nitrided ternary Fe-0.2/0.5Ti-2.0Si alloy specimens, a practically constant nitrogen level. The dashed lines indicate the nitrogen levels in nitrided Fe-*Me*-2.0Si alloys for (pure) ferrite saturation ($[N]_\alpha^0$ = 0.29 at.%; according to Ref. [45]) and all *Me* (= Ti, Cr and V) precipitated as stoichiometric *Me*N. The dotted lines in a) and b) connect the experimentally obtained data points.

For nitriding times less than about 30 h, and except for the nitrided ternary Fe-0.5/0.2Ti-2.0Si alloys, all other alloys show (more or less) a plateau in the nitrogen content vs. time curves (Figure 26b). The levels of nitrogen content expected for equilibrium saturation of the ferrite matrix with nitrogen, and with all Ti precipitated as TiN (for the Fe-Ti-Si alloys), with all Cr precipitated as CrN (for the Fe-Cr-Si alloy) and with all V precipitated as VN (for the Fe-V-Si alloy), have been indicated in Figure 26b with dashed horizontal lines. These levels of nitrogen content are called the "normal nitrogen content upon *Me*N development" ($[N]_{MeN} + [N]_{\alpha}^{0}$).

The initial (at nitriding time <30 h) plateau level of nitrogen content of the ternary Fe-0.3V-2.0Si alloy specimen is nearly at the expected $[N]_{MeN} + [N]_{\alpha}^{0}$ level (Figure 26b), suggesting that at this stage, all V has precipitated as stoichiometric VN and that no significant precipitation of Si_3N_4 has occurred. The initial plateau level of nitrogen content of the ternary Fe-2.0Cr-2.0Si alloy specimen is lower than the expected $[N]_{MeN} + [N]_{\alpha}^{0}$ level. This discrepancy, despite the expectation of an even higher nitrogen content due to precipitation of a small amount of Si_3N_4 at this stage (as revealed by TEM; cf. Section 5.3.2) and excess nitrogen uptake, which is expected in connection with precipitated CrN [70, 113] can be attributed to dissolved Si in ferrite lowering the nitrogen solubility [62].

Absence of an initial plateau for the nitrided Fe-Ti-Si alloys suggests overlapping in time of the TiN precipitation and Si_3N_4 precipitation processes, i.e., some part of Si precipitates, as Si_3N_4, simultaneously with the precipitation of Ti as TiN (see what follows and Section 5.3.2, where supporting TEM evidence is presented).

In case of the nitrided binary Fe-2.0Si alloy specimen the initial plateau level of nitrogen content is 0.20 at.%. This value is smaller than the expected nitrogen solubility of pure iron (0.29 at.%; according to Ref. [45]) for the same nitriding conditions, suggesting that, at this stage of nitriding, no significant Si_3N_4 precipitation has taken place. The slightly lower nitrogen level

in the Fe-2.0Si alloy as compared to the expected nitrogen solubility of pure iron can be attributed to the presence of dissolved Si in ferrite that lowers (significantly) the nitrogen solubility [62].

The dependence of nitrogen content on nitriding time for the different alloys can be fitted well (for nitriding times beyond the initial stage, i.e. for nitriding times >30 h; see above) with a sigmoidal Boltzmann function (see Figure 27a). The derivative of these functions with respect to nitriding time provides the nitriding rates as a function of nitriding time (Figure 27b).

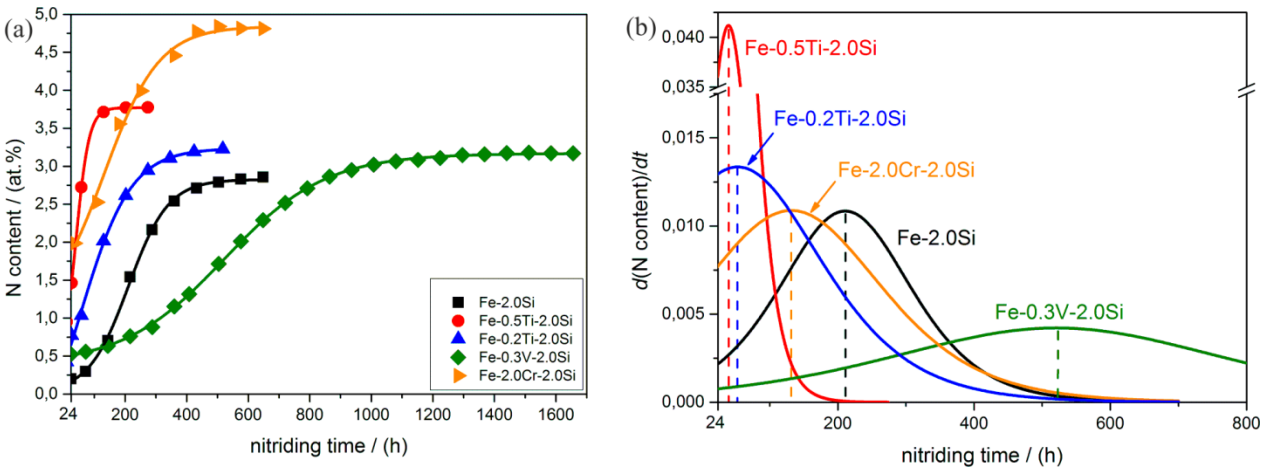

Figure 27: **a)** Nitrogen content as a function of nitriding time for binary Fe-2.0Si alloy and ternary Fe-*Me*-2.0Si alloy (with *Me* = Ti, Cr and V) specimens nitrided at 580 °C with $r_N = 0.104\ \mathrm{atm}^{-1/2}$. The experimentally obtained data points were numerically fitted with a sigmoidal Boltzmann function (continuous lines). **b)** The corresponding nitrogen-uptake rates as a function of nitriding time (derivatives of the continuous lines in a)).

Evidently, the highest maximum-nitriding rate occurs for the ternary Fe-0.5Ti-2.0Si and Fe-0.2Ti-2.0Si alloys, followed by the ternary Fe-2.0Cr-2.0Si alloy, the binary Fe-2.0Si alloy and the ternary Fe-0.3V-2.0Si alloy, in that order. The kinetic data show that, as compared to the

Si_3N_4-precipitation rate in the binary Fe-2.0Si alloy, pronounced acceleration of the Si_3N_4-precipitation rate occurs in the ternary Fe-0.2/0.5Ti-2.0Si alloys, whereas a strong deceleration is observed in the ternary Fe-0.3V-2.0Si alloy. In this respect the Fe-2.0Cr-2.0Si alloy takes an intermediate position.

5.3.2. Structure and morphology of precipitated nitrides

TEM investigations were performed to reveal the structure and morphology of precipitated nitrides (i) after relatively short nitriding times (but mostly after 24 h, because this nitriding time is sufficient to nitride a 1 mm thick specimens homogenously; cf. Section 5.2.2.) and (ii) after the nitriding time at which (in addition to *Me*N) nearly all Si_3N_4 has precipitated.

TEM images recorded from the ternary Fe-0.2Ti-2.0Si alloy specimen, from the ternary Fe-2.0Cr-2.0Si alloy specimen and from the ternary Fe-0.3V-2.0Si alloy specimen after short time nitriding are shown in Figure 28. In these nitrided alloys, finely-dispersed, nano-sized *Me*N precipitates have developed. These precipitates exhibit a platelet-like morphology (thickness of only 1-2 atomic layers) with a length around 4 nm in case of TiN, a length around 23 nm in case of CrN and a length around 5 nm case of VN. The (semi-) coherency of these nitride platelets with the ferrite matrix is illustrated by the coffee-bean like contrast [72] surrounding the platelets in the BF images (cf. magnified insets in Figure 28a1, 28b1 and 28c). The corresponding SADPs, recorded in $[001]_{\alpha\text{-Fe}}$-zone axis, show diffraction spots from the ferrite matrix and in case of the Fe-2.0Cr-2.0Si and Fe-0.3V-2.0Si alloys streaks of intensity along $[100]_{\alpha\text{-Fe}}$ and $[010]_{\alpha\text{-Fe}}$ directions with intensity maxima at positions corresponding to diffraction spots of CrN/VN of rock-salt crystal structure type oriented in Baker-Nutting orientation relationship ($(100)_{\alpha\text{-Fe}} \parallel (100)_{MeN}, [010]_{\alpha\text{-Fe}} \parallel [011]_{MeN}$) [13] with respect to the ferrite matrix. These streaks of

intensities are a consequence of strain broadening due to the development of (semi-) coherent nitride platelets on $\{100\}_{\alpha\text{-Fe}}$-habit planes (the maximal misfit strain occurs in $\langle 100 \rangle_{\alpha\text{-Fe}}$ directions perpendicular to the nitride platelets) and the very thin nature of the *Me*N platelets. Note that these streaks of intensity are less well observable in case of the Fe-0.2Ti-2.0Si alloy and are most pronounced in case of the Fe-0.3V-2.0Si alloy. Both the Fe-0.2Ti-2.0Si and the Fe-2.0Cr-2.0Si alloy specimens additionally show, in contrast with the Fe-0.3V-2.0Si alloy specimen, relatively small cubically shaped precipitate particles (Figure 28a2 and 28b2); small as compared to their size after longer nitriding times (see Figure 29, 30 and 31). These observations suggest that these particles are amorphous Si_3N_4 (for direct evidence see discussion of Figure 29, 30 and 31), as reported before for nitrided binary Fe-Si (see Refs. [16-18]), an effect likely due to control by interface thermodynamics [31, 114].

TEM images recorded from a Fe-0.5Ti-2.0Si alloy specimen nitrided for 77 h (after this nitriding time all Ti and nearly all Si have precipitated as TiN and Si_3N_4, respectively; cf. Figure 27a) are shown in Figure 29. The BF image (Figure 29a) reveals two cubical Si_3N_4 precipitates which remained upon electropolishing at the edge of the TEM foil due to selective dissolution of the ferrite matrix. The edge length of the cubes is approximately 30 nm and the cube faces are parallel to $\{100\}_{\alpha\text{-Fe}}$-lattice planes. The corresponding SADP (Figure 29b), recorded in $[001]_{\alpha\text{-Fe}}$-zone axis, shows diffraction spots from the ferrite matrix together with an extremely weak streaking in $[100]_{\alpha\text{-Fe}}$ and $[010]_{\alpha\text{-Fe}}$ directions. A DF image (Figure 29c) recorded using the weak intensity of a streak at the location of the expected 002_{TiN}-diffraction spot (indicated with a circle in the SADP in Figure 29b) shows, by bright appearance, TiN platelets in both the ferrite matrix and the amorphous Si_3N_4 particles.

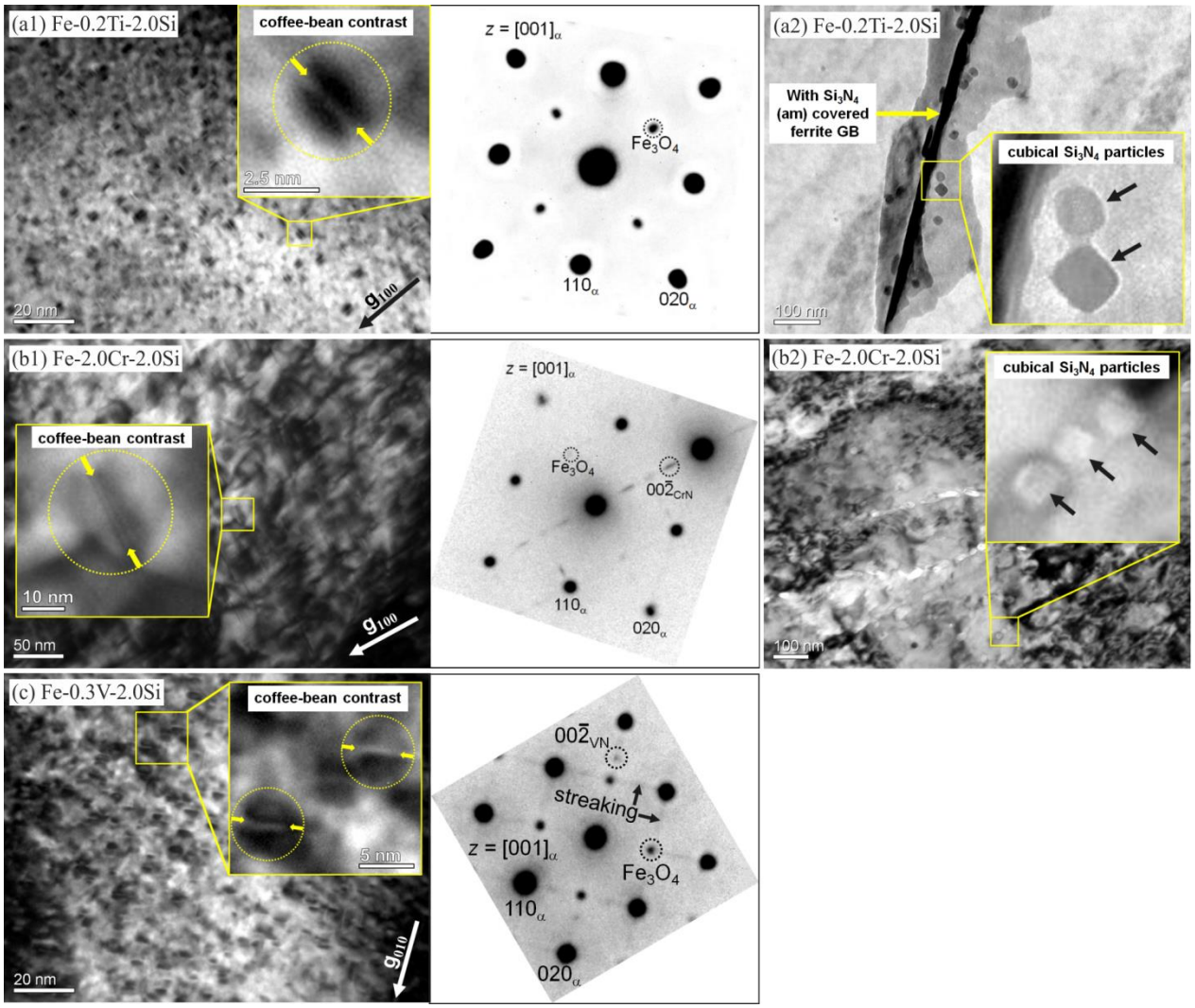

Figure 28: TEM images recorded from ternary Fe-*Me*-Si alloy (with *Me* = Ti, Cr and V) specimens after nitriding (580 °C, $r_N = 0.104\ \mathrm{atm}^{-1/2}$) for 10 h in case of the Fe-0.2Ti-2.0Si alloy and for 24 h in case of the Fe-2.0Cr-2.0Si and Fe-0.3V-2.0Si alloys. Nano-sized *Me*N platelets developed (BF images **a1)**, **b1)** and **c)**). The SADPs show diffraction spots belonging to the ferrite matrix, iron oxide and in case of the Fe-2.0Cr-2.0Si and Fe-0.3V-2.0Si alloy specimens streaking along $[100]_{\alpha\text{-Fe}}$ and $[010]_{\alpha\text{-Fe}}$ directions. The BF images of the Fe-0.2Ti-2.0Si and the Fe-2.0Cr-2.0Si alloy specimen show, in addition to TiN/CrN platelets, cubical Si_3N_4 particles (BF images **a2)** and **b2)**) in the ferrite matrix. The Fe-0.2Ti-2.0Si alloy specimen (b2) shows in addition a ferrite-grain boundary covered with amorphous Si_3N_4.

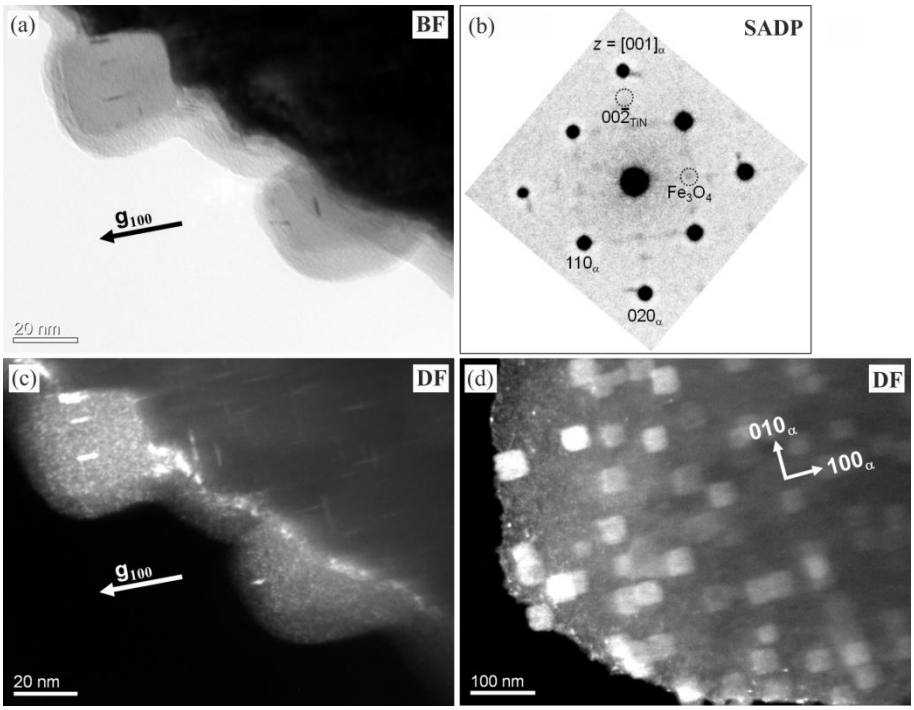

Figure 29: TEM images recorded from the ternary Fe-0.5Ti-2.0Si alloy specimen after nitriding (580 °C, $r_N = 0.104\ \mathrm{atm}^{-1/2}$) for 77 h (after this nitriding time all TiN and nearly all Si_3N_4 have precipitated). **a)** BF image showing two cubical Si_3N_4 particles at the edge of the TEM foil; tiny (TiN) platelets can be discerned within these Si_3N_4 particles. **b)** The corresponding SADP with diffraction spots of the ferrite matrix (α), iron oxide and very weak streaks of intensities along $[100]_{\alpha\text{-Fe}}$ and $[010]_{\alpha\text{-Fe}}$ directions. **c)** DF image recorded using the (weak) intensity of a streak (location of the aperture at the position of the possible $00\bar{2}_{TiN}$ -diffraction spot) has been indicated with a dashed circle in the SADP) exhibits crystalline (TiN) platelets with a pronounced bright contrast in the ferrite matrix and within the cubical Si_3N_4 particles. The cubical Si_3N_4 particles appear also brighter than the surrounding matrix due to the diffuse intensity resulting from electron scattering by the amorphous Si_3N_4 particles. **d)** DF image, recorded using the diffuse intensity, showing the Si_3N_4 particles by bright contrast with the matrix. Note the high Si_3N_4-particle density at this practically end stage of the precipitation process.

In the DF image the cubical Si_3N_4 particles also appear with bright contrast indicating their amorphous nature: the diffuse halo of intensity generated by electron scattering by the amorphous Si_3N_4 particles at the location of 002_{TiN}-diffraction spot implies illumination of both the amorphous particles and crystalline TiN platelets in the DF image (see Figure 29c); the DF image formed by placing the SADP aperture at a location of diffuse intensity, where no TiN spot occurs, leads to bright appearance of only the amorphous Si_3N_4 particles in the corresponding DF image (Figure 29d).

Both the presence of much smaller TiN platelets (length around 4 nm) within relatively large Si_3N_4 particles and the recognition that these TiN platelets have the same orientation as the TiN particles in the ferrite matrix suggest that the TiN platelets within the Si_3N_4 particles have precipitated first in the ferrite matrix, in accordance with a Baker-Nutting OR, and were incorporated later into (overgrown by) growing Si_3N_4 particles.

The Fe-2.0Cr-2.0Si alloy specimen nitrided for 648 h (at this stage all Cr and all Si have precipitated as CrN and Si_3N_4, respectively) exhibits cubical Si_3N_4 particles (edge length around 40 nm) which incorporate parts of significantly coarsened CrN platelets (platelet length up to 80 nm; cf. Figure 30a). Due to the significant coarsening of the CrN precipitates diffraction spots belonging to CrN are (now) visible in the corresponding SADP (see the SADP in Figure 30b) and compare it with that in Figure 28b1. The DF image shown in Figure 30c was recorded using the diffuse intensity around the primary electron beam and a weak diffraction spot of CrN. Similar to the observations for the Fe-Ti-Si alloy, the Si_3N_4 particles and CrN platelets show a bright contrast and thus the Si_3N_4 particles are amorphous. The BF images suggest that small (as compared to the CrN platelet length; see above) Si_3N_4 particles heterogeneously nucleate at the incoherent CrN/α-Fe interface perpendicular to the platelet faces (Figure 30d) and grow along the (initially) coherent CrN/α-Fe interface of the platelet faces with the matrix (Figure 30e).

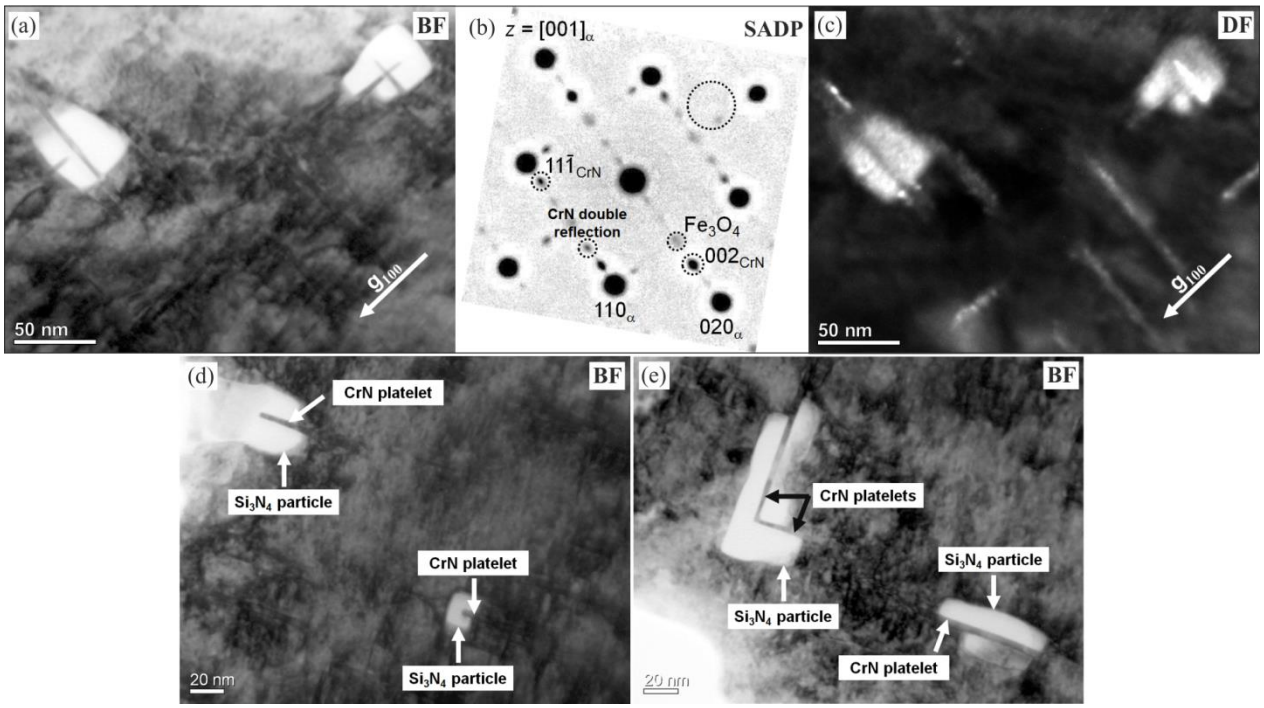

Figure 30: TEM images recorded from the ternary Fe-2.0Cr-2.0Si alloy specimen after nitriding at 580 °C with $r_N = 0.104\ atm^{-1/2}$ for 648 h (after this nitriding time all CrN and all Si_3N_4 have precipitated). In contrast with the electron transparent foils pertaining to the TEM analysis shown in Figure 28, 29 and 31, this TEM foil was prepared from the core region (around 500 µm below the surface). **a)** The BF image shows two cubical Si_3N_4 particles intersected by significantly coarsened (as compared to the initial stage: see Figure 28b1) CrN precipitates. **b)** The corresponding SADP (with $[001]_{\alpha\text{-}Fe}$ -zone axis) shows diffraction spots of the ferrite matrix (α), iron oxide (see caption of Figure 28) and CrN of rock-salt crystal-structure type, satisfying a Baker-Nutting OR with respect to the ferritic matrix. **c)** DF image, recorded using the diffuse intensity and a weak diffraction spot of CrN (see the large dashed circle in b)), shows Si_3N_4 particles and CrN platelets with a pronounced bright contrast. **d)** BF image showing two Si_3N_4 particles apparently nucleated at the tip of coarsened CrN platelets and **e)** BF image showing Si_3N_4 particles grown along the faces of CrN platelets.

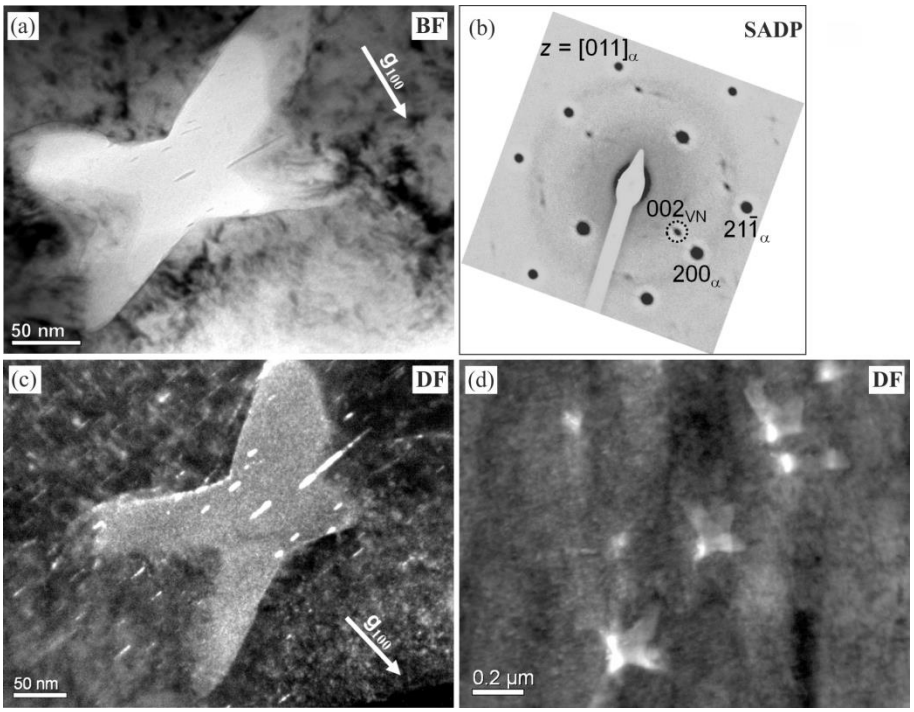

Figure 31: TEM images recorded from the ternary Fe-0.3V-2.0Si alloy specimen after nitriding at 580 °C with $r_N = 0.104\ \mathrm{atm}^{-1/2}$ for 1656 h (after this nitriding time all VN and all Si_3N_4 have precipitated). **a)** BF image showing a cut through an octapod-shaped Si_3N_4 precipitate, with cross-over distance from tip to tip of approximately 350 nm; note the VN platelets within the Si_3N_4 particle. **b)** The corresponding SADP ($[011]_{\alpha\text{-Fe}}$-zone axis) shows diffraction spots belonging to the ferrite matrix and VN and a diffuse intensity ("halo") around the primary electron beam due to electron scattering by the amorphous Si_3N_4 precipitates. **c)** DF image, recorded using the intensity of the 002_{VN}-diffraction spot, exhibiting crystalline (VN) platelets with a pronounced bright contrast in the ferrite matrix and within the cubical Si_3N_4 particle. The cubical Si_3N_4 particles appear also brighter than the surrounding matrix due to the diffuse intensity resulting from electron scattering by the amorphous Si_3N_4 particle. **d)** DF image, recorded using the diffuse intensity, showing multiple illuminated Si_3N_4 particles by bright contrast with the matrix.

Nitriding of a Fe-0.3V-2.0Si alloy specimen for 1656 h leads to coarsening of crystalline VN precipitates and to the development of large amorphous Si_3N_4 particles with a presumably octopod-shape[H] (Figure 31). Further, crystalline VN platelets have become incorporated, by overgrowth, into the amorphous and much larger Si_3N_4 particles. Corresponding SADP (Figure 31b) shows diffraction spots belonging to the ferrite matrix and to VN. The DF image shown in Figure 31c was recorded using the intensity of a VN-diffraction spot and as a consequence the VN precipitates show a distinctively bright contrast. Note the similar orientation of VN platelets in the Si_3N_4 particle and in the matrix (see above discussion for the Fe-0.5Ti-2.0Si alloy). The DF image recorded by placing the SADP aperture at a location of diffuse intensity, where no VN spot occurs, leads to bright appearance of the octapod shaped amorphous Si_3N_4 particles (Figure 31d).

5.3.3. Ferrite-lattice parameter changes as a function of nitriding time; macrostrain and microstrain

The diffractograms recorded from the surface of the nitrided specimens show only reflections from the ferrite matrix. A comparison of the $200_{\alpha\text{-Fe}}$-reflections of the binary Fe-2.0Si alloy and the ternary Fe-*Me*-2.0Si alloys, before nitriding (stage 1), and after nitriding for times (i) at which the ferrite matrix is saturated with dissolved nitrogen and all *Me*, in case of the Fe-*Me*-2.0Si alloys, has precipitated as *Me*N (at around 24 h – 26 h; stage 2), and (ii) at which, additionally

[H] A change of morphology happens upon Si_3N_4 precipitation in the long time nitrided Fe-0.3V-2.0Si alloy specimen. At the beginning (216 h) of Si_3N_4 precipitation the Si_3N_4 particles are cubical whereas after completion of the precipitation process (1656 h) the particles have become octapod-shaped [110]. Comparably long nitriding/ageing times were not applied to the other alloy specimens of this work. A similar change in Si_3N_4 precipitate morphology upon nitriding a binary Fe-4.5Si alloy for long times at 650 °C (923 K) was observed and discussed in Ref. [19].

(for the Fe-*Me*-2.0Si alloys), all Si has precipitated as Si_3N_4 (stage 3), is provided by Figure 32. Again (cf. Section 5.2.4), note that, for the homogenously nitrided specimens considered here, no (macro)stress-depth profiles occur, thereby allowing an interpretation of ferrite-lattice parameter changes as caused only by possible changes of solute contents and (homogeneous) hydrostatic (macro)stress. Thus, upon nitriding, ferrite-peak shifts pertaining to the times/conditions (i) and (ii), indicated above, can be due to a change of the ferrite-lattice parameter associated with (a) the change in the contents of interstitially dissolved nitrogen and substitutionally dissolved *Me* and Si in the ferrite matrix, upon precipitation of internal nitrides, and (b) the establishment of a macroscopic, tensile, hydrostatic component of stress as a consequence of the elastic accommodation of the *Me*N-particle/α-Fe matrix misfit; such change of the matrix-lattice parameter upon nitriding was demonstrated for the first time for precipitation of Si in supersaturated Al-Si alloys in Ref. [111]. On this basis ((a) + (b)) the measured ferrite-lattice parameter change as a function of nitriding time is interpreted in the following as reflecting the different stages of nitride precipitation.

The ferrite-lattice parameters of unnitrided (stage 1), 24 h – 26 h nitrided (stage 2) and homogeneously through nitrided (stage 3) specimens of the Fe-2.0Si alloy and the Fe-*Me*-2.0Si alloys were determined, applying Bragg´s law, from the measured positions of $200_{\alpha\text{-Fe}}$-ferrite (XRD) $K_{\alpha 1}$ peaks, corrected for the instrumental offset (cf. Section II, D). The measured changes in the lattice parameter of ferrite for a particular stage of nitriding, with respect to its value in the preceding stage, are presented in Table II (the last two columns). The measured lattice-parameter values of the unnitrided alloys and the corresponding values as predicted by using the lattice-parameter data for the different *binary* iron-based alloys as presented in Ref. [115], by interpolation adopting “Végard´s law” even in the present case of *ternary* instead of binary iron-based alloys, are also presented in Table 11.

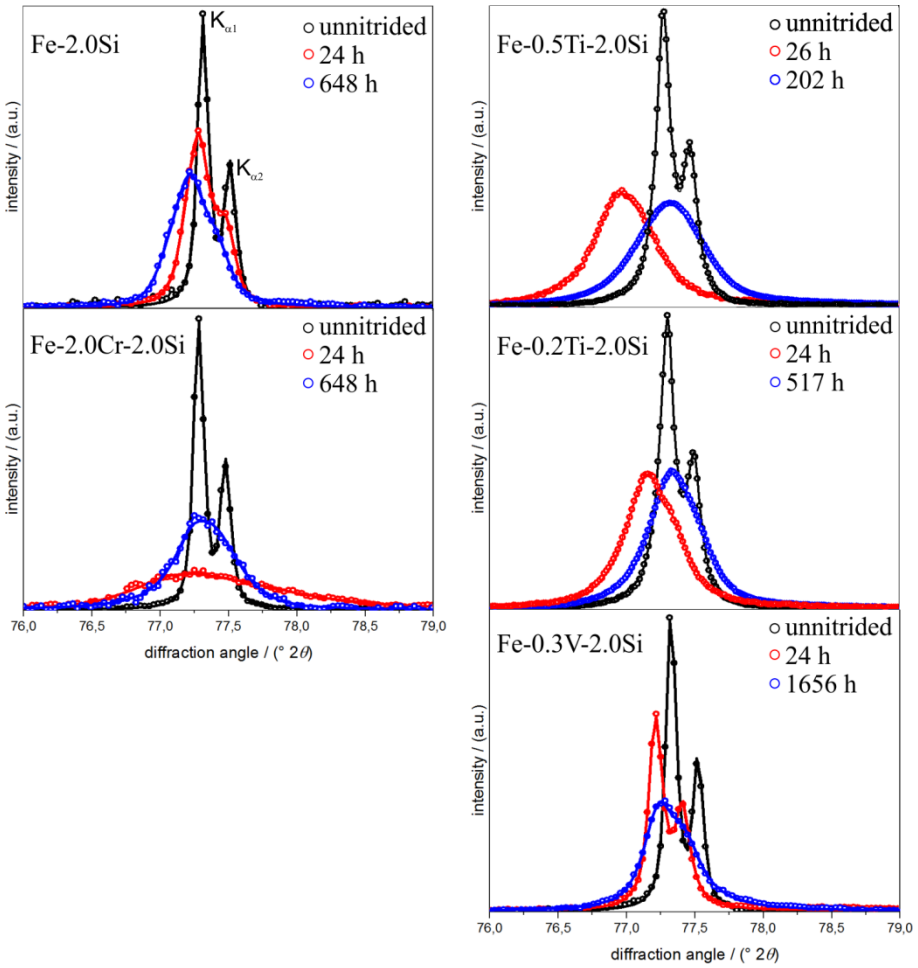

Figure 32: X-ray diffractograms (normalized with respect to integrated intensity) in the diffraction-angle range of the $200_{\alpha\text{-Fe}}$ reflection recorded from the surface of the binary Fe-2.0Si alloy specimen and the ternary Fe-*Me*-Si alloy (with *Me* = Ti, Cr and V) specimens before nitriding and after nitriding at 580 °C with a nitriding potential of $r_N = 0.104\ \text{atm}^{-1/2}$ for times (i) after the 1 mm thick specimens have been (homogenously) through nitrided (cf. Section 5.2.2) and (ii) after in addition to *Me*N, practically all Si_3N_4 has precipitated. In the diffractograms only reflections belonging to ferrite are observed. The intensity data (circles) were fitted with asymmetrical (split) pseudo-Voigt functions for the $K_{\alpha 1}$ and $K_{\alpha 2}$ components (continuous lines; cf. Section 5.2.4).

A fair agreement between measured and predicted lattice parameter values of the unnitrided Fe-*Me*-Si alloys occurs (Table 11; first two columns), recognizing the experimental accuracy (about ± 0.0002 Å; cf. Section II, D). Moreover, the possible discrepancies may be ascribed to the non-validated assumption of a Végard-like dependence of the lattice parameter on content of solutes even in the present case of ternary alloys.

The small, positive change of the ferrite-lattice parameter in case of the binary Fe-2.0Si alloy after nitriding for 24 h (stage 2) is in agreement with the lattice parameter increase expected due to the dissolution of 0.2 at.% of nitrogen in ferrite (see Section 5.3.1; according to Ref. [116], an increase of 0.0014 Å of the lattice parameter of ferrite is expected upon dissolution of 0.2 at.% nitrogen). This suggests that at this stage all Si remains in dissolved state, i.e. no Si_3N_4 precipitation occurs (cf. Section. 5.3.1). A further increase of the ferrite-lattice parameter occurs in stage 3, which is compatible with the expectation that upon precipitation of Si, in stage 3, the lattice parameter of the ferrite matrix increases further.[17, 62] A depletion of 2 at.% of Si solute in ferrite results in an increase of the ferrite-lattice parameter of the order 0.0013 Å [115]. Further, the removal of 2 at.% Si from the ferrite matrix leads to an increased equilibrium nitrogen solubility (plus 0.09 at.% nitrogen; see Section 5.3.1) and thus to a further increase of the ferrite-lattice parameter of 0.0006 Å [116]. The good agreement of the thus predicted, total (0.0019 Å) and measured (0.0022 Å) lattice parameter changes for stage 3 is compatible with the absence of any possible hydrostatic tensile misfit stress due to misfitting Si_3N_4 precipitates: As indicated in Section 5.3.1, the precipitation of Si_3N_4 in a ferritic matrix is associated with such a large volume misfit (>100%) that it is entirely accommodated plastically by dislocation generation (as shown in Ref. [19]).

Considering stage 2 and as compared to the binary Fe-Si alloy, for all ternary Fe-*Me*-Si alloys a much larger, positive change in the ferrite lattice parameter occurs (Table 11). Note that the

removal of dissolved *Me* from the solid solution, upon *Me*N development, leads to a decrease in the ferrite lattice parameter (opposite to an increase as induced by Si depletion (see above discussion), which depletion does not occur in stage 2 (see Sections 5.3.1 and 5.3.2). Hence, the occurrence of the large, positive change in the lattice parameter in stage 2 for the Fe-*Me*-Si alloys is direct evidence for the development of a hydrostatic tensile misfit strain, as expected according to Ref. [111], upon elastic accommodation of the *Me*N-particle/α-Fe volume misfit.

Table 11: Predicted and measured ferrite-lattice parameters of the binary Fe-2.0Si alloy and the ternary Fe-*Me*-2.0Si alloys in the unnitrided state (stage 1). Measured change of the ferrite-lattice parameter with respect to the preceding stage after all *Me* has precipitated as *Me*N (stage 2) and after also all Si has precipitated as Si_3N_4 additionally to *Me*N (stage 3). The error in the measured lattice-parameter values is about ± 0.0002 Å and the error for the lattice-parameter difference values is about ± 0.0004 Å (see Section 5.2.4).

	stage 1 unnitrided lattice parameter, a		stage 2 nitrided (24 h – 26 h) $\Delta a = a_{\text{stage 2}} - a_{\text{unnitrided}}$	stage 3 nitrided (end stage) $\Delta a = a_{\text{stage 3}} - a_{\text{stage 2}}$
alloy Fe-*Me*-Si	calculated (Å)	measured (Å)	measured (Å)	measured (Å)
Fe-2.0Si	2.8651	2.8654	0.0009	0.0022
Fe-0.2Ti-2.0Si	2.8653	2.8657	0.0048	-0.0053
Fe-0.5Ti-2.0Si	2.8655	2.8665	0.0108	-0.0117
Fe-0.3V-2.0Si	2.8655	2.8648	0.0037	-0.0008
Fe-2.0Cr-2.0Si	2.8662	2.8664	0.0057	-0.0051

Considering stage 3, and as compared to stage 2, for all ternary Fe-*Me*-Si alloys an opposite (i.e. negative) change of the ferrite-lattice parameter occurs. Upon only precipitation of Si in stage 3 in the Fe-*Me*-Si alloys the ferrite-lattice parameter increases (see above). Hence, the occurrence of an in absolute sense much larger and negative ferrite-lattice parameter change for the Fe-*Me*-Si alloys in stage 3 is ascribed to the relaxation of the tensile hydrostatic component of misfit stress, induced in stage 2, upon the continued nitriding (aging) in stage 3. This is compatible with the observations reported in Sections 5.3.1 and 5.3.2: In stage 3 the *Me*N particles, which (largely) all developed in stage 2, grow and become incoherent with the surrounding ferrite matrix, leading to the relaxation of the misfit stresses.

As compared to VN, TiN exhibits a larger misfit with the ferrite matrix. With a view to the above discussion, then a larger hydrostatic, tensile macrostress in the ferrite matrix is expected, leading, for the same amount of alloying element, to a larger increase of the ferrite-lattice parameter. This expectation is compatible with the experimental results for the lattice parameter change after 24 h – 26 h of nitriding (cf. results for Fe-V-Si and Fe-Ti-Si for stage 2 in Table 11). Also note that the increase of the ferrite-lattice parameter is larger for the alloy with the higher Ti content, which is in agreement with the given interpretation. In view of the misfit of TiN with the ferrite matrix being larger than for VN, it can be expected that upon continued nitriding (aging), at identical conditions, TiN will loose coherency with the ferrite matrix sooner than VN. Indeed, whereas for the Fe-V-Si alloy in stage 3, i.e. after all Si_3N_4 has precipitated, the relaxation of the (coherency) macrostrain in the ferrite matrix has not been completed, for the Fe-Ti-Si alloys, this relaxation appears to be fully realized (cf. corresponding results in the last two columns of Table 11).

As compared to VN and TiN, CrN takes an intermediate position regarding its misfit with the ferrite matrix. An in this sense modified discussion as above can be given for the macrostrain

changes (ferrite-lattice parameter changes) for the Fe-Cr-Si alloy. Doing so, it should be recognized that the amount of alloying element *Me* is much larger in the Fe-Cr-Si alloy than in the Fe-V-Si and Fe-Ti-Si alloys.

The diffraction-line broadening data support the above interpretation: The FWHM of the $200_{\alpha\text{-Fe}}\text{-}K_{\alpha 1}$ peak increases for all Fe-*Me*-Si alloys upon nitriding for 24 h – 26 h (stage 2) and the increase is the more pronounced the larger the misfit between *Me*N and the ferrite matrix and the higher the *Me* content (Table 12). These observations strongly suggest that the nitriding induced diffraction-line broadening at this stage 2 reflects the development of microstrain (i.e. localized variation in strain due to the misfit-strain fields surrounding the (semi-)coherent *Me*N precipitates as reported in Ref. [71].

Table 12: FWHM (in ° 2θ) of the $200_{\alpha\text{-Fe}}$-ferrite peak ($K_{\alpha 1}$ component) of the binary Fe-2.0Si alloy and the ternary Fe-*Me*-2.0Si alloys in the unnitrided state (stage 1), after all *Me* has precipitated as *Me*N (stage 2) and after also all Si has precipitated as Si_3N_4 additionally to *Me*N (stage 3). The error in the FWHM values is ± 0.013° 2θ (see Section 5.2.4).

	stage 1	stage 2	stage 3
alloy	unnitrided	nitrided (24 h – 26 h)	nitrided (end stage)
Fe-*Me*-Si	(° 2θ)	(° 2θ)	(° 2θ)
Fe-2.0Si	0.050	0.100	0.075
Fe-0.2Ti-2.0Si	0.064	0.173	0.119
Fe-0.5Ti-2.0Si	0.065	0.211	0.138
Fe-0.3V-2.0Si	0.047	0.063	0.055
Fe-2.0Cr-2.0Si	0.046	0.584	0.315

The semi-coherent *Me*N (with *Me* = Ti, Cr and V) platelets developing along $\{100\}_{\alpha}$-lattice planes of the matrix, according to the Baker-Nutting OR, induce tensile and compressive misfit stresses parallel and perpendicular to the faces of the platelets, respectively. Thereby a locally varying, tetragonal distortion of the platelet surrounding ferrite matrix occurs, which contributes to a large extent to the (asymmetry of the) diffraction-line broadening especially observed for the $200_{\alpha\text{-Fe}}$ reflex [71]. Upon continued nitriding until nitrogen saturation, i.e. Si_3N_4 has precipitated in addition to *Me*N (stage 3), the FWHM of the $200_{\alpha\text{-Fe}}$ peak has decreased as compared to the FWHM after 24 h of nitriding (stage 2) due to relaxation of the *Me*N/α-Fe misfit, relatively most pronouncedly for the Fe-Ti-Si alloys and least for the Fe-V-Si alloy, which is fully compatible with the above interpretation of the (average) ferrite-lattice parameter change.

5.4. General discussion

5.4.1. Separate precipitations of binary nitrides, *Me*N and Si_3N_4

In the nitrided ternary Fe-*Me*-Si (with *Me* = Ti, Cr and V) alloys precipitation of separate binary, crystalline cubic rock-salt crystal-structure type *Me*-nitride (*Me*N) and binary, amorphous Si-nitride (Si_3N_4) occurs, as indicated by the mass-uptake and TEM data (Sections 5.3.1 and 5.3.2). This contrasts with the nitriding behavior of other ternary iron-based alloys: In Fe-Cr-Al and Fe-Cr-Ti alloys mixed ternary nitrides, $Me_{a(1-x)}Me_{b(x)}N$, developed [21-25]. The occurrence of the one or the other nitride-precipitation process can be understood as follows.

The values of the so-called interaction parameter, as defined in Ref. [14], for *Me*N (with *Me* = Ti, Cr and V) development in ferrite compared to the value of the interaction parameter for $SiN_{1.33}$ (Si_3N_4) development in ferrite (cf. Table IV and Section 5.1) are largely different and thus suggest the improbability of formation of ternary mixed nitrides upon nitriding Fe-*Me*-Si alloys.

As compared to crystalline Si_3N_4, *Me*N has a distinctly different crystal structure and *Me*-N bonding character [74].

In the case of ternary iron-based alloys which contain two different alloying elements (Me_a, Me_b), which both can form nitrides of identical crystal structure, precipitation of mixed ternary nitrides is more likely.

Table 13: Interaction parameter, *I*, defined as the ratio of the change of the chemical Gibbs energy upon precipitation of *Me* (with *Me* = Al, Ti, Cr, V *and* Si) and N, both dissolved in α-Fe (ferrite), as MeN_n, at 773 K. $\Delta G_{MeN_n}^{773K} = \Delta G_{MeN_n}^{0} - n\Delta G_{N}^{\alpha\text{-Fe(N)}}$, where $\Delta G_{MeN_n}^{0}$ is the Gibbs energy of formation for one mole MeN_n and $\Delta G_{N}^{\alpha\text{-Fe(N)}}$ is the Gibbs energy of dissolution of 1 mole nitrogen in ferrite (Fe-*Me* interaction is ignored). $W_{strain} = 6G_{\alpha\text{-Fe}}C\varepsilon^2 V_{MeN_n}$ is the misfit-strain energy developing upon precipitation of MeN_n in ferrite, where $G_{\alpha\text{-Fe}}$ is the shear modulus of ferrite, *C* is given by $3K_{MeNn}/(3K_{MeNn}+4G_{\alpha\text{-Fe}})$, with K_{MeNn} as the bulk modulus of *Me*N, ε is the linear misfit parameter and V_{MeNn} is the molar volume of the nitride. The misfit-strain energy was calculated according to Ref. [14] for the case of full elastic accommodation of the misfit.

alloy	$\Delta G_{MeN_n}^{773K}$ (kJ/mol)	W_{strain} (kJ/mol)	$I = -\frac{\Delta G_{MeN_n}}{W_{strain}}$
Fe-Ti	-300	173	1.7
Fe-V	-186	112	1.7
Fe-Al	-275	272	1.0
Fe-Cr	-91	116	0.8
Fe-Si	-210	523	0.4

This explains the development of metastable, cubic rock-salt crystal structure type, mixed ternary nitrides $Cr_xAl_{1-x}N$ and $Cr_xTi_{1-x}N$ in nitrided ternary Fe-Cr-Al [21-23] and Fe-Cr-Ti [24, 25] alloys. The development of mixed nitrides in the case of Fe-Cr-Al and Fe-Cr-Ti alloys is moreover favored due to the decrease of precipitate/matrix misfit as compared to the development of the stable binary nitrides in the ferrite matrix [21, 24]: Incorporation of Al into CrN decreases the misfit of CrN and ferrite; incorporation of Cr into TiN decreases the misfit of TiN and ferrite.

5.4.2. Influence of coherency strain on the Si_3N_4-precipitation kinetics

The ternary Fe-*Me*-Si alloys (with *Me* = Ti, Cr and V) show distinctively different rates of Si_3N_4 precipitation as reflected by the nitriding rates (Section 5.3.1): The rate of Si_3N_4 precipitation upon nitriding is highest in the Fe-Ti-Si alloys, followed by the Fe-Cr-Si alloy, and slowest in the Fe-V-Si alloy (cf. Section 5.3.1). As compared to the rate of Si_3N_4 precipitation in binary Fe-Si alloy, the additional presence of Ti and Cr appears to have an accelerating effect, whereas the additional presence of V retards the precipitation of Si_3N_4. These effects on the Si_3N_4-precipiation kinetics can be ascribed to the varying degree of coherency, strain-field development, associated with the preceding practically fully (*Me* = Cr, V) or largely (*Me* = Ti) precipitation of (semi-) coherent cubic rock-salt crystal-structure type *Me*N, as follows.

The presence of coherency, misfit-strain fields in the ferritic matrix, arisen by the (preceding) precipitation of *Me*N particles, is an obstacle for dislocation mobility and thus obstructs the development of Si_3N_4: Si_3N_4 has a large volume misfit with the ferrite matrix such that plastic accommodation associated with dislocation generation accompanies the precipitation of Si_3N_4 (see Ref. [19]; cf. discussion of ferrite-lattice parameter changes for the Fe-Si alloy upon nitriding in Section 5.3.3). It may thus be expected that the precipitation of Si_3N_4 is hindered

most severely if the misfit-strain fields around the *Me*N precipitates are most pronounced. As follows from the results presented in Sections III, B and III, C, in case of the Fe-V-Si alloy the degree of coherency is larger (e.g. see Figure 28c: SADP with distinct streaks) and upon prolonged long time nitriding (involving aging/coarsening of the VN precipitates) this coherency is only partly lost (see Table 11and Figure 32; discussed in Section 5.3.3). Both effects (degree of coherency and its perseverance) are much less pronounced for the Fe-Ti-Si alloys (see Sections 5.3.2 and 5.3.3). On this basis it can be understood that pronounced retardation of the Si_3N_4 precipitation, as compared to the rate of Si_3N_4 precipitation in the binary Fe-Si alloy, occurs for the Fe-V-Si alloy.

Evidently the TiN precipitates can realize/maintain their coherency and elastic accommodation of their misfit with the ferrite matrix much less well than the VN precipitates (the misfit with the ferritic matrix decreases in the order TiN → CrN → VN). As a matter of fact, whereas for the Fe-V-Si and Fe-Cr-Si alloys, the Si_3N_4 precipitation effectively occurs after full *Me*N precipitation (see plateaus in Figure 26b after 24 h of nitriding), partial overlap with the subsequent Si_3N_4 precipitation occurs in case of the Fe-Ti-Si alloys (no plateau in Figure 26b after 24 h of nitriding).

Heterogeneous precipitation of Si_3N_4 can be accelerated over homogeneous precipitation if sufficient favorable nucleation sites exist in the ferrite matrix. As soon as upon coarsening/aging of the *Me*N platelets incoherency occurs at the *Me*N/α-Fe interface such nucleation sites are produced (note the finely dispersed nature of the *Me*N precipitates). Considering the state of (coherency) stress around the *Me*N platelets, coherency is best realized and maintained along the faces of the *Me*N platelets, where $\{100\}$ -planes of the ferrite matrix are parallel to $\{100\}$ -planes of *Me*N, whereas incoherency is expected first at the narrow surface/rim of the platelets, where $\{100\}$ -planes of the ferrite matrix are parallel to $\{110\}$ -planes of *Me*N (see the schematic

Figure 33). Recognizing that the interfacial energy of an incoherent interface is distinctively larger than that of a coherent interface,[11] heterogeneous nucleation of Si_3N_4 is expected at such incoherent interfaces. This has been observed indeed in this study (see Fig. 5(d)). Again, upon continued nitriding (i.e. aging) incoherency for the *Me*N/α-Fe interface is observed first for the TiN precipitates and latest for the VN precipitates (see results presented in Sections III, B and III, C and the above discussion), in accordance with the (volume) misfit for TiN being largest. As a consequence the provision of nucleation sites for Si_3N_4 at (the high density of) *Me*N/α-Fe interfaces leads to an acceleration of the Si_3N_4 precipitation in the Fe-Ti-Si and, to a much lesser degree, in the Fe-Cr-Si alloys, as compared to the Si_3N_4 precipitation in the binary Fe-Si alloy.

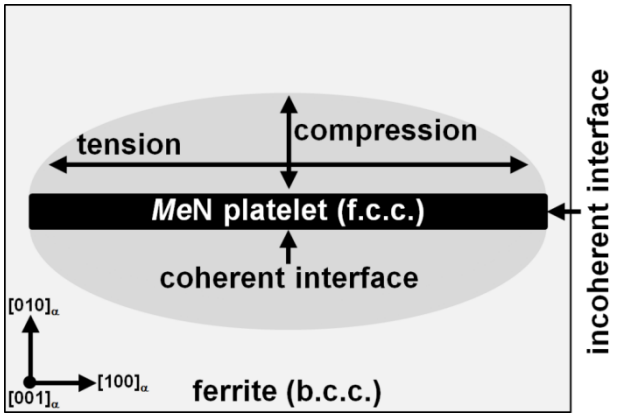

Figure 33: Schematic drawing of a (semi-) coherent *Me*N platelet in the ferrite matrix. Due to the (semi-) coherency of the misfitting *Me*N platelet, the ferrite matrix surrounding the platelet is tetragonally distorted: (i) Two principal tensile stresses act parallel to the platelet and (ii) a principal compressive stress acts normal to the platelet.

5.5. Conclusions

- In contrast with the formation of "mixed" nitrides, $Me_{a(1-x)}Me_{b(x)}N$, in Fe-Al-Cr and Fe-Cr-Ti alloys upon nitriding, nitriding of Fe-*Me*-Si alloys (with *Me* = Ti, Cr and V) leads to the precipitation of *Me*N and Si_3N_4 nitrides, separately and successively: First all *Me*N precipitates as finely-dispersed, nano-sized, crystalline platelets. The *Me*N platelets have the rock-salt type crystal structure and maintain the Baker-Nutting orientation relationship with the surrounding ferrite matrix. Subsequently all Si precipitates as larger, amorphous, cubically Si_3N_4 particles with the cube faces parallel to $\{100\}_{\alpha\text{-Fe}}$ planes. The formation of separate *Me*N and Si_3N_4 nitrides, and not a mixed nitride, can be ascribed to the large difference of the *Me*-N and Si-N interactions.
- The precipitation rate of Si_3N_4 differs strongly for the different Fe-*Me*-Si alloys; the Si_3N_4 precipitation is pronouncedly retarded in the Fe-V-Si alloy and accelerated in the Fe-Ti-Si and Fe-Cr-Si alloys, as compared to the binary Fe-Si alloy. On the basis of transmission electron microscopy and diffraction data, and X-ray diffraction-line shift and broadening data, these striking differences in nitriding kinetics could be ascribed to subtle differences in the development and relaxation of coherency strains:

  (i) A strongly retarded Si_3N_4 precipitation is observed in the Fe-V-Si alloy, as a consequence of the highest degree of coherency of *Me*N precipitate and ferrite matrix occurring for VN (as compared to TiN and CrN) and of preservation of this coherency for a distinct part upon prolonged nitriding.

  (ii) An accelerated Si_3N_4 precipitation is observed for the Fe-Ti-Si and Fe-Cr-Si alloys due to a rapidly occurring coherent → incoherent transition for the TiN/α-Fe,

CrN/α-Fe interfaces. Subsequent heterogeneous nucleation of Si_3N_4 at these incoherent interfaces takes place. The larger the alloying element, Ti, content in the Fe-Ti-Si alloy the higher the TiN-particle density and the faster the Si_3N_4 precipitation (more nucleation sites).

(iii) The Si_3N_4 precipitation occurs in the Fe-Cr-Si alloy and in particular in the Fe-V-Si alloy, largely separated in time, after the *Me*N precipitation, whereas a partial overlap occurs in the Fe-Ti-Si alloys. This phenomenon is consistent with a coherent → incoherent transition of the CrN/α-Fe and VN/α-Fe interfaces after completed CrN/VN precipitation, and a partial coherent → incoherent transition of the TiN/α-Fe interface before completed TiN precipitation.

Acknowledgments

The authors thank Mr. Dipl.-Ing. (FH) P. Kress and Mr. W. Engelhardt for assistance with the nitriding experiments and Prof. Dr. van Aken to provide access to the TEM (all are with the Max Planck Institute for Intelligent Systems, Stuttgart).

Chapter 6

Summary

6.1 Summary in the English language

This thesis demonstrates that gas nitriding is suitable for fundamental scientific research because the thermodynamic conditions (chemical potential of nitrogen) of the nitriding process can be controlled precisely over a wide range and nitriding of iron-based model alloys is suitable to arrive at a better understanding of the nitriding process and thereby gain fundamental scientific knowledge about phase transformations, thermodynamics and kinetics.

Nitriding of steel alloyed with tungsten can lead to the precipitation of tungsten nitride. Despite the frequent use of tungsten as an alloying element (tungsten improves the machinability), little is known about the precipitation process of tungsten nitride in iron. Therefore, the crystal structure and morphology of tungsten nitride precipitated upon nitriding a binary iron-based Fe-W alloy was investigated (**Chapter 2**).

For this specimens of an iron-based binary Fe-0.5 at.% W alloy were nitrided at 610 °C with a nitriding potential of 0.104 $atm^{-1/2}$ for different times. At initial stages of nitriding finely-dispersed, nano-sized, α``-$Fe_{16}N_2$-type tungsten-nitride platelets developed along $\{100\}_{\alpha\text{-Fe}}$-lattice planes of the ferrite matrix. Continued nitriding resulted in the development of colonies with a lamellar structure (alternating nitride and ferrite-matrix lamellae) and at this stage the crystal structure of the tungsten nitride can be conceived as a superstructure of hexagonal δ-WN which obeys a Pitsch-Schrader orientation relationship with the ferrite matrix. The tungsten-nitride lamellas are unstable with respect to hydrogen reduction at 470 °C and thus dissolution of the

nitrides occur upon denitriding, leaving back tungsten-rich regions, at the location of former nitride-lamellae, due to the low diffusivity of tungsten in ferrite at 470 °C.

Interestingly, when the surface regions of the specimens contained significant amount of defects (dislocations) an unusually high amount of tungsten-nitride precipitation occurred at the surface. Moreover, the developed hexagonal tungsten nitrides had no specific orientation relationship with the underlying ferrite substrate and showed a sharp texture (basal planes of the tungsten nitrides are parallel to the substrate surface). The occurrence of the textured tungsten nitride at the surface has been attributed to a relatively lower surface energy of the (close-packed) $\{0001\}_{W\text{-}N}$ surface.

The formation of pores in the iron-nitride compound layer is a well-known phenomenon and has been investigated extensively. However, pore formation is not restricted only to the iron-nitride compound layer: Pores can also develop in the diffusion zone which consists of nitrogen austenite and/or nitrogen ferrite. The effects of alloying elements on pore formation in nitrogen ferrite and nitrogen austenite and the role of grain boundaries on pore formation were investigated in **Chapter 3**.

For this pure iron and binary iron-based Fe-*Me* alloys (with *Me* = Al, Si, Cr, Co, Ni and Ge) were nitrided at 650 °C for 72 hours with different nitriding potentials in order to stabilize nitrogen ferrite (r_N = 0.050 $atm^{-1/2}$) or nitrogen austenite (r_N = 0.104 $atm^{-1/2}$) at the surface of the specimens. The thermodynamic assessment showed that, at the applied nitriding conditions, pure nitrogen ferrite as well as pure nitrogen austenite *underneath* the specimen surface is thermodynamically unstable. Due to this the decomposition of nitrogen-ferrite into nitrogen-depleted ferrite and nitrogen gas and the decomposition of nitrogen-austenite into nitrogen-depleted austenite and nitrogen gas is expected. The assessment of required pressures according

to both the *von Mises* criterion as well as the *Tresca* criterion to yield the ferrite and austenite matrix surrounding the pores is smaller than the expected pressure of N_2 gas in the pores. Indeed, the results of the assessments were experimentally supported: Pores developed at grain boundaries in nitrogen ferrite and nitrogen austenite underneath the surface and ferrite matrix bulged out to the surface in case of pores very close to the surface. A nitrided pure iron single crystal did not show pore formation, even after longer nitriding treatments as applied on the polycrystalline specimens, revealing the importance of grain boundaries as nucleation sites for pores.

A series of iron-based Fe-*Me* alloys (with *Me* = Al, Si, Cr, Co, Ni and Ge) were nitrided at similar conditions as the pure iron specimens and pore formation occurred in all alloys. It showed that alloying elements which enhance the equilibrium nitrogen solubility of iron, i.e. Al and Cr, and which precipitate easily as nitrides in the iron matrix, such as AlN and CrN, show less porosity. This is due to the competition between precipitation of alloying-element nitrides and the formation of pores and later on, alloying-element nitrides strengthen the matrix. Alloying elements which reduce the equilibrium nitrogen solubility of iron, i.e. Co and Ge, and which do not easily precipitate as nitrides in the iron matrix showed, in comparison to pure iron, a higher degree of porosity. In these cases, no competition between alloying-element nitride precipitation and pore formation takes place and the reduced equilibrium nitrogen solubility promotes pore formation. Si dissolved in iron lowers also the equilibrium nitrogen solubility of iron but nitrided Fe-Si alloy showed only marginal pore formation. Pore formation in Fe-Si alloy is retarded due to Si_3N_4 precipitation in the bulk and along ferrite-grain boundaries which inhibits the nucleation of pores.

Industrial nitriding of steel containing multiple alloying elements where each alloying element has its own interaction with nitrogen shows the necessity of understanding the nitriding behavior

of multicomponent iron alloys. Only few research works investigated the nitriding response of iron-based alloys which contain more than one alloying element. It is known that in nitrided iron-based ternary Fe-Cr-Ti and Fe-Cr-Al alloys precipitation of metastable, mixed, ternary nitrides $Me_{a(1-x)}Me_{b(x)}N$, instead of the stable binary nitrides Me_aN and Me_bN, occurs. The development of such mixed nitrides has been attributed to the similarities of the corresponding binary nitrides; the binary nitrides are of the same stoichiometry and of the same crystal structure. The research work presented in **Chapter 4** investigated the nitride precipitation process, the crystal structure and the morphology of nitrides developing in an iron-based ternary alloy containing alloying elements whose corresponding binary nitrides exhibit a rather different nature, i.e. different stoichiometry and different crystal structure.

For this V and Si were chosen as alloying elements and specimens of an iron-based ternary Fe-V-Si alloy were nitrided at 580 °C with a nitriding potential of 0.104 $atm^{-1/2}$ for different times. Upon nitriding, in a first stage, the ferrite matrix gets saturated with nitrogen and all V precipitates as finely-dispersed, nano-sized, crystalline VN platelets. These VN platelets exhibit the rock-salt type crystal structure and maintain the Baker-Nutting orientation relationship with the surrounding ferrite matrix. Continued nitriding leads, in a second stage, to the very slow and subsequent precipitation of stoichiometric but *amorphous* Si_3N_4. The amorphous nature of the Si_3N_4 particles is explained by the thermodynamic stabilization due to a lower energy of the amorphous/crystalline interface in comparison to the crystalline/crystalline interface. At the beginning of the Si_3N_4 precipitation, Si_3N_4 particles are cubical with cube faces parallel to $\{100\}_{\alpha\text{-Fe}}$ planes whereas at later stages the Si_3N_4 particles are octapod-shaped. This change of morphology has been attributed to the anisotropic growth of misfitting Si_3N_4 particles as a result of an anisotropic strain-field in the surrounding, elastically anisotropic, ferrite matrix. Development of the separate VN and Si_3N_4 particles, instead of mixed nitride, has been ascribed

to the large difference in the interaction of V and Si with nitrogen, i.e. large differences in the chemical affinity to nitrogen and the volume misfit of nitrides with the ferrite matrix.

Moreover, it was found that the Si_3N_4-precipitation rate upon nitriding the ternary Fe-V-Si alloy specimens was much lower than the Si_3N_4-precipitation rate in a corresponding binary Fe-Si alloy specimen with a similar Si content. This phenomena is a result of the extra enhancement of the elastic-strain energy due to the development of highly misfitting Si_3N_4 particles in the, due to (semi-) coherent VN platelets, already severely strained ferrite matrix. Further, the VN platelets act as obstacles for the movement of dislocations which are produced by the plastic accommodation of the Si_3N_4 particle/ferrite-matrix volume misfit. In order to support the above interpretation an Fe-V-Si alloy specimen nitrided such that only all V has been precipitated as VN was annealed at higher temperature (750^{o}C under Ar atmosphere) to relieve all the misfit strains associated with the already developed VN particles. Further nitriding of such "nitrided + annealed" ternary Fe-V-Si specimen showed the Si_3N_4-precipitation at a faster rate as in the binary Fe-Si alloy.

After realizing the *separate* and *successive* precipitation of VN and Si_3N_4 in nitrided Fe-V-Si alloy and the influence of coherency strains on the rate of Si_3N_4 precipitation, investigations were extended to other ternary Fe-*Me*-Si ternary alloys to further understand the magnitude of coherency strains on the rate of Si_3N_4 precipitation. Due to differences in the lattice parameter of the particular nitrides the coherency-strain fields induced by misfitting *Me*N (with *Me* = Ti, Cr, V) platelets in the ferrite matrix are of different magnitudes: Highest for TiN, followed by CrN and lowest for VN. The project presented in **Chapter 5** was aimed to investigate the effect of the magnitude of the coherency strains caused by TiN, CrN and VN on the subsequently precipitating Si_3N_4 particles.

To this end specimens of iron-based ternary Fe-*Me*-Si alloys (with *Me* = Ti, Cr and V) were nitrided at 580 °C with a nitriding potential of 0.104 $atm^{-1/2}$ for different times. Similar to Fe-V-Si, in the Fe-*Me*-Si alloys in a first stage of nitriding precipitation of all *Me* as finely-dispersed, nano-sized and crystalline *Me*N platelets occurred. These *Me*N platelets exhibit the rock-salt type crystal structure and maintained the Baker-Nutting orientation relationship with the surrounding ferrite matrix. Upon continued nitriding, the subsequent precipitation of stoichiometric and amorphous Si_3N_4 took place. The development of mixed nitrides was not observed and the separate formation of *Me*N and Si_3N_4 is ascribed to the large difference in the interaction of *Me* and Si with nitrogen.

Further, the Si_3N_4-precipitation rate differed strongly for the particular Fe-*Me*-Si alloys; in comparison to a binary Fe-Si which contains a similar Si content, as in ternary alloys, the Si_3N_4-precipitation rate is accelerated in the Fe-Ti-Si and the Fe-Cr-Si alloys and decelerated in the Fe-V-Si alloy. These diverse Si_3N_4-precipitation rates are related to differences in the development and relaxation of coherency strains due to *Me*N precipitates. The Si_3N_4-precipitation rate is accelerated for the Fe-Ti-Si and the Fe-Cr-Si alloys due to a rapidly occurring coherent → incoherent transition of the TiN/α-Fe, CrN/α-Fe interfaces and Si_3N_4 nucleates subsequently at these incoherent interfaces. In case of nitrided Fe-Ti-Si alloys it was shown that the higher the Ti content and thus the higher the TiN-particle density the faster is the Si_3N_4 precipitation due to a simultaneously increased amount of possible nucleation sites. The Si_3N_4-precipitation rate is retarded in the Fe-V-Si alloy due to the highest degree of coherency of the VN precipitates with the ferrite matrix and a preservation of the coherency for a distinct part even for very prolonged nitriding. In contrast to the Fe-Ti-Si alloys, the precipitation of Si_3N_4 in the Fe-Cr-Si and in the Fe-V-Si alloy is largely separated in time after the CrN/VN precipitation. The reason is that TiN

loses the coherency with the ferrite matrix before all Ti has precipitated as TiN whereas CrN/VN became incoherent not before completed CrN/VN precipitation.

6.2 Zusammenfassung in der deutschen Sprache

Die vorliegende Arbeit zeigt, dass mit dem Prozess des Gasnitrierens Grundlagenforschung betrieben werden kann da die thermodynamischen Bedingungen (das chemische Potential von Stickstoff) über einen weiten Bereich sehr genau kontrollierbar ist. Das Gasnitrieren von Eisenbasislegierungen führt dabei zu einem besseren Verständnis des eigentlichen Nitrierprozesses und gleichzeitig wird ein besseres Verständnis über grundlegende Prozesse wie Phasenumwandlungen, Thermodynamik und Kinetik erhalten.

Nitrieren von wolframhaltigem Stahl kann zu der Ausscheidung von Wolframnitriden führen und obwohl Wolfram häufig als Legierungselement in Stahl eingesetzt wird (Wolfram verbessert die Spanbarkeit) ist wenig über die Ausscheidung von Wolframnitriden in Eisen bekannt. Aus diesem Grund wurden die Kristallstruktur und die Morphologie von Wolframnitriden untersucht, die sich während dem Nitrieren einer binären Fe-W Legierung ausgeschieden haben (**Kapitel 2**).

Hierfür wurden Proben einer eisenbasierenden binären Fe-0.5 at.% W Legierung bei 610 °C mit einem Nitrierpotential von 0.104 $atm^{-1/2}$ für unterschiedlich lange Zeit nitriert. In frühen Stadien des Nitrierens entwickeln sich feinverteilte, nanometergroße, α´´-ähnliche Wolframnitridplättchen auf $\{100\}_{\alpha\text{-Fe}}$-Gitterebenen aus. Wird das Nitrieren fortgesetzt, entstehen Kolonien mit lamellarer Struktur (abwechselnde Nitrid- und Eisenmatrixlamellen) wobei die Kristallstruktur der Nitridlamellen als eine Überstruktur von hexagonalem δ-WN aufgefasst werden kann und die Nitridlamellen eine Pitsch-Schrader Orientierungsbeziehung mit der Eisenmatrix aufweisen. Diese Nitridlamellen lösen sich beim Denitrieren (Wasserstoffreduktion)

bei 470 °C auf und lassen dabei, aufgrund der langsamen Diffusion von Wolfram in Eisen bei dieser Temperatur, mit Wolfram angereicherte Regionen zurück.

Interessanterweise bilden sich während dem Nitrieren, wenn die Probenoberfläche eine ausreichend hohe Defektdichte (Versetzungen) aufweist, auch an der Oberfläche der Proben ungewöhnlich viele Wolframnitride. Diese Oberflächennitride zeigen eine ausgeprägte Fasertextur (Basalebenen der Wolframnitride sind parallel zum Eisensubstrat), besitzen aber keine Orientierungsbeziehung mit dem darunterliegenden Eisensubstrat. Die Ausbildung dieser texturierten Oberflächennitride wird mit einer niedrigen Oberflächenenergie der (dichtgepackten) $\{0001\}_{W\text{-}N}$ -Oberfläche erklärt.

Porenbildung in der Eisennitrid-Verbindungsschicht ist ein wohlbekanntes Phänomen und wurde umfassend untersucht. Allerdings tritt die Porenbildung nicht nur in der Eisennitrid-Verbindungsschicht auf: Poren treten auch in der Diffusionszone auf, welche aus Stickstoffaustenit und/oder Stickstofferrit besteht. Die Auswirkungen von Legierungselementen in Stickstoffaustenit und Stickstofferrit, sowie die Rolle von Korngrenzen auf die Porenbildung wurde in **Kapitel 3** untersucht.

Hierzu wurde reines Eisen und binäre eisenbasierende Fe-*Me* Legierungen (mit *Me* = Al, Si, Cr, Co, Ni und Ge) bei 650 °C für 72 h mit unterschiedlichen Nitrierpotentialen nitriert um einerseits Stickstofferrit (r_N = 0.050 atm$^{-1/2}$) oder Stickstoffaustenit (r_N = 0.050 atm$^{-1/2}$) an der Probenoberfläche zu stabilisieren. Dabei zeigte eine thermodynamische Abschätzung, dass bei den angewandten Nitrierbedingungen reiner Stickstofferrit als auch reiner Stickstoffaustenit unterhalb der Probenoberfläche nicht stabil ist. Deshalb wird die Zersetzung von Stickstoff-austenit bzw. Stickstofferrit zu Stickstoff verarmten Austenit bzw. Ferrit und Stickstoffgas erwartet. Eine Abschätzung der Drücke (Fließbedingung nach *von Mises* und *Tresca*), die

notwendig sind um die Ferrit- bzw. die Austenitmatrix um die Poren plastisch zu verformen zeigte, dass diese Drücke (Fließspannung) kleiner sind als die erwarteten Drücke in Poren aufgrund von Stickstoffgas. Tatsächlich wurden die Ergebnisse der theoretischen Abschätzungen durch experimentelle Ergebnisse unterstützt: Poren bildeten sich an Korngrenzen in Stickstoff-ferrit und Stickstoffaustenit unterhalb der Probenoberfläche und im Falle von oberflächennahen Poren in Ferrit, wurde eine Auswölbung der Ferritmatrix beobachtet. Beim Nitrieren einer einkristallinen reinen Eisenprobe bildeten sich keine Poren, auch nicht nach längeren Nitrierzeiten im Vergleich zu denen die bei den polykristallinen Proben angewandt wurden. Damit zeigte sich die Bedeutung von Korngrenzen als Keimbildungsstelle für Poren.

Eine Reihe von Proben eisenbasierender Fe-*Me* Legierungen (mit *Me* = Al, Si, Cr, Co, Ni und Ge) wurden unter gleichen Bedingungen wie die Reineisenproben nitriert und in allen Proben entwickelten sich Poren. Dabei zeigte sich in Legierungen welche Legierungselemente enthalten die die Gleichgewichts-Stockstofflöslichkeit in Eisen erhöhen, d. h. Al und Cr, und die sich relativ leicht als Nitride in der Eisenmatrix ausscheiden, wie AlN und CrN, weniger Porosität als in reinem Eisen. Dies geht auf den Wettbewerb zwischen der Ausscheidung von Legierungselementnitriden und der Porenbildung zurück und wenn Legierungselementnitride ausgeschieden sind verstärken diese die Eisenmatrix. In Legierungen welche Legierungselemente enthalten die die Gleichgewichts-Stockstofflöslichkeit in Eisen senken, d. h. Co und Ge, und die sich nicht als Nitride in der Eisenmatrix ausscheiden, zeigen mehr Porosität als reines Eisen. In diesen Fällen existiert kein Wettbewerb zwischen der Ausscheidung von Legierungselementnitriden und der Porenbildung und die gesenkte Stickstofflöslichkeit in Eisen fördert Porenbildung. Auch Si senkt die die Gleichgewichts-Stockstofflöslichkeit in Eisen, jedoch ist die Porenbildung im Fall der nitrierten Fe-Si Legierung gering. In diesem Fall ist die

Porenbildung aufgrund von Si_3N_4 Ausscheidungen im Volumen und entlang von Korngrenzen gehemmt, wobei letzteres die Keimbildung von Poren behindert.

Das industrielle Nitrieren von Stählen welche eine Vielzahl an Legierungselementen aufweisen, wobei die einzelnen Legierungselemente jeweils unterschiedlich mit Stickstoff wechselwirken, zeigt die Notwendigkeit auf, das Nitrierverhalten von mehrkomponenten Eisenlegierungen zu untersuchen. Nur wenige wissenschaftliche Arbeiten untersuchten bisher das Nitrierverhalten von Eisenbasislegierungen die mehr als ein Legierungselement enthielten. In den Fällen von nitrierten ternären Fe-Cr-Al und Fe-Cr-Ti Legierungen ist bekannt, dass sich metastabile, gemischte, ternäre $Me_{a(1-x)}Me_{b(x)}N$ ausscheiden anstelle der stabilen binären Nitride (Me_aN und Me_bN). Die Ausbildung dieser gemischten Nitride wird auf Gemeinsamkeiten der jeweiligen binären Nitride zurückgeführt; die binären Nitride besitzen dieselbe Stöchiometrie und dieselbe Kristallstruktur. In der vorliegenden Arbeit (**Kapitel 4**) wurde der Ausscheidungs-prozess, die Kristallstruktur sowie die Morphologie von Nitriden untersucht, welche sich in einer ternären Legierung ausbilden, die Legierungselemente enthält welche von unterschiedlicher Art sind, d. h. eine verschiedene Stöchiometrie als auch eine verschiedene Kristallstruktur aufweisen.

Hierzu wurden die Legierungselemente V und Si ausgewählt und Proben einer eisenbasierenden ternären Fe-V-Si Legierung wurden bei 580 °C mit einem Nitrierpotential von 0.104 $atm^{-1/2}$ für unterschiedliche Zeiten nitriert. In einem ersten Stadium des Nitrierens wird die Eisenmatrix mit Stickstoff gesättigt und das gesamte V scheidet sich als feinverteilte, kristalline VN-Plättchen aus. Diese VN-Plättchen besitzen die kubische Kochsalz-Kristallstruktur und halten eine Baker-Nutting Orientierungsbeziehung mit der umgebenden Eisenmatrix ein. Wird das Nitrieren fortgesetzt, so scheidet sich in einem zweiten, anschließenden Stadium sehr langsam stöchiometrisches und *amorphes* Si_3N_4 aus. Das auftreten von amorphem Si_3N_4 wird dabei mit einer thermodynamischen Stabilisierung aufgrund einer kleineren Energie der

amorph/kristallin Grenzfläche im Vergleich mit einer kristallin/kristallin Grenzfläche erklärt. Zu Beginn der Si_3N_4 Ausscheidung sind die Si_3N_4 Teilchen würfelförmig und die Würfelflächen sind parallel zu $\{100\}_{\alpha\text{-Fe}}$-Gitterebenen ausgerichtet, wohingegen sehr lange Nitrierzeiten zu „achtbeinigen“ Teilchen führt. Diese Gestaltsänderung wird dem anisotropen Wachstum der Si_3N_4 Teilchen zugesprochen, aufgrund eines anisotropen Dehnungsfeldes in der umgebenden, elastisch anisotropen, Eisenmatrix. Die Ausscheidung von getrennten VN und Si_3N_4 Teilchen, anstelle von Mischnitriden, wird den großen Unterschieden in der Wechselwirkung von V und Si mit Stickstoff zugeschrieben, d. h. große Unterschiede in der chemischen Affinität zu Stickstoff und große Unterschiede in der Fehlpassungen der Nitride mit der Eisenmatrix.

Darüber hinaus zeigte sich, dass die Si_3N_4-Ausscheidungsrate beim Nitrieren der ternären Fe-V-Si Legierung viel langsamer als bei einer binären Fe-Si Legierung ist und dies bei gleichem Si Gehalt. Dieses Phänomen geht auf die zusätzliche Steigerung der elastischen Verspannungsenergie aufgrund von stark fehlpassenden Si_3N_4-Teilchen zurück, die sich in der Eisenmatrix ausbilden welche ohnehin schon wegen den (teil-) kohärenten VN-Plättchen stark verspannt ist. Weiterhin fungieren die VN-Plättchen als Hindernisse für die Bewegung von Versetzungen, die im Zusammenhang mit der plastischen Anpassung zwischen Si_3N_4-Teilchen und Eisenmatrix entstehen. Um diese Interpretation zu stützen, wurde eine Probe der Fe-V-Si Legierung nur solange nitriert bis sich das gesamte V als VN ausgeschieden hat und anschließend wurde diese Probe bei erhöhter Temperatur (750 °C) angelassen um Verspannungen aufgrund der VN-Plättchen durch Erholungsprozesse abzubauen. Weiteres Nitrieren dieser „nitrierten + angelassenen“ Fe-V-Si Probe führte zu einer Si_3N_4-Ausscheidungsrate vergleichbar schnell wie in der binären Fe-Si Legierung.

Nachdem die *separate* und *nachfolgende* Ausscheidung von VN und Si_3N_4 in nitrierten Proben der Fe-V-Si Legierung entdeckt und der Zusammenhang zwischen Kohärenzspannungen und der Si_3N_4-Ausscheidungsrate erkannt war, wurden die Untersuchungen mit weiteren ternären Fe-*Me*-Si Legierungen fortgesetzt, um den Einfluss unterschiedlich großer Kohärenzspannungen auf die Si_3N_4-Ausscheidungsrate besser zu verstehen. Dabei entwickeln unterschiedliche fehlpassende Nitride (TiN, CrN, VN) aufgrund unterschiedlicher Gitterparameter verschieden hohe Kohärenzspannungen. Diese Kohärenzspannungen in Ferrit sind im Falle von TiN am größten, gefolgt von CrN und am kleinsten bei VN. Die Arbeit, welche in **Kapitel 5** vorgestellt wird, hatte das Ziel die Auswirkung unterschiedlich großer Kohärenzspannungen, hervorgerufen durch TiN, CrN und VN, auf die nachfolgende Si_3N_4-Ausscheidung zu untersuchen.

Hierzu wurden Proben von eisenbasierenden ternären Fe-*Me*-Si Legierungen (mit *Me* = Ti, Cr und V) bei 580 °C mit einem Nitrierpotential von 0.104 $atm^{-1/2}$ für unterschiedliche Zeit nitriert. Vergleichbar mit Proben der Fe-V-Si Legierung, scheidet sich in einem ersten Stadium alles Ti/Cr als feinverteilte, kristalline TiN/CrN-Plättchen aus. Diese Plättchen besitzen ebenfalls die kubische Kochsalz-Kristallstruktur und halten eine Baker-Nutting Orientierungsbeziehung mit der umgebenden Eisenmatrix ein. Wird das Nitrieren fortgesetzt, so scheidet sich in einem zweiten, anschließenden Stadium stöchiometrisches und *amorphes* Si_3N_4 aus. Die Ausscheidung von getrennten TiN/CrN und Si_3N_4 Teilchen, anstelle von Mischnitriden beruht auf den großen Unterschieden in der Wechselwirkung von Ti/Cr und Si mit Stickstoff.

Die Si_3N_4-Ausscheidungsrate unterscheidet sich unter den einzelnen Fe-*Me*-Si Legierungen sehr stark; im Vergleich mit einer binären Fe-Si Legierung mit gleichem Si-Gehalt ist die Si_3N_4-Ausscheidungsrate in den Fe-Ti-Si und Fe-Cr-Si Legierungen beschleunigt, wohingegen die Si_3N_4-Ausscheidungsrate in der Fe-V-Si Legierung stark verlangsamt ist. Diese unterschiedlichen Si_3N_4-Ausscheidungsraten beruhen auf Unterschieden in der Entwicklung und Relaxation von

Kohärenzspannungen aufgrund der ausgeschiedenen *Me*N. Eine beschleunigte Si_3N_4-Ausscheidungsrate in den Fe-Ti-Si und Fe-Cr-Si Legierungen basiert auf einem schnell auftretenden Übergang der TiN/α-Fe bzw. CrN/α-Fe Grenzflächen von kohärent → inkohärent. Außerdem keimt Si_3N_4 an diesen nun inkohärenten Grenzflächen. Es zeigte sich auch, dass je höher der Ti Anteil und somit eine höhere TiN-Teilchendichte, desto schneller scheidet sich das Si_3N_4 aus, aufgrund einer gleichzeitig erhöhten Dichte an möglichen Keimbildungsstellen. Die Si_3N_4-Ausscheidung in der Fe-V-Si Legierung ist verzögert, da VN-Ausscheidungen den höchsten Grad an Kohärenz mit der Eisenmatrix besitzen und die Kohärenz selbst bei langem Nitrieren annähernd aufrechterhalten wird. Im Gegensatz zu den Fe-Ti-Si Legierungen ist die Ausscheidung von Si_3N_4 in den Fe-Cr-Si und Fe-V-Si Legierungen zeitlich stark von der CrN/VN-Ausscheidung getrennt. Der Grund hierfür liegt an dem sehr frühen Verlust der Kohärenz von TiN mit der Eisenmatrix, noch bevor das gesamte Ti als TiN ausgeschieden ist, wohingegen CrN und VN die Kohärenz mit der Eisenmatrix erst verlieren nachdem die gesamte CrN/VN-Ausscheidung abgeschlossen ist.

Bibliography

[1] Liedtke D, Baudis U, Boßlet J, Huchel U, Klümper-Westkamp H, Lerche W, Spies H-J. Expert-Verlag, Renningen-Malmsheim 2006;3rd ed.

[2] Unterweiser PM, Gray AG (eds.). *Source Book on Nitriding*, ASM, Metals Park, OH 1977.

[3] Mittemeijer EJ. *ASM Handbook* (eds. Dossett, JI and Totten, GE) 2013;4A:619.

[4] Leineweber A, Gressmann T, Mittemeijer EJ. Surf. Coat. Technol. 2012;206:2780.

[5] Mittemeijer EJ, Slycke JT. Surf. Eng. 1996;12:152.

[6] Lehrer E. Z. Elektrochem. 1930;36.

[7] Mittemeijer EJ, Somers MAJ. Surf. Eng. 1997;13:483.

[8] Kunze J. *Nitrogen and Carbon in Iron and Steel*. Berlin: Akademie Verlag 1990.

[9] Somers MAJ, Vanderpers NM, Schalkoord D, Mittemeijer EJ. Metal. Trans. A 1989;20:1533.

[10] Biglari MH, Brakman CM, Somers MAJ, Sloof WG, Mittemeijer EJ. Z. Metallk. 1993;84:124.

[11] Mittemeijer EJ. *Fundamentals of Materials Science*, Springer 2011, Chapter 9.

[12] JCPDS. PDF-2 (2002) database. Version 2.1. International Center for Diffraction Data.;Version 2.1.

[13] Bain EC. T. Am. I. Min. Met. Eng. 1924;70:25.

[14] Somers MAJ, Lankreijer RM, Mittemeijer EJ. Philos. Mag. A 1989;59:353.

[15] G. R. Booker, Norbury J. Nature 1959;184:1311.

[16] Mittemeijer EJ, Biglari MH, Bottger AJ, van der Pers NM, Sloof WG, Tichelaar FD. Scripta Mater. 1999;41:625.

[17] Meka SR, Jung KS, Bischoff E, Mittemeijer EJ. Philos. Mag. 2012;92:1435.

[18] van Landeghem HP, Goune M, Redjaimia A. Steel Res. Int. 2012;83:590.

[19] Meka SR, Bischoff E, Rheingans B, Mittemeijer EJ. Philos. Mag. Lett. 2013;93:238.

[20] Roberts W, Jack KH, Grieveso.P. Journal of the Iron and Steel Institute 1972;210:931.

[21] Clauss AR, Bischoff E, Hosmani SS, Schacherl RE, Mittemeijer EJ. Metall. Mater. Trans. A-Phys. Metall. Mater. Sci. 2009;40A:1923.

[22] Clauss AR, Bischoff E, Schacherl RE, Mittemeijer EJ. Philos. Mag. 2009;89:565.

[23] Clauss AR, Bischoff E, Schacherl RE, Mittemeijer EJ. Mater. Sci. Technol. 2010;26:297.

[24] Jung KS, Meka SR, Schacherl RE, Bischoff E, Mittemeijer EJ. Metall. Mater. Trans. A-Phys. Metall. Mater. Sci. 2012;43A:934.

[25] Jung KS, Schacherl RE, Bischoff E, Mittemeijer EJ. Metall. Mater. Trans. A-Phys. Metall. Mater. Sci. 2012;43A:763.

[26] Atmani H, Thoumire O. Bulletin of Materials Science 2002;25:219.

[27] Knerr CH, Rose TC, Filkowski JH, Davis JR, Davidson GM, Lampmann SR, Zorc TB, Daquila JL, Ronke AW, Henninger KL, Uhl (eds.) RC. ASM International, Metals Park OH 1991;4:387.

[28] Schubert W-D, Lassner E, Danninger H. International Tungsten Industry Newsletter 2008:6.
[29] Stephenson A, Grieveson P, Jack KH. Scand. J. Met. 1973;2:39.
[30] Predel B. Landolt-Börnstein - Group IV Physical Chemistry Numerical Data and Functional Relationships in Science and Technology online access April 2014;5e: Dy-Er - Fr-Mo.
[31] Jeurgens LPH, Wang ZM, Mittemeijer EJ. Int. J. Mater. Res. 2009;100:1281.
[32] Dahmen U, Ferguson P, Westmacott KH. Acta Metal. 1987;35:1037.
[33] Pitsch W, Schrader A. Arch. Eisenhüttenw. 1958;29.
[34] Mittemeijer EJ, Vogels ABP, van der Schaaf PJ. J. Mater. Sci. 1980;15:3129.
[35] Prenosil B. HTM 1973;28:157.
[36] Somers MAJ, Mittemeijer EJ. Surf Eng 1987;3:123.
[37] Somers MAJ, Kooi BJ, Sloof WG, Mittemeijer EJ. Surf Interface Anal 1992;19:633.
[38] Hoffmann R, Mittemeijer EJ, Somers MAJ. HTM Journal of Heat Treatment and Materials 1996;51.
[39] Middendorf C, Mader W. Z Metallkd 2003;94:333.
[40] Etsion I. J Tribol-T ASME 2005;127:248.
[41] Mittemeijer EJ, VanRooyen M, Wierszyllowski I, Rozendaal HCF, Colijn PF. Z Metallkd 1983;74:473.
[42] Lu FX. Inst Phys Conf Ser. No. 68: Chapter 9 1983.
[43] Mittemeijer EJ. J Met 1985;37:16.
[44] Meka SR, Hosmani SS, Clauss AR, Mittemeijer EJ. Int J Mater Res 2008;99:808.
[45] Stein J, Schacherl RE, Jung M, Meka SR, Rheingans B, Mittemeijer EJ. In.t J. Mater. Res. 2013;104:1053.
[46] Anderson JO, Helander T, Höglund L, Shi PF, Sundman B. Calphad 2002;26.
[47] Kunze J. HTM Journal of Heat Treatment and Materials 1996;51:348.
[48] Yu M, Ma G, Li J. Springer Books 2009.
[49] Clarke KD, Comstock Jr. RJ, Mataya MC, Tyne CJ, Matlock DK. Metall Mater Trans A 2008;39:752.
[50] Chase Jr. MW. J Phys Chem Ref Data, Monograph 9 1998; http://webbook.nist.gov, (online access November 2013).
[51] Speidel MO. Proc. Stainless Steel World 2001 Conference, The Hague - The Netherlands 2001.
[52] Byrnes MLG, Grujicic M, Owen WS. Acta Metall. Mater. 1987;35:1853.
[53] DeHoff RT, Rhines FN. *Quantitative Microscopy*. McGraw-Hill 1968.
[54] Pouchou JL, Pichoir F. Rech. Aerospatiale 1984:167.
[55] Jehn AH, Perrot P. Landolt-Börnstein New Series IV/11D1; (online access November 2013).
[56] Perrot P. Landolt-Börnstein New Series IV/11D3, http://www.springermaterials.com; (online access November 2013).
[57] Biglari MH, Brakman CM, Mittemeijer EJ, van der Zwaag S. Philos. Mag. A 1995;72:931.

[58] Schacherl RE, Graat PCJ, Mittemeijer EJ. Metall Mater Trans A 2004;35A:3387.
[59] Hekker PM, Rozendaal HCF, Mittemeijer EJ. J Mater Sci 1985;20:718.
[60] Zaginaychenko SY, Matysina ZA, Milyan MI. Fiz Met Metalloved 1990:63.
[61] Leineweber A, Lienert F, Glock S, Woehrle T, Schaaf P, Wilke M, Mittemeijer EJ. Z. Kristallogr. 2011:293.
[62] Kunze J, Friedrich POK. J. Mater. Sci. Lett. 1986;5:815.
[63] Fonovic M, Leineweber A, Mittemeijer EJ. Surf Eng 2013; in press.
[64] Bell T, Owen WS. T. Metall. Soc. AIME 1967;239:1940.
[65] The Landolt-Börnstein Database IV/5, Springer Materials, http://www.springermaterials.com; (online access November 2013).
[66] Grabke HJ. Berich. Bunsen Gesell. 1968;72:533.
[67] Grabke HJ. Berich. Bunsen Gesell. 1968;72:541.
[68] Kirkwood DH, Atasoy OE, Keown SR. Met. Sci. 1974;8:49.
[69] Jack DH. Acta Metallurgica 1976;24:137.
[70] Hosmani SS, Schacherl RE, Litynska-Dobrzynska L, Mittemeijer EJ. Philos. Mag. 2008;88:2411.
[71] Diaz NEV, Hosmani SS, Schacherl RE, Mittemeijer EJ. Acta Mater. 2008;56:4137.
[72] Bor TC, Kempen ATW, Tichelaar FD, Mittemeijer EJ, Van der Giessen E. Philos. Mag. A-Phys. Condens. Matter Struct. Defect Mech. Prop. 2002;82:971.
[73] Christian JW. The Theory of Transformations in Metals and Alloys, part I, second edition, Oxford: Pergamon Press 1975.
[74] Sarin VK, Mari D, Llanes L, Nebel CE. Comprehensive Hard Materials, Elsevier Books 2014;vol. 1-3.
[75] Hardie D, Jack KH. Nature 1957;180:332.
[76] Hosmani SS, Schacherl RE, Mittemeijer EJ. Acta Mater. 2005;53:2069.
[77] Hosmani SS, Schacherl RE, Mittemeijer EJ. Acta Mater. 2006;54:2783.
[78] Lankreijer RM, Somers MAJ, Mittemeijer EJ. Proc. Int. Conf. on High Nitrogen Steels, Eds. J. Foct and A. Hendry, Lille, France, May 18-20 1988, The Institute of Metals, London 1989.
[79] Menthe E, Rie KT, Schultze JW, Simson S. Surf. Coat. Tech. 1995;74–75, Part 1:412.
[80] Larisch B, Brusky U, Spies HJ. Surf. Coat. Tech. 1999;116–119:205.
[81] Tomio Y, Kitsuya S, Oh-Ishi K, Hono K, Miyamoto G, Furuhara T. Metall. Mater. Trans. A 2014;45A:239.
[82] Lin Y, Wang J, Zeng D, Huang R, Fan H. J. Mater. Eng. Perform. 2013;22:2567.
[83] Selg H, Meka SR, Kachel M, Schacherl RE, Waldenmaier T, Mittemeijer EJ. J. Mater. Sci. 2013;48:4321.
[84] Mashreghi AR, Soleimani SMY, Saberifar S. Mater. Design 2013;46:532.
[85] Park G, Bae G, Moon K, Lee C. J. Therm. Spray Techn. 2013;22:1366.
[86] Nikulin SA, Rogachev SO, Khatkevich VM, Rozhnov AB. Met. Sci. Heat Treat. 2013;55:351.
[87] Pinedo CE, Varela LB, Tschiptschin AP. Surf. Coat. Tech. 2013;232:839.

[88] Winck LB, Ferreira JLA, Araujo JA, Manfrinato MD, da Silva CRM. Surf. Coat. Tech. 2013;232:844.
[89] da Silva FJ, Marinho RR, Paes MTP, Franco SD. Wear 2013;304:183.
[90] Tang LN, Yan MF. J. Mater. Eng. Perform. 2013;22:2121.
[91] Nakonieczny A, Monka G. Mater. Sci. 2013;48:715.
[92] Kahraman F, Gencer GM, Karadeniz S. J. Fac. Eng. Archit. Gazi Univ. 2013;28:7.
[93] Zagonel LF, Bettini J, Basso RLO, Paredez P, Pinto H, Lepienski CM, Alvarez F. Surf. Coat. Technol. 2012;207:72.
[94] Soleimani SMY, Mashreghi AR, Ghasemi SS, Moshrefifar M. Mater. Des. 2012;35:87.
[95] Nouveau C, Steyer P, Rao KRM, Lagadrillere D. Surf. Coat. Technol. 2011;205:4514.
[96] Jiang Z-h, Tong X-j, Sun F, Wang G-s, Li Z. J. Aeronaut. Mater. 2011;31:40.
[97] Kong JH, Lee DJ, On HY, Park SJ, Kim SK, Kang CY, Sung JH, Lee HW. Met. Mater.-Int. 2010;16:857.
[98] Akbari A, Mohammadzadeh R, Templier C, Riviere JP. Surf. Coat. Technol. 2010;204:4114.
[99] Hartford J. Phys. Rev. B 2000;61:2221.
[100] Podgurski HH, Davis FN. Acta Metall. Mater. 1981;29:1.
[101] Rickerby DS, Henderson S, Hendry A, Jack KH. Acta Metall. Mater. 1986;34:1687.
[102] Hosmani SS, Schacherl RE, Mittemeijer EJ. Metall. Mater. Trans. A-Phys. Metall. Mater. Sci. 2007;38A:7.
[103] Yang MM, Krawitz AD. Metall. Trans. A 1984;15:1545.
[104] Kamminga JD, Janssen G. Surf. Coat. Technol. 2005;200:909.
[105] van Wiggen PC, Rozendaal HCF, Mittemeijer EJ. J. Mater. Sci. 1985;20:4561.
[106] Schacherl RE, Graat PCJ, Mittemeijer EJ. *Modelling the nitriding kinetics of iron-chromium alloys*. In: Chandra T, Torralba JM, Sakai T, editors. Thermec'2003, Pts 1-5, vol. 426-4. Zurich-Uetikon: Trans Tech Publications Ltd, 2003. p.1047.
[107] Hosmani SS, Schacherl RE, Mittemeijer EJ. Mater. Sci. Technol. 2005;21:113.
[108] Podgurski HH, Knechtel HE. T. Metall. Soc. AIME 1969;245:1595.
[109] Biglari MH, Brakman CM, Mittemeijer EJ, van der Zwaag S. Metall. Mater. Trans. A-Phys. Metall. Mater. Sci. 1995;26:765.
[110] Schwarz B, Meka SR, Bischoff E, Schacherl RE, Mittemeijer EJ. accepted for publication in Acta Mat. 2014.
[111] Mittemeijer EJ, van Mourik P, de Keijser TH. Phil. Mag. A 1981;43:1157.
[112] Delhez R, Mittemeijer EJ. J. Appl. Crystallogr. 1975;8:609.
[113] Hosmani SS, Schacherl RE, Mittemeijer EJ. J. Mater. Sci. 2008;43:2618.
[114] Benedictus R, Böttger A, Mittemeijer EJ. Phys. Rev. B 1996;54:9109.
[115] Pearson WD. *A Handbook of Lattice Spacing and Structures of Metals and Alloys*. New York: Pergamon Press, 1958.
[116] Ferguson P, Jack KH. J. Met. 1982;35:A73.

List of publications

1. B. Schwarz, R. E. Hoerth, E. Bischoff, R. E. Schacherl and E. J. Mittemeijer: The Process of Tungsten-Nitride Precipitation upon Nitriding Ferritic Fe- 0.5 at.% W Alloy. *Defect and Diffusion Forum*, 334-335, 284, 2013 (Chapter 2 of this thesis).

2. B. Schwarz, H. Goehring, S. R. Meka, R. E. Schacherl and E. J. Mittemeijer: Pore Formation upon Nitriding Iron and Iron-based Alloys; The Role of Alloying Elements and Grain Boundaries. Submitted for publication to *Metallurgical and Materials Transactions A* (Chapter 3 of this thesis).

3. B. Schwarz, S. R. Meka, R. E. Schacherl, E. Bischoff and E. J. Mittemeijer: Nitriding of Iron-based Ternary Fe-V-Si Alloy; The Precipitation Process of Separate Nitrides. To be published in *Acta Materialia* (Chapter 4 of this thesis).

4. B. Schwarz, P. J. Rossi, L. Strassberger, F. Joerg, S. R. Meka, E. Bischoff, R. E. Schacherl and E. J. Mittemeijer: Coherency Strain and Precipitation Kinetics; Crystalline and Amorphous Nitride Formation in Ternary Fe-Ti/Cr/V-Si Alloys. Submitted for publication to *Philosophical Magazine* (Chapter 5 of this thesis).

Erklärung über die Eigenständigkeit der Dissertation

Ich versichere, dass ich die vorliegende Arbeit mit dem Titel

„*Gas Nitriding of Iron-based Alloys*“

selbständig verfasst und keine anderen als die angegebenen Quellen und Hilfsmittel benutzt habe; aus fremden Quellen entnommene Passagen und Gedanken sind als solche kenntlich gemacht.

Stuttgart, den 23. Mai 2014: 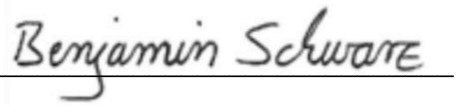

Danksagung

Diese Arbeit wurde am Max-Planck-Institut für Intelligente Systeme (ehemals Max-Planck-Institut für Metallforschung) in Stuttgart angefertigt. Hiermit möchte ich mich bei allen Personen bedanken, die zum Gelingen dieser Arbeit beigetragen haben.

An erster Stelle danke ich Herrn Prof. Dr. Ir. E. J. Mittemeijer, meinem Doktorvater, für die Aufnahme in seine Abteilung und für sein unentwegtes Vertrauen in mich. Aufgrund der unbändigen Neugier, seinem Enthusiasmus für die Wissenschaft, sowie dem unermüdlichen Einsatz den er für seine Doktoranden aufbringt, hat er diese Arbeit in größtem Maße vorangebracht. Dabei war die Zusammenarbeit immer freundlich und die unzähligen Diskussionen sehr förderlich.

Zudem danke ich Herrn Prof. Dr. J. Bill für die freundliche Übernahme des Mitberichts und Prof. Dr. T. Schleid für die Bereitschaft den Prüfungsvorsitz zu übernehmen.

Außerdem danke ich Dr. Meka und Dr. Schacherl, meinen täglichen Betreuern, für Ihre Hilfs- und ihre Diskussionsbereitschaft, sowie dem außergewöhnlich freundlichen Umgang. Auch Dr. Bischoff und Dr. Leineweber möchte ich für all ihre Unterstützung danken.

Ich danke der International Max Planck Research School for Advanced Materials, die diese Arbeit teilweise finanziert hat.

Meine Kollegen haben zum Gelingen dieser Arbeit ebenfalls in großem Maße beigetragen. Dabei danke ich namentlich Ute und Winni sowie im Gesamten der Abteilung Mittemeijer. Sie alle haben zu einer äußerst angenehmen Arbeitsatmosphäre beigetragen. Besonders danke ich auch Herrn Jürgen Köhler, der mich gerade zu Beginn dieser Arbeit durch seine große Hilfsbereitschaft in vielen Bereichen unterstützte bevor er unerwartet verstarb.

Zuletzt danke ich ganz herzlich Sarah und meiner Familie für die unermüdliche Unterstützung und ihren Rückhalt.

Curriculum Vitae

Persönliche Angaben:

Name: Benjamin Schwarz

geboren am 3. Januar 1983 in Waiblingen

Schulbildung:

1995 – 1999: Staufer-Realschule in Waiblingen, mit dem Abschluss der mittleren Reife
1999 – 2002: Technisches Gymnasium Waiblingen, mit dem Abschluss der fachgebundenen Hochschulreife

Zivildienst:

2002 – 2003: Remstalwerkstätten der Diakonie Stetten e. V. in Waiblingen

Universitäre Ausbildung:

2003 – 2010: Studium der Werkstoffwissenschaft an der Universität Stuttgart, mit dem Abschluss Diplom-Ingenieur. Diplomarbeit über das Thema „Gas Nitriding of Fe-2 at.% Al Alloy“ bei Prof. Dr. Ir. E. J. Mittemeijer an dem Max-Planck-Institut für Metallforschung
2007: Forschungspraktikum über das Thema „The Electrocatalytic Oxygen Reduction Reaction at Au/Pt-Nanoclusters“ bei Dr. Eric W. McFarland an der University of California in Santa Barbara und dem Materials Research Lab, USA

Promotion:

2010 – 2014: Promotion zum Dr. rer. nat. über das Thema „Gas Nitriding of Iron-based Alloys“ bei Prof. Dr. Ir. E. J. Mittemeijer an dem Max-Planck-Institut für Intelligente Systeme (ehemals Max-Planck-Institut für Metallforschung)